VINCENT KÜMMERER

ANOMALOUS LAYERS IN THE SOUTHERN PORTUGUESE CONTINENTAL SHELF SEDIMENTARY RECORD: POTENTIAL EVIDENCE OF THE 1755 CE LISBON TSUNAMI

UNIVERSIDADE DO ALGARVE
FACULDADE DE CIÊNCIAS E ECNOLOGIA
2019

VINCENT KÜMMERER

ANOMALOUS LAYERS IN THE SOUTHERN PORTUGUESE CONTINENTAL SHELF SEDIMENTARY RECORD: POTENTIAL EVIDENCE OF THE 1755 CE LISBON TSUNAMI

Master in Marine and Coastal Systems
Work performed under the supervision of:

Teresa Drago (IDL, IPMA)
Cristina Veiga Pires (UAlg, CIMA, Faro)

UNIVERSIDADE DO ALGARVE
FACULDADE DE CIÊNCIAS E TECNOLOGIA
2019

Declaração de autoria de trabalho / Declaration of Authorship of work

ANOMALOUS LAYERS IN THE SOUTHERN PORTUGUESE CONTINENTAL SHELF SEDIMENTARY RECORD: POTENTIAL EVIDENCE OF THE 1755 CE LISBON TSUNAMI

Declaro ser o autor deste trabalho, que é original e inédito. Autores e trabalhos consultados estão devidamente citados no texto e constam da listagem de referências incluída.

I declare to be the author of this work, which is original and unpublished. Authors and works consulted are duly cited in the text and are included in the list of references.

X

Vincent Kümmerer

Faro, 30th of September 2019

Copyright

Dedication and Acknowledgment

I am most grateful to both of my supervisors Teresa Drago and Cristina Veiga-Pires for helping me with any issue I faced working on this thesis. I felt supported by them throughout the whole time and appreciated for the work I did.

I would like to acknowledge i) all team members involved in the project ASTARTE and especially the team of WP2 (task 2.2), namely Teresa Drago, Pedro Silva, Ana Lopes, Vitor Magalhães, Cristina Roque, Ana Isabel Rodrigues, João Noiva, Pedro Terrinha, Anxo Mena, Guillermo Francés, Achim Kopf, David Völker, Emília Salgueiro, Ana Alberto and the responsible researcher of the project Maria Ana Baptista; ii) the Laboratory of Geology of IPMA Algés, under the responsibility of Fátima Abrantes for the SEM utilisation and particularly Cristina Lopes and Vitor Magalhães for the help in the SEM analysis; iii) the CIMA research center project UID/MAR/00350/2013 for receiving me in its facilities; and iv) the financial support of my parents. Furthermore, I would also like to thank Joaquim Luis for helpful information about the NSWING model and particularly making me familiar to GMT; my brother Felix Kümmerer, helping me with programming and discussing general concepts of my work; Maarten Blaauw for helping me with the age modelling with rbacon; and Óscar Ferreira for commenting the dissertation plan. I express special thanks to Kate Malmgren for correcting my English and giving constructive comments. I thank my parents Elisabeth and Albrecht Kümmerer and my brothers Felix and Robin Kümmerer for motivation, interest, and trust for my work besides the financial support. Last but not least, I thank my colleagues Valeria Fanti and Jonas Stock and the ‘Dream Team’ for fruitful comments and support.

This work is a contribution to the ASTARTE project.

Abstract

At present, knowledge about tsunami event deposits in outer shelf environments with water depths > 60 m is limited, although understanding of the involved processes as tsunami induced erosion of seafloor sediments and induced backwash currents are critical for tsunami hazard assessment. Both, incoming tsunami waves and generated backwash currents can leave signatures in the offshore sedimentary record. Preservation of tsunami imprints seems more likely in offshore deposits as in onshore deposits, which are in contrary more regarded. Thus, a multidisciplinary approach was conducted to detect probable imprints left by the 1755 Lisbon tsunami event in 3 cores from the southern Portuguese continental shelf with water depths > 57 m. Age model results, based on ^{14}C and ^{210}Pb ages, confirm the ages of the sediment to the 1755 Lisbon tsunami event. Other extreme events such as storms can be excluded trough hydrodynamic considerations. Implementing new high-resolution methodologies as the multivariate analyses of sand composition and microtextural features on quartz grain surfaces yielded more evidence for a tsunamigenic origin of previous detected high energy event layers in the studied core sections in the context of ASTARTE project, although no remarkable terrigenous signal is present. The heterogenous and mixing character of the probable 1755 Lisbon offshore tsunami deposits coupled with hydrodynamic considerations suggest, that subunits related to different tsunami wave incursions and backwash phases re unlikely to be preserved in similar environments as the study area. Also, spatial depositional differences of tsunami sediments were encountered in the study area by differences in mean grain size, sand composition, and simulated horizontal surface velocities. The new applied methodologies contribute paleo-tsunami layer identification and facilitate new studies on offshore tsunami deposits. While the southern Portuguese shelf seems to be a very good study area, we suggest for near future works to collect multiple cores aligned in transects for a better understanding of tsunami sedimentation dynamics

Key-Words: Tsunami Deposit; Offshore; Sand Components; CE 1755; Backwash; Portugal

Resumo

Atualmente, o conhecimento sobre os depósitos de eventos de tsunamis em ambientes de plataforma externa com profundidades de água > 60 m é limitado, embora a compreensão dos processos envolvidos, como a erosão induzida pelo tsunami de sedimentos do fundo do mar e correntes de retorno, seja fundamental para a avaliação do risco de tsunamis. Tanto as ondas de tsunami que chegam quanto as correntes de retorno geradas podem deixar assinaturas no registo sedimentar offshore. A preservação das marcas do tsunami parece mais provável nos depósitos offshore do que nos depósitos onshore, embora sejam estes últimos os mais estudados. Neste contexto, foi realizada uma abordagem multidisciplinar no registo sedimentar potencialmente relacionado com o tsunami de 1755 que afectou Lisboa, com base em 3 sondagens da plataforma continental do sul de Portugal, a profundidades maiores que 57 m. Os resultados do modelo de idades que conjuga dados de ^{14}C e ^{210}Pb, confirmam a relação deste registo com o tsunami de Lisboa de 1755 enquanto outros eventos extremos, como tempestades, é excluída através de considerações hidrodinâmicas. A utilização de uma abordagem multidisciplinar de alta resolução, como a análise multivariada da composição mineralógica da areia e as características microtextuais em superfícies de grão de quartzo, suportam a evidência sobre a origem tsunamigénica dos níveis previamente definidos nas sondagens estudadas no âmbito do projecto ASTARTE, embora não seja visível nenhum vestígio evidente de acarreio terrígeno. O carácter heterogéneo e misto dos depósitos de plataforma correspondentes ao tsunami de 1755 de Lisboa, associados a determinadas condições hidrodinâmicas, sugerem que as subunidades relacionadas com diferentes incursões de ondas de tsunamis e fases de retorno não conseguem serem preservadas em ambientes de plataforma, semelhantes aos da área de estudo. Além disso, diferenças espaciais de deposição de sedimentos de tsunamis foram encontradas na área de estudo através das diferenças na média granulométrica, composição da areia e através do cálculo das velocidades de corrente horizontais. A cxonjugação de vários indicadores como os utilizados neste trabalho permite ampliar ainda mais o conjunto de ferramentas para a identificação de níveis de paleo-tsunami e avançar com novos estudos sobre depósitos de tsunamis no domínio da plataforma continental. Para uma melhor compreensão da dinâmica de sedimentação de tsunamis em regiões de plataforma externa, sugere-se o estudo de várias sondagens localizadas ao longo de transectos, parecendo a plataforma sul de Portugal uma área de estudo promissora.

Resumo Alargado

Os tsunamis representam um dos riscos naturais com maior impacte para as zonas costeiras, densamente povoadas. Considerando a subida global do nível do mar, o risco potencial envolvido neste tipo de evento extremo pode mesmo vir a aumentar. Neste contexto, compreender a natureza dos processos relacionados com os tsunamis é crucial para a implementação de medidas de mitigação apropriadas, em simultâneo com um maior envolvimento da população, tanto a nível do conhecimento como da preparação para este tipo de eventos. Atualmente, o conhecimento sobre os depósitos sedimentares resultantes de eventos energéticos (tempestades, tsunamis) na plataforma continental, e em particular na plataforma externa (>60m), é ainda limitado, sendo a compreensão dos processos envolvidos, como a erosão de sedimentos de fundo por correntes de retorno ("backwash"), fundamental para a sua identificação e caracterização.

Estas correntes de retorno podem arrastar material terrestre e costeiro e transportá-lo até profundidades de plataforma continental externa. Neste ambiente marinho, é mais provável que os depósitos de tsunamis sejam melhor preservados do que nas áreas terrestres. No entanto, até muito recentemente, os estudos sedimentológicos relativos à identificação e caracterização de eventos de tsunami em registos sedimentares, centravam-se nos depósitos localizados "onshore". Mas se por um lado a preservação dos depósitos de tsunami será melhor que em ambiente terrestre, as diferentes caraterísticas geológicas regionais, como a batimetria e as fontes sedimentares disponíveis, tornam a identificação dos níveis correspondentes aos eventos de tsunami mais complexa em ambiente de plataforma. Nesse contexto, a utilização de um conjunto de indicadores diferentes e relativos a várias áreas de estudo é crucial para identificar e caraterizar os níveis de tsunamis.

No presente estudo, a importância/impacte do tsunami de Lisboa de 1755 e a informação histórica e científica existente foram consideradas bons requisitos para se avançar um pouco mais no estudo de depósitos de tsunami localizados "offshore". Assim, tendo por objetivo a confirmação dos níveis identificados com origem em tsunami, utilizaram-se, como base de estudo, três sondagens (M106, M107 e POP2) colhidas na plataforma continental externa a oeste de Faro (entre profundidades compreendidas entre 57 e 91 m). Foram utilizados vários indicadores sedimentológicos e as análises que foram realizadas com intervalo centimétrico

incluíram, além da granulometria, o estudo composicional da fração arenosa e as características microtexturais das superfícies dos grãos de quartzo. Pretendeu-se assim, encontrar possíveis diferenças entre os 'níveis de tsunami' e a sedimentação normal de plataforma continental, resultantes tanto dos diferentes processos de sedimentação como da origem do material envolvido.

Para isso, foram elaborados modelos de idades para cada sondagem, com base nas taxas de sedimentação inferidas a partir dos resultados de ^{14}C e de ^{210}Pb e usando estatísticas baiesianas. Estes modelos permitiram a correlação dos níveis anteriormente identificados como de "alta energia", com o evento do tsunami de 1755 CE. Além disso, considerações teóricas relacionadas com a profundidade limite da agitação marítima discutidas no presente trabalho excluem outros possíveis eventos extremos como tempestades e inundações na deposição dos níveis em questão. Por conseguinte, é muito provável que estes correspondam aos níveis de tsunami decorrente do sismo de 1755 que afetou grandemente as zonas do Algarve e de Lisboa. Apesar desta correlação, não se encontraram evidências significativas e claras de material transportado pelas ondas de retorno, com o carácter terrígeno que à partida se poderia esperar, como, por exemplo, maior abundância de madeira ou fragmentos de material rochoso derivado do continente. No entanto, a análise multivariada da análise composicional da areia revelou pequenas, mas distinguíveis diferenças entre os sedimentos relacionados com o tsunami e a sedimentação de fundo da plataforma continental. Por outro lado, verificou-se um aumento significativo de "superfícies frescas" e um aumento ligeiro de "marcas de percussão" nos grãos de quartzo dos níveis correspondentes ao tsunami. Estas caraterísticas apoiam a hipótese de uma sedimentação de diferentes caraterísticas nos níveis relacionados com o tsunami e os correspondentes ao regime de sedimentação normal de plataforma.

Nos níveis identificados como relacionados com o tsunami, a composição da areia apresenta um aumento de fragmentos de conchas em comparação com a sedimentação de fundo. Além disso, essas camadas tsunamigénicas exibem uma tendência decrescente na média granulométrica da amostra total (sequências granulo-decrescente), apesar da média da fracção arenosa não mostrar nenhuma variação. Exceção feita, no entanto, para uma das sondagens (M107) na qual essa tendência é visível quer na amostra total quer unicamente na fração arenosa. A componente arenosa desta sondagem apresenta uma maior percentagem

de grãos terrígenos do que as duas outras sondagens o que explica provavelmente que na camada tsunamigénica a mesma apresente um aumento de percentagem da mica na parte superior dos níveis de tsunami e não um aumento de percentagem nos fragmentos da conchas como observado nas duas sondagens da plataforma externa.

A simulação hidrodinâmica da corrente de retorno do tsunami efetuada no presente trabalho implica a existência de uma contribuição dos sedimentos da zona costeira entre Faro e Quarteira pertencente ao Sistema de Barreiras da Ria Formosa. Isto pode explicar o fraco sinal da componente terrígena nos níveis de tsunami, uma vez que o transporte de sedimentos exclusivamente de origem continental é inibido devido ao carácter protetor do sistema de ilhas barreiras da Ria Formosa que não permitiu o avanço da onda de tsunami para o interior. As diferenças das secções estudadas entre sondagens podem ser explicadas pelas diferenças espaciais de deposição sedimentar do tsunami e pelas diferentes velocidades nos respetivos locais a diferentes profundidades. O carácter heterogéneo geral detetado dos prováveis depósitos do tsunami de 1755, juntamente com os resultados do modelo hidrodinâmico, sugerem que as subunidades definidas e relacionadas com diferentes incursões de ondas de tsunamis e fases de retorno não são suscetíveis de serem preservadas em ambientes semelhantes aos da plataforma externa do sul de Portugal.

O estudo multidisciplinar utilizado neste trabalho alarga a possibilidade de identificação/caraterização de depósitos de tsunamis em ambiente de plataforma, permitindo assim estimar os intervalos de recorrência dos mesmos em estudos que tenham por base registos sedimentares em ambientes de plataforma semelhantes à estudada. Também se contribuiu para um melhor entendimento/conhecimento da dinâmica de sedimentação de um evento de tsunami numa plataforma continental, sendo, no entanto, necessário mais e melhores estudos nesta área, tendo por base o estudo de várias sondagens localizadas em transetos perpendiculares à costa e em áreas com inundações máximas como, por exemplo, a conhecida área de estudo do tsunami Boca do Rio, no sul do Algarve. Em geral, a plataforma do sul de Portugal parece ser uma área muito boa para estudos sobre processos de sedimentos tsunamigénicos.

Content

List of Figures

List of Tables

1. Introduction

Coastal areas are densely populated and are simultaneously particularly at risk of natural hazards. Tsunamis are one of the most dangerous hazards often resulting in high numbers of casualties and severe damage in coastal areas like the Tohoku-Oki event in March 2011 and the most recent tsunami in Indonesia at the 25th of December 2018. More than one million recorded deaths have been connected to tsunami impacts worldwide since historical times (Röbke and Vött, 2017) and estimates of the financial damage caused by the Tohoku-Oki tsunami in 2011 alone are up to $335 billion (Daniell and Vervaeck, 2012). In 2030, it is projected that nearly one billion people will live in areas vulnerable to tsunami events along the coast (Neumann et al., 2015). Within the context of global sea level rise, threats of coastal inundation by marine and coastal hazards has risen (Reed et al., 2015). Therefore, understanding the nature of tsunami related processes is crucial to develop appropriate mitigation measures and enhance knowledge and preparedness of civilization.

Portugal lies in close proximity to the western segment of the Eurasia-Nubia plate boundary, a highly tectonically active area capable of generating severe earthquakes (Zitellini et al., 2009; Shanmugam, 2012; Matias et al., 2013). Andrade et al. (2016) revised the amounts of tsunamis that occurred in Portugal to 7 events since historical times and showed that only the notorious 1755 Lisbon tsunami left geological evidence along Algarve lowlands. Studies of high energy deposits in sedimentary records of paleaotsunamis are used to expand the data to pre-historic times. The sedimentary records can originate from both deposits on land and marine deposits, while the latter is less explored (e.g. Dawson and Stewart, 2007) but is potentially more revealing (Reinhardt et al., 2006; Rhodes et al., 2006; Weiss and Bahlburg, 2006; Sakuna et al., 2012). Marine sediments deposited by the tsunami are a result of either reworked sediments due to the initial tsunami wave or by traction generated backwash currents of the tsunami wave. Studies of tsunami sediments also enhance the knowledge about sedimentation dynamics of tsunami events. Enhanced knowledge about dynamics of sedimentation can aid in tracing back currents and their associated forces during the event. Besides the potential to save lifes and capital in coastal areas exposed to tsunami risk, geological knowledge of tsunami events need be widened in order to better understand these dangerous hazards.

The EU-project ASTARTE (Assessment, STrategy And Risk Reduction for Tsunamis in Europe) (www.astarte-project.eu) executed between 2013 and 2017, had the ultimate goal to reach a higher level of tsunami resilience in the NEAM (North East Atlantic & Mediterranean)

region, in order to improve preparedness of coastal populations, and, ultimately, to save lives and assets. One of the tasks was dedicated to the evaluation of tsunami recurrence intervals in the North East Atlantic region based on the study of the shelf sedimentary record.

Tsunami recurrence intervals resulting from earthquake studies need to be verified by evidence resulting from tsunami deposits, otherwise they are most likely biased, because there are many other tsunami triggering-processes such as landslides, volcanic eruptions, or a combination of multiple events. In Augusta Bay (Italy), Smedile et al. (2011) identified 12 layers that are most likely related to tsunami events. Those results suggest an approximate recurrence time of every 330-370 years. Tsunami recurrence intervals from sedimentary records can only be identified when there is clear evidence for the tsunamigenic origin of layers in the sedimentary record. For certainty of a tsunamigenic origin in the offshore sediment record, it is helpful to have historical data of tsunamis from eyewitnesses and geological studies on onshore tsunami deposits. With this previous knowledge, it is possible to validate the geological proxies that identify the tsunamigenic layers of the recent and historical tsunamis in the sediment cores. Therefore, studying offshore records of tsunamis in the area of Portugal is promising, since there are both several studies on onshore tsunami deposits (e.g. Dawson et al., 1995; Hindson and Andrade, 1999; Cuven et al., 2013; Font et al., 2013; Vigliotti et al., 2019) (chapter 1.2) and an extensive tsunami catalogue (Baptista and Miranda, 2009; Andrade et al., 2016). Besides, Abrantes et al. (2008) and Quintela et al. (2016) already found tsunami deposits in Portuguese shelf sediments that are related to the 1969 and 1755 Lisbon tsunami events, although clear sedimentological characteristics evidence of the tsunamigenic layers in the southern Portuguese shelf needs to be further expanded.

1.1. Physical and Sedimentary Aspects of Tsunamis

Large tsunamis are mostly triggered by big offshore earthquakes. Although generated offshore, tsunamis behave like shallow water waves with enormous wavelengths in the order of hundreds of kilometers. In the open ocean, properties of tsunami waves are comparatively small with wave heights in the range of 1 meter. However, their vertical extension comprises the entire water column even in the deep sea and wave periods range from a few minutes to 2 hours. Waves lose energy when propagating through water, but the loss of energy is inversely proportional to the wavelength and phase velocity. Consequently, tsunami waves are powerful and able to cross whole oceans keeping almost their entire initial energy. The phase velocity of the tsunami wave is positively correlated with the Earth's gravity and the depth of the ocean.

Therefore, tsunami waves decelerate when reaching shallower depths at seamounts or continental shelves (Helal and Mehanna, 2008; Röbke and Vött, 2017). In contrast to the deep sea, due to shoaling, the wave height is rising in the nearshore zone in the order of 3 to 6 fold of the original wave height (Ward, 2001). Results of the shoaling are run-ups heights of tens of meters and horizontal inundation expanses of several km inland (Hindson et al., 1996).

A tsunami event can be divided into 4 physical stages that are relevant for distinguishing different sedimentation regimes (Dawson and Stewart, 2007). These physical stages are (1) generation, (2) propagation, (3) inundation, and (4) traction. Anything capable of disturbing the water column can be a triggering mechanism of a tsunami wave, corresponding to the generation phase. There are a variety of source types which include seismic, volcanic, landslides or even asteroid impacts (Papadopoulos, 2015). Propagation of the tsunami waves to shallower water causes erosion of seafloor sediments that are thus put into suspension due to high frictional velocities (Sugawara and Goto, 2012). When the wave is large enough (higher than ~7 m) it can even affect deep-sea sediments (Kastens and Cita, 1981). The inundation phase of the wave onto onshore areas, although significantly slowed down, erodes more material and transport it further landward. After a point of zero velocity, gravity generates traction, in the form of tsunami backwash currents from the maximum inundation area to deeper waters (Einsele et al., 1996). The consequences of backwash processes are in general less studied compared to run-up processes. Thus, backwash currents can be even more powerful and erosive than run-up flows. Reasoning are that backwash currents are concentrated in for example coastal depressions and loaded with a high quantity of continental detrital material (Le Roux and Vargas, 2005; Feldens et al., 2008). Thus, these currents can generate hyperpycnal backwash flows, causing offshore accumulation of allochthonous material (Paris et al., 2010). Large plumes moving offshore and transporting material were also observed from satellite images and video footage after the 26th December 2004 Indian's ocean tsunami (e.g. Umitsu et al., 2007).

Offshore tsunamigenic sedimentation processes (**Figure 1**) are still under debate. Sugawara et al. (2009) states that currents generated by backwash are the major sedimentation-processes responsible for offshore deposition of tsunami sediments, while resuspension by the initial tsunami propagation is a minor sedimentation process (Sugawara et al., 2009). On the other hand, there is also evidence that the landward propagating wave can cause deposition of sediments (Jonathan et al., 2012; Sakuna et al., 2012; Ikehara et al., 2014). For instance, Ikehara

et al. (2014) used the accident at the Fukushima-Daiichi Nuclear Power Plant caused by the 2011 Tohoku-Oki tsunami for studying the response of sea floor sediments to tsunamis.

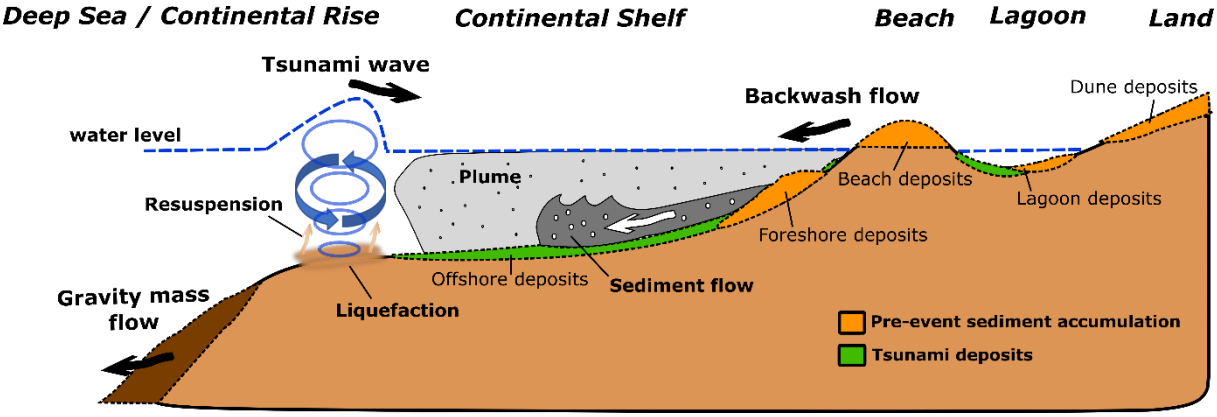

Figure 1: Conceptual model of tsunami sedimentation processes, deposits and propagation from deep sea to inland (modified after Einsele et al. 1996 and Sugawara et al. 2009).

This accident released short-lived radioactive elements providing a tracer for material transport and chronological evidence. Thus, they were able to detect two sedimentation phases generating two turbidite sequences, one before and one after the accident, suggesting that the initial propagation of the tsunami wave can resuspend seafloor sediments and deposits tsunamigenic sediments. Consequently, both sedimentation processes induced by backwash currents and resuspension were detected. Backwash current can be traced by allochthonous material (Sakuna-Schwartz et al., 2015) while resuspension sedimentation lacks this property.

1.2. The 1755 Lisbon Tsunami

The 1755 (CE) Lisbon's tsunami was caused by one or several (e.g. Matias et al., 2013) offshore earthquakes with a magnitude of 8.75 M_W (moment magnitude) (e.g. Johnston, 1996). The location of the faults that produced the earthquake is still under debate but several authors suggested the Horseshoe Abyssal Thrust Fault and the Marquês de Pombal Fault (e.g. Omira et al., 2009; Ramalho et al., 2018; Costa et al., 2019). A study on historical reports from affected countries of the 1755 tsunami inferred wave periods around 20 min, run-up heights between 1 and 15 m, wave heights higher than 15 m and 3 to 6 numbers of tsunami waves depending on the locality (Baptista et al., 1998). In lowlands of the Algarve coastline, there are several geological records of the 1755 Lisbon tsunami (**Figure 2**), whereas other historical tsunamis since Roman times do not seem to have any signature in onshore sediments (Andrade et al., 2016). A well-studied site is the coastal lowland Boca do Rio located in the coastline of the Algarve.

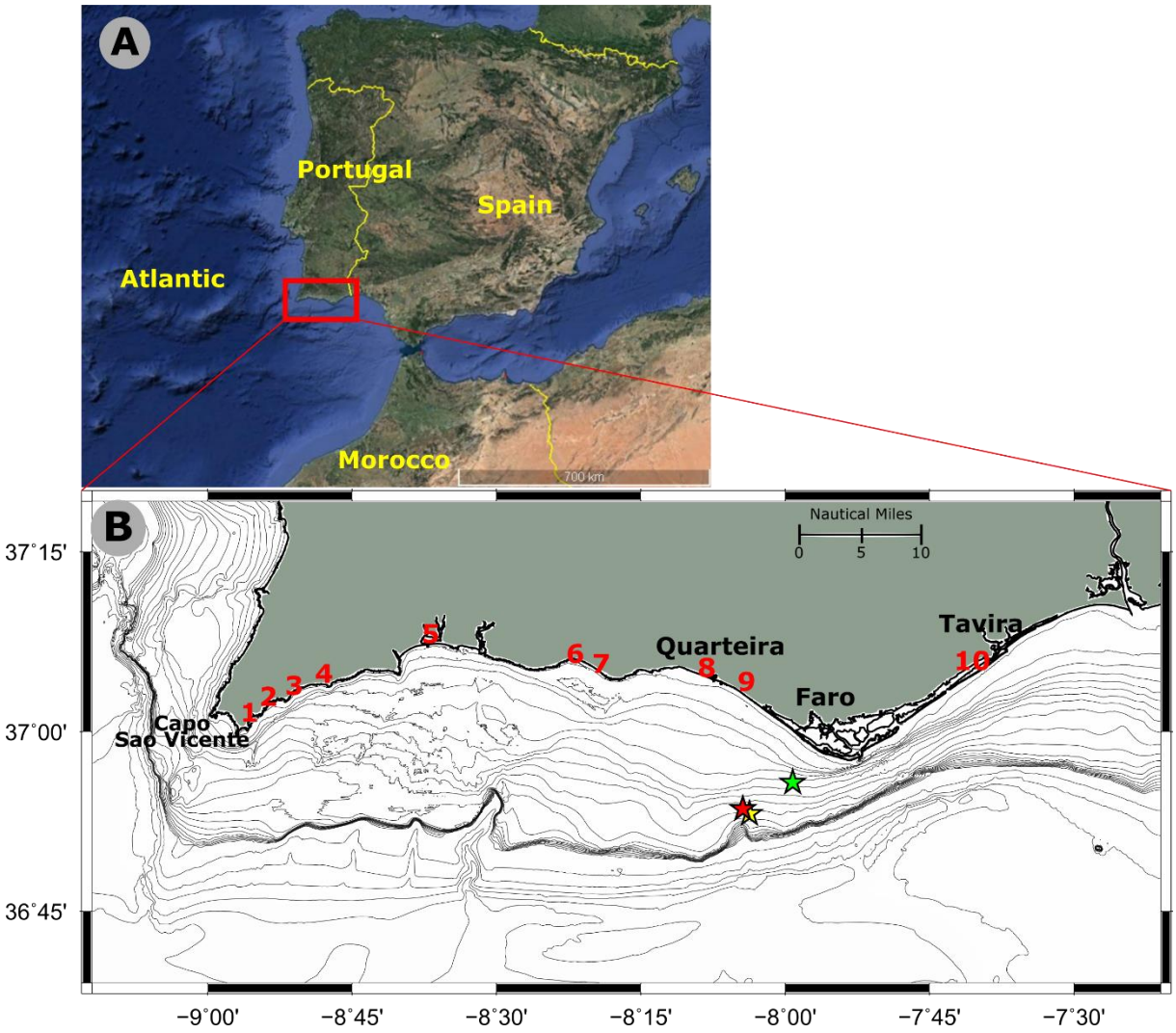

Figure 2: (A) Google earth image of the study site (marked with the red box) located in the Algarve, south Portugal. (B) Detailed view of the study area with core locations (red = M106, green = M107, yellow = POP2), contour lines are in 10 m steps till 200 m water depth than change to 100 m steps. Sites of onshore 1755 event geological studies, 1-Martinhal, 2-Barranco, 3- Furnas, 4-Boca do Rio, 5-Alvor, 6-Alcantarihla, 7-Salgados, 8-Quarteira, 9-Carcavai, 10-Ria Formosa barrier-lagoon. (bathymetry source: w3.ualg.pt/%7Ejluis/mirone/misc/algarve50.grd (20/05/2019).

In this place, the source of the sand and the change in the hydrodynamic process forming the event deposits are controversial (e.g. Hindson and Andrade, 1999; Font et al., 2010; Vigliotti et al., 2019). The interpretations of the hydrodynamic processes, including the initial tsunami wave, wave reflection or backwash, involves multiple inundation phases by several waves (Hindson et al., 1996), one wave that generated several inundation and backwash phases (Font et al., 2010) and two inundation phases and one backwash phase (Vigliotti et al., 2019). Other authors reached a similar interpretation in a study of Salgados lagoon (Moreira et al., 2017). In Los Lances Bay, southwestern coast of Spain, 8 subunits of this event were found in one core interpreted with at least 4 incoming wave phases, three settling phases and one backwash phase (Cuven et al., 2013). This shows that the signature of the hydrodynamic processes in onshore

records is not straight forward and depend greatly on locality including distance to the shoreline. Hence, historical and geological data from onshore deposits do not coincide and the amount of inundation, settling and backwash phases for the 1755 Lisbon tsunami are not clarified.

1.3. Offshore Tsunami Deposits

Dawson and Steward (2007) reviewed tsunami deposits in the geological record. They concluded, that on one hand, the study of stratigraphic units of onshore tsunami deposits associated to onshore sedimentation has not been identified for prehistoric/ancient tsunamis, while on the other hand most published studies of recent or historical tsunami deposits are concentrated on onshore deposits and only little attention is given to the offshore realm. At present, the importance of studies in the offshore realm recognized more attention but only 15 works were published dealing with possible tsunami sediments from the continental shelf of depths deeper as 50 m (**Table 1**).

Table 1: List of studies dealing with possible tsunami sediments in the continental shelf realm. Multiple tsunamis mean that at least 2 or more tsunamis layers were studied, IOT = Indian Ocean Tsunami, TOT = Tohoku-Oki Tsunami. Tsunami vs. Storm: '-' means the topic was not discussed in the work, '×' means the topic was discussed but a clear distinction between the high energy events is not clear, '✓' means that the topic is discussed and they are certain of tsunamigenic origin. Depth refers to the water depth where surface samples/cores or geophysical data were collected. Here the definition for the inner shelf, shelf, shelf /rise, and deep sea are till >50 m, >=50 m, >200 m and >1000 m respectively. Bays are more protected shallow marine environments and therefore considered differentially. AAS = Atomic Adsorption Spectrometer, FTIR = Fourier Transform Infrared Spectrometry, MS = Magnetic Susceptibility, MSCL = Multi-Sensor Core Logger, OM = Organic Matter, PAH = Polycyclic Aromatic Hydrocarbons, TOC = Total Organic Carbon, XRF = X-ray Fluorescence, XRD = X-ray Diffraction.

Location	Source	Tsunami Event [CE]	Storm vs. Tsunami	Depth	Environment	Methods
Japan						
SE Hokkaido	Noda et al. (2007)	2003 TOT	×	38-112	Shelf	Grain-size; Sedimentary Structure; Microfossil (Diatom, Foraminifera); Geophysical; XRD; Modelling.
Sendai Bay	Ikehara et al. (2014)	2011 TOT	✓	122	Shelf	XRD; TOC; C/N; Mud content; Sediment composition; ^{134,137}Cs; ^{210}Pb; δ^{13}C.
Sendai Bay	Tamura et al.(2015)	2011 TOT	×	14-30	Inner Shelf	XRD; Grain-size; ^{134,137}Cs.
Off Shimokita	Toyofuku et al.(2014)	2011 TOT	-	55-211	Shelf	Grain-size; ^{210}Pb; Foraminifera; OM (C/N, biomarkers, Chl *a*, δ^{13}C); Core description.

Off Tohoku	Nomaki et al.(2016)	2011 TOT	-	310-880	Shelf Rise	TOC; TN; C/N; Nutrients; $\delta^{13}C$; $\delta^{15}N$.
Kujukuri	Pilarczyk et al.(2019)	Multiple	-	120	Shelf + Onshore	Grain-size; Foraminifera (taxonomy and taphonomy)
Thailand						
Khao Lak	Feldens et al.(2008)	2004 IOT	✓	10-70	Shelf	Geophysical; Grain Size.
Khao Lak	Sakuna-Schwartz et al. (2015)	2004 IOT	✓	9-16	Inner Shelf	Geophysical; Grain Size; Radiographs; XRF; MSCL; ^{137}Cs; ^{210}Pb.
Khao Lak	Milker et al. (2013)	2004 IOT	×	10-64	Shelf	Core description; Foraminifera.
Khao Lak	Sakuna et al. (2012)	2004 IOT	✓	9-57	Shelf	Geophysical; MSCL; XRF; MS; Grain-size; XRD; ^{210}Pb.
Khao Lak	Feldens et al.(2012)	2004 IOT	✓	5-35	Inner Shelf	Geophysical; XRD; Grain-size.
Khao Lak	Pongpiachan et al. (2013)	2004 IOT	✓	?	Shelf + Onshore	FTIR; Statistical analysis.
Khao Lak	Pongpiachan (2014)	2004 IOT	-	5-70	Shelf	PAHs.
Krabi	Sugawara et al. (2009)	2004 IOT	✓	4-30	Inner Shelf	Foraminifera; visually; Grain-size, contents; color.
Israel						
Caesarea	Reinhardt et al.(2006)	115	-	10	Inner Shelf	Archaeological excavation; molluscan fossil; ^{14}C.
Caesarea	Goodman-Tchernov et al. (2009)	-1550	✓	15 - 20	Inner Shelf	Micropalaeontology; Grain-size.
Caesarea	Goodman-Tchernov and Austin (2015)	Multiple	×	3-15	Inner Shelf	Seismic survey.
Aquaba-Eilat	Goodman Tchernov et al. (2016)	-350	✓	12.2-16.4	Inner Shelf	Grain-size; Foraminifera; Core description; photography; ^{14}C.
Off Jisr al-Zarka	Tyuleneva et al.(2018)	Multiple	✓	15.3	Inner Shelf	FTIR; XRD; XRF; Grain-size; mineralogical; ^{14}C.
Portugal						
Off Lisbon	Abrantes et al.(2005; 2008)	1969 , 1755	-	88-105	Shelf	XRF; MS; Grain-size; ^{210}Pb; ^{14}C.
Off Algarve	Quintela et al.(2016)	1755	✓	96	Shelf + Onshore	Foraminifera; Grain-size; $CaCO_3$-Content; $^{127,137}Cs$; ^{210}Pb.
Italy						
Augusta Bay	Smedile et al. (2011)	Multiple	✓	72	Shelf	Geophysical; XRD; tephrochronology; Grain-size; MS; Density; Foraminifera.
	Smedile et al. (2019)	Multiple	✓	60-108	Shelf	XRF; ^{210}Pb; ^{14}C; MSCL; Grain-size; textural components; Foraminifera.
Indonesia						

Teluk Banten	Van Den Bergh et al. (2003)	1883	✓	2-30	Bay	XRF, MS; X-ray, Grain-size; ^{210}Pb; ^{14}C.
Lhok Nga	Paris et al. (2010)	2004 IOT	×	< 25	Inner Shelf + Onshore	Offshore boulder distribution; Modelling.
India						
Chennai	Jonathan et al. (2012)	2004 IOT	-	14	Inner Shelf	Grain-size; $CaCO_3$ and OM content; Foraminifera.
Nagapattina	Veerasingam et al.(2014)	2004 IOT	✓	5-10	Inner Shelf	Grain-size; FTIR; MS.
	Srinivasalu et al.(2010)	2004 IOT	-	25	Inner Shelf	Grain-size; Organic $CaCO_3$-content; AAS
China						
East China Sea	Yang et al.(2017)	Multiple	×	5-1450	Shelf + Deep Sea	Modelling; Grain-size; ^{14}C.
American Samoa						
Pago Pago Bay	Riou et al.(2018)	Multiple	×	15-60	Bay	Seismic survey; ^{14}C; ^{210}Pb; Core description; XRF.

Offshore tsunami deposits seem to be more undisturbed and continuous than onshore tsunami deposits (Weiss and Bahlburg, 2006; Sakuna et al., 2012), but they can be altered by several post-sedimentary processes such as wave action, currents, bioturbation and geochemical alterations (e.g. Chagué-Goff, 2010; Feldens et al., 2012). Also, the local setting in terms of geology, coastal and offshore bathymetry, vegetation close to the coast and sedimentation regime makes it unlikely, that one indicator can reveal a tsunamigenic origin in onshore deposits (Goff et al., 2012; Shanmugam, 2012). Anyway, there is still discrepancy about the spatial distribution of backwash sedimentation on the continental shelf. Coleman (1968) states that a major part of tsunami deposition takes place near the shore or in the deeper offshore waters beyond the shelf and suggestes that a bathymetric survey coupled with shallow marine drilling monitoring of an area frequently experiencing tsunami waves should be conducted. Following this suggestion, Feldens et al. (2012) monitored the inner shelf off Khao Lak in Thailand, using this approach. They were able to trace the 2004 Indian tsunami event layer until a water depth of 18 m while the impact of this event was not detected by seafloor morphology or sediment distribution in the major part of the study area. Furthermore, van den Bergh et al. (2003) showed that land-derived components are only incorporated in sediments close to the shore. Later, Tamura et al. (2015) showed similar results and concluded that even a big tsunami event as the 2011 Tohoku-Oki tsunami is unlikely to leave extraordinary tsunami offshore deposits in open-

sea settings (~15 km off the shore, 30 m water depth). This highlights that studies of tsunami event layers in the continental shelf need more sophisticated and side specific multidisciplinary approaches because differences to "non-event" sediments can be small in variation and size. Tsunami deposits have characteristic properties of "event" deposits showing redeposition, erosion, episodic occurrence and are therefore different to the normal prevailing autochthonous background deposition. Hence, it is important to analyze these background sedimentary conditions to differentiate them from tsunami sedimentation of allochthonous material or rather reworked material.

A major problem in the study of tsunami deposits is the differentiation between storm and tsunami events. Both processes lead to identical depositional processes and related sedimentary features (Shanmugam, 2012). At present, this contention is not fully solved and, in some cases, is not even discussed (**Table 1**). Authors that exclude storms as a possible event for sedimentation of their interpreted tsunami layers justify this either with meteorological data, when the event was recent, (e.g. Feldens et al., 2008; Ikehara et al., 2014; Veerasingam et al., 2014) or that the storm wave base does not reach their core locations (Smedile et al., 2011; Quintela et al., 2016). Indeed, the wavelengths of storm waves are much shorter than of most tsunami waves and the wave base depends on the wavelength. Various sedimentological characteristics have been studied in order to distinguish between storm and tsunami events. One example is the stacking of subunits in tsunami deposit which can only be produced by waves with extremely long wavelengths and storm waves lack this property (Fujiwara and Kamataki, 2007). However, Shanmugam (2012) concluded that there are no reliable sedimentological criteria for distinguishing paleaotsunami deposits from paleo-storm deposits in various environments. Furthermore, based on linear wave theory, Weiss and Bahlburg (2006) compared the influence of tsunami and storm waves on shelf sediments and a water depth where tsunami deposits are protected from the storm waves. In the case of Brisbane (Australia), they concluded that the water depth in which tsunami deposits will be preserved is greater than 65 m based on a boundary storm wave with a wave height of 14.3 m and periods between 6s and 14s. In respect to this, the possibility that storms can interfere with possible tsunami layer in the shallower marine environment is high and for studies with shallower water depths this must be considered. In general, there is still a lack of evidence in offshore paleaotsunamis and other mechanisms as storm events or turbidity currents directly triggered by earthquakes (Chagué-Goff et al., 2017).

Morton et al. (2007) show differences of sandy onshore deposits between storms and tsunamis. They concluded that the difference in flow depths are > 10 m and < 3 m for tsunami

and storms, respectively, and their difference in wave dynamics result in distinguishable deposits. Tsunami deposits are distributed broad over a large region while storm deposits are concentrated within a zone relatively close to the beach. In some extreme cases, important floods can also induce similar sediment processes and thus have similar sediment deposition (Sakuna-Schwartz et al., 2015).

1.4. 'Tsunami-proxies' in Offshore Environments

The "proxies" for identifying palaeo-tsunami deposits still focus on onshore records but several can be transformed to offshore records (Chagué-Goff et al., 2011; Goff et al., 2012). Works comparing onshore and offshore tsunami deposits were also conducted (Smedile et al., 2012; Tipmanee et al., 2012; Quintela et al., 2016). For studies of potential offshore tsunami deposits, different methodologies and mostly a whole set of proxies are used to identify the tsunamigenic origin of the sedimentary layers. They include sedimentological, geochemical, geophysical, micropaleontological, archaeological, statistical and modeling disciplines (**Table 1**). In the following section, several proxies of offshore tsunami studies are introduced and discussed. The focus lies on studies with samples from water depths greater than 50 m of the continental shelf (see **Table 1**, environment: shelf) and methodologies that will be used in this study will be introduced.

1.4.1. Grain-size Distribution

Grain-size distribution in tsunami layers depends greatly on the locality of the samples and the grain size of the source material besides the current velocity. In general, tsunami deposits are marked with an increase in grain-size compared to background deposition because of the increased current velocity related to the high energy event. Tsunami layer in zones of water depths > 50 m are generally fining up in grain-size distributions. This is explained by the erosion of finer particles by the tsunami wave and dispersion of finer grains to offshore regions by backwash flows (Noda et al., 2007). Most of the tsunami layers are poorly-sorted (Goodman-Tchernov et al., 2009; Paris et al., 2010; Smedile et al., 2011; Sakuna et al., 2012) but can also be well to poorly-sorted (Abrantes et al., 2008) or well-sorted (Ikehara et al., 2014). This points out, that grain size distribution data can only serve as a supportive indicator of tsunamigenic origin, but it is difficult to consider as a reliable criterion.

1.4.2. Magnetic Susceptibility

High values of magnetic susceptibility (MS) in the core profile correspond to layers rich in ferro- or ferrimagnetic minerals. One application of MS in tsunami research is the time and cost-effective identification of ash layers to improve the age modelling, when the eruption age of the volcano is known (e.g. van den Bergh et al., 2003; Smedile et al., 2011). Another application is the identification of physical changes in the depositional environment since the magnetic signature of minor or trace magnetic components varies according to their source and depositional history (Maher et al., 2009). For instance, Abrantes et al. (2008) identified a deposit of reworked material, most likely caused by the 1755 Lisbon tsunami, due to an anomalous high peak in MS and larger medium grain sediment. In "event" layers of more shallow marine environments peaks of MS correspond to layers with higher abundance of land-derived components such as volcanic rock fragments (van den Bergh et al., 2003).

1.4.3. Inorganic Geochemistry

X-ray fluorescence (XRF) scanner are used to semi-quantitatively assess sediment composition by detection of minor and major element counts and thus allowing to detect a change in the source of the deposited sediments and differentiate terrigenous material from marine sediments. In the study of shelf "tsunami event" sediments other XRF-results often show similar results than other proxies as shown by Abrantes et al. (2008), where XRF-Fe mimics the magnetic susceptibility and XRF-Ca the mean grain size along the core profile. In offshore tsunami studies with samples originating from shallower areas this method is more promising (Sakuna-Schwartz et al., 2015; Tyuleneva et al., 2018) although XRF (K/Ti and Ca/Ti) was successfully applied in turbidite studies related to tsunami events in the deep sea off south Portugal (Gràcia et al., 2010).

1.4.4. X-Radiographs

X-radiographs are used to detect internal sedimentary structures or unconformities that cannot be seen by the naked eye. Sediments with high density (e.g. pebbles, shell fragments) are displayed in lighter grey and vice versa for sediments with lower density (Hamblin, 1962). Aside from supporting other proxies X-radiographs reveal along core changes in sedimentary processes (Noda et al., 2007; Ikehara et al., 2014). This proxy might be a good indicator to gain

more information about initial erosion and resuspension of seafloor sediments produced by the friction of the propagating tsunami wave even in greater water depths.

1.4.5. Microfossils - Foraminifera

There are several studies using microfossils and most of the works of offshore tsunami event deposits concentrated on the study of foraminifera (**Table 1**). Indicators for tsunamigenic layers are for example the increase in coastal foraminifera abundance coupled with coarser layers (Quintela et al., 2016), high concentration of displaced epiphytic foraminifera couple with grain-size changes (Smedile et al., 2011) caused by tsunami backwash. Increased ratio between agglutinated and hyaline foraminifera to total benthic foraminifera was attributed to sediment movement by tsunami wave action (Noda et al., 2007). Milker et al. (2013) developed a transfer function for water-depth reconstructions based on benthic foraminifera to reconstruct re-deposition and dynamics of sediment distribution associated with the 2004 Indian Ocean Tsunami. Thus, they were able to limit the maximum water depth of resuspension to 20 m offshore Khao Lak, Thailand. Because in their study site, storm events reveal similar characteristics and redeposition processes, they were not able to distinguish between storm and tsunami layers.

1.4.6. Sand Composition

The composition of marine sediments can vary from biogenic or terrigenous to authigenic components. These components can either be autochthonous or allochthonous. In the case of possible tsunami sediments, terrigenous particles as fragments of continental rocks (quartz, feldspar, mica, amphiboles, etc.) or other lithic fragments are an indicator for backwash processes and can provide evidence for a tsunamigenic origin of these sediments (Ikehara et al., 2014). Also, differences in mica and heavy minerals (here tourmaline) were attributed to different modes of sediment transport and deposition processes of tsunamis, because mica, a phyllosilicate, is more abundant in the top part of the tsunami event layer due to its lower density and planar shape, and heavy minerals in the lower part (Jagodziński et al., 2012). Some biogenic components (e.g. terrestrial plant fragments) can be considered as signatures of continental components (Scheffers et al., 2009) and indicator for backwash processes related to tsunami events (Feldens et al., 2008). Shell fragments can indicate allochthonous fragments from the inner shelf reworked and transported by tsunami-related processes that created a disturbed sediment bed (e.g. Abrantes et al., 2008; Toyofuku et al., 2014).

1.4.7. Microtextural Characteristics of Quartz Grains

Microtextural characteristics on quartz grains can be used for both provenance studies and studies of distinct sedimentation processes as high energy events within the same environment. Sediment transport caused by high-energy events like tsunamis or storms leave mechanical imprints on the surface of the grains. By studying the relative abundance of different imprints, it is therefore possible to detect and study the dynamics of high-energy events. Thus, tsunami grains reflect both the crossed effect of the sediment origin (multiple in the present study: dune, beach and nearshore (see **Figure 1**)) and the marked imprints during the event.

Based on a pre-existing catalogue (Mahaney, 2002), Costa et al. (2012a) summarized microtextures on quartz grain surfaces in 5 families: Angularity, fresh surfaces, percussion marks, adhering particles and dissolution. Mechanical features (fresh surfaces, percussion marks and angularity) are caused by grain collision and develop in environments of high energy (e.g. tsunamis). However, angularity is considered more as a long-term characteristic and therefore playing a more important role for provenance studies than deposition processes. Percussion marks, v-shaped patterns, are found mainly in subaqueous, high sediment concentration regimes when grain collision plays the most important role, but impact velocities are lower. Fresh surfaces are also formed in subaqueous environments but in lower sediment concentration regime. When sediment concentration is lower impacts on grain surfaces are stronger allowing to create whole new surfaces due to higher velocities. Chemical features (adhering particles and dissolution) are more representative of lower-energy environments. Adhering particles, microparticles on the grain surface, are common in alluvial and deeper environments. Dissolution, degree of dissolution on the grain surface, tends to be more common in alluvial and deeper environments. Post-sedimentary dissolution is capable of masking former mechanical marks on the grain surface.

1.5. Outer Shelf off Faro and High Energy Event Layers

The southern Portuguese continental shelf has a narrow width of 5 – 20 km compared to other shelves worldwide, due to the erosive action of the Mediterranean Outflow Water (MOW) which contributes to the narrowing of the continental slope off Faro. The outer shelf passes over to the continental slope at depths of 100 and 140 m and has an average slope gradient of 0.4 ° - 0.53 ° and 0.3 ° to 0.4 ° in the outer continental shelf (Roque et al., 2010). The shelf break direction is generally southwards, except along the continental shelf area between Faro and Tavira where it is northeast. Currents on the continental shelf are weak with

maximal velocities of 0.25 m/s flowing eastward parallel to the shoreline (Moita, 1986). This predominant littoral drift is induced by southwest daily winds and storm-waves, eastward directed accumulation of sediments. Waves are originating to 70 % from southwest and 30 % from southeast with maximal significant wave heights (H_S) of 7 and 6 m, respectively, although the wave climate is characterized by a predominantly smooth and moderate sea state (Almeida et al., 2011). Average neap and spring tides ranges from 1.3 to 2.8 m with maximum of 3.5 m (Ciavola et al., 1997). Main contributors to the sedimentation on the continental shelf of Algarve are cliff erosion and the input of the Guadiana River (Andrade, 1990). Generally, only the fine particles are deposits in the shelf because sands are directly transported eastward when reaching the continental shelf. Although, a study of Magalhães (2001) shows that 86 % of the fine-grained material is transported further offshore to beyond the outer shelf. The resulting general surface sediment pattern is a sandy inner shelf, a muddy mid shelf and a patchy sandy outer shelf with some rocky outcrops (Lobo et al., 2004).

In April 2017, during the ASTARTE final meeting in Baleares Island, Drago et al. (2017) presented the results of a multidisciplinary study based on 6 cores located offshore Quarteira (south Portugal) that included sedimentological (grain-size, carbonate, organic matter content), geochemical (major and minor elements) and magnetic (magnetic susceptibility, natural remnant magnetization, etc.) analyses. The study allowed the identification of 13 layers (that were named as "anomalous layers") within the 6 cores that exhibit characteristics interpreted as corresponding to high energy events (Drago et al., 2018). Dating methods (^{14}C and ^{210}Pb) of these layers, 4 related, probably, to the 1st of November 1755 Lisbon tsunami event.

1.6. Objectives

A previous multidisciplinary study was not able to confirm a tsunamigenic origin of high-energy event layers (HEEL) in the cores located offshore of the Algarve coast, Portugal. Although distinct layers were dated to be deposits by the 1755 Lisbon tsunami. The present study aims thus to confirm their tsunamigenic origin by presenting new high-resolution sedimentological proxies. The sedimentary record of a tsunami event is intimately related with the resuspension of seafloor sediments due to the action of the 'tsunami wave' and the transport of allochthonous material (e.g. pebbles and shells) from land or near shore areas to offshore by backwash currents.

The main objective of the present work is to find evidences to identify those previous detected HEEL as offshore tsunami sediments in an outer continental shelf environment. A lot of proxies were already used in previous studies (Drago et al., 2016), therefore more detailed high-resolution methodologies are needed. First, a high-resolution study of the terrigenous/biogenic sand component (see chapter 1.4.6) profile along the sedimentary record above, below and within the detected layers of previous studies will be undergone. Hereby, possible differences between 'tsunami layers' and the normal background sedimentation are expected because of their different sedimentation processes and their origin of source material. Beforehand, a pilot study will justify details of this new methodology in tsunami research. Second, differences on the microtextural surface features of quartz grains (see chapter 1.4.7) within the mentioned intervals will be studied. Expected results are different percentages of surface textures produced by other collision regimes and source effects. The study of microtextures on quartz grain surfaces represents one of the first in this environment and will contribute by broadening the application of this methodology.

Minor objectives are to elaborate dynamics of offshore tsunami sedimentation and to distinguish differences between other high-energy events with the help of tsunami wave modelling and geological considerations. The new techniques in tsunami sediment identification in deeper offshore environments will contribute to the 'toolkit' of tsunami deposit identification as proposed in recent works (Quintela et al., 2016; Tyuleneva et al., 2018).

2. Methods

2.1. Material

Potential tsunami layers will be studied on samples of three gravity cores. One core, POP2 (POPEI2-1CGP), was collected in the scope of the POPEI project (FCT-POCTI/MAR/55618/2004) in 2008 while the two other cores M106 (MW14-GC-106) and M107 (MW14-GC-107) were collected during a Spanish cruise in the scope of the MOWER project (CTM 2012-39599-C03) in 2014. All three cores are located on the continental shelf off Faro, in the Algarve, south Portugal (**Figure 2**). Cores were obtained from water depths between 56.76 m and 90.81 m and core lengths are ranging between 1.25 m and 3.52 m (**Table 2**). All cores were subsampled in 1 cm intervals and preserved at a temperature of 4°C. For all cores, X-ray fluorescence parameters, magnetic parameters, grain-size, ^{14}C, and ^{210}Pb dating were already acquired in the scope of the ASTARTE project and some layers named as 'anomalous' layers possible corresponding to the 1755 Lisbon's tsunami sedimentary record (Drago et al., 2016, 2018).

Table 2: Information about the cores of this study. Name, coordinates, water depth, and length.

Name	Acronym	Longitude [°W]	Latitude [°N]	Water Depth [m]	Length [m]
POPEI2-1CGP	POP2	-8.06	36.89	84.5	1.8
MW14-GC-106	M106	-8.07	36.89	90.81	3.53
MW14-GC-107	M107	-7.99	36.93	56.76	1.25

Drago et al. (2016) describes, that the colour of the sediment in all cores is varying between light olive grey (5y 5/2) to olive grey (5Y3/2) on the Munsell colour chart. Also, no distinct structures besides bioturbation are visible and sediments are quite homogenous, except of core M107 which shows are very chaotic, massive and unstructured facies at the base with large shells and shell fragments. For all the cores a general fining upward trend with many shell fragments towards the base is present, indicating a transgressive succession with decreasing energy depositional regimes from the bottom to the top of the cores. Along whole core depths (**Table 2**) M106 and POP2 mean grain is ranging from 50 µm at the base to ca. 15 µm at core tops. Mean grain size of core M107, which is in general slightly coarser than the two others, ranges from 200 µm at base to ca. 20 µm at core top. Also, predominant textural type is sand in

core M107 in core depths lower than 40 cm, while in cores MW106 and POP2 silt is predominant with percentages of 40 -70 % (Drago et al., 2016).

2.2. Age Modelling

The age estimation models of the three cores are based on Accelerator Mass Spectrometry (AMS) ^{14}C-dating and ^{210}Pb-dating. With the ages obtained from the age estimation analyses (**Table 3** and **Table 4**) ages were projected on core depths using Bayesian statistics with the help of package 'rbacon' (Blaauw and Christen, 2011) implemented in the software 'R'.

Table 3: Results from the Pb^{210} analysis (total and excess). SR = Sedimentation Rate. For more information see Drago et al. (2016).

	POPEI2-1CGP		MW14-GC-106		MW14-GC-107	
SR	0.24 cm / year		0.28 cm / year		0.081 cm / year	
Level [cm]	^{210}Pb-total	^{210}Pb-excess	^{210}Pb-total	^{210}Pb-excess	^{210}Pb-total	^{210}Pb-excess
0.5	194	173.2	202	182.2	116	97.8
1.5	-	-	-	-	-	-
2.5	197	176.7	165	143.7	123	101.6
4.5	150	127.4	-	-	62	40.5
7.5	138	118.6	112	88.6	27	8.9
10.5	-	-	88	63.9	23	5.0
13.5	62	41.3	80	59.4	-	-
15.5	-	-	70	50.7	-	-
19.5	39	15.8	38	14.8	-	-
24.5	-	-	34	13.1	-	-

This approach divides the core in several small vertical sections (here 5 cm sections were chosen for all cores) and uses Markov Chain Monte Carlo (MCMC) iterations to estimate accumulation rates for those sections. Thus, no constant accumulation rate between dated levels must be assumed, resulting in better accumulation rate estimations (Blaauw et al., 2018). Radiocarbon ages were corrected using the calibration curve 'Marine 13' (Reimer et al., 2013) coupled with an elaborated marine reservoir effect value (ΔR) for the core location (**Figure 2**). ΔR was elaborated by using the database of 'CALIB' (http://calib.org/marine/, 06/09/2019) by entering the approximate core location and choosing the 20 closest points. Out of those 20 listed results, only points from the south coast of Portugal were chosen excluding also points originating from fresh water influenced areas as for example the Ria Formosa (lagoon). The

resulting estimated marine reservoir age effect is $\Delta R = 268 \pm 122$ based on 9 points out of this database (Monge Soares, 1993 (http://calib.org/marine/references.php)).

Table 4: Radiocarbon ages obtained from the 3 cores. Calibrated radiocarbon ages are minimum and maximum values of calibrated ages using 'rbacon' (Blaauw and Christen, 2011) (see text in chapter 2.2 for more details).

Depth [cm]	Laboratory Reference	Material	Conventional Radiocarbon Age ± σ [yrs]	Calibrated Radiocarbon Age [yrs]
POPEI2-1CGP				
60.5	Beta-457926	Shell	660 ± 30 BP	1451 – 1750 CE
89.5	Beta-457927	Shell	1240 ± 30 BP	1019 – 1451 CE
132.5	Beta-463038	Foraminifera	2130 ± 30 BP	230 – 745 CE
158.5	Beta-463039	Foraminifera	2670 ± 30 BP	313 BCE – 270 CE
MW14-GC-106				
100.5	Beta-463031	Foraminifera	780 ± 30 BP	1446 – 1686 CE
135.5	Beta-463032	Foraminifera	910 ± 30 BP	1200 – 1529 CE
175.5	Beta-463033	Foraminifera	1450 ± 30 BP	875 – 1247 CE
215.5	Beta-463034	Foraminifera	1620 ± 30 BP	491 – 940 CE
265.5	Beta-457936	Shell	2340 ± 30 BP	103 BCE – 406 CE
318.5	Beta-457937	Shell	3120 ± 30 BP	838 – 245 BCE
350.5	Beta-463035	Foraminifera	3950 ± 30 BP	1381 – 578 BCE
MW14-GC-107				
28.5	A1610401	Shell	1380 ± 40 BP	973 –1503 CE
68.5	A1610401	Shell	3380 ± 30 BP	1472 – 523 BCE
90.5	A1610401	Shells + Gastropods	5260 ± 30 BP	3494 – 2159 BCE
110.5	Beta-457940	Shell	5600 ± 40 BP	4301 – 3410 BCE

Excess ^{210}Pb ($^{210}Pb_{ex}$) was calculated by subtracting the supported fraction from the total. Then $^{210}Pb_{ex}$ profiles of the cores were used to calculate mean sedimentation rates (**Table 2**) by using exponential interpolation of $^{210}Pb_{ex}$ values, assuming constant rate of deposition (Robbins, 1978). In contrast to ^{14}C – ages, ^{210}Pb – ages were used as absolute dates within the age-depth model, with an error estimate of 1 year. Previous detected layers, that are interpreted to correspond to high energy events (Drago et al., 2016) (see chapter 1.5) were speculatively considered as sections of instantaneous accumulation of sediments. Hence, these layers were excised before modelling to further enhance the age-depth relations.

2.3. Sedimentological Composition

For the sedimentological composition, pre-selected layers were chosen to be studied. In each core samples 10 cm below and above the HEELs referred in Drago et al. (2016, 2018) as "anomalous layers" are studied (**Table 5**), to detect possible differences between high energy events and the normal marine background sedimentation layers, and also for comparison for sediment component patterns before, during and after the HEEL in the three cores. In core M106 the samples of the levels 75 – 76 cm (within the HEEL) and 55 – 56 cm (within the post HEEL) are missing, resulting in a total amount of 78 samples that are studied in the present work (**Table 5**).

Table 5: Sections of pre high energy layer (HEEL), HEEL and post HEEL and full sections of the 3 cores that will be analyzed for their sediment composition in the present study. Distance from top in cm. SN = Sample Number.

Core	Section [cm] (SN)	Pre HEEL [cm] (SN)	HEEL [cm] (SN)	Post HEEL [cm] (SN)
POPEI2-1CGP	80 – 50 (29)	60 – 50 (10)	70 – 60 (9)	80 – 70 (10)
MW14-GC-106	80 – 52 (26)	52 – 62 (10)	70 – 62 (7)	80 – 70 (9)
MW14-GC-107	32 – 8 (24)	18 – 8 (10)	22 – 18 (4)	32 – 22 (10)

2.3.1. Preparation of Samples

Samples were wet sieved using a 63 µm mesh, dried (max. 40 °C) and sieved using 2000 µm, 1000 µm, 500 µm, 250 µm, 125 µm and 63 µm meshes. Total weights and weights of the separate fractions are listed in **Annex A**. The organic matter was not destroyed for grain size analysis (to allow the preservation of biogenic components such as charcoal) which resulted in

the formation of aggregates during the drying process in the cores M106 and POP2. Samples of these two cores were treated with a deflocculant (hexametaphosphate) before sieving to eliminate the aggregates. A solution of 0.04 g*ml^{-1} sodium hexametaphosphate ($Na_6O_{18}P_6$) was prepared. For 10 ml distilled water, 3 drops of the sodium hexametaphosphate solution were mixed with the sediments in each sample. Samples were then mixed using an ultrasonic cleaner for ~ 10 minutes and dried afterwards (max. 40 °C). For mean grain size distribution calculation the Folk and Ward method (Folk and Ward, 1957) was used within the software 'Gradistat' (Blott and Pye, 2001).

2.3.2. Component Classification and Identification

For analysing the sedimentological composition of the samples a binocular (OLYMPUS SZX7) with an OLYMPUS DF PL 2X$_{-4}$ objective and WHSZ10x-H/22 draw tubes was used. Components were classified as terrigenous, biogenic and non-identified and grouped in 11 subgroups (**Table 6**, **Annex B**). Terrigenous components are subdivided in quartz, mica, opaque, aggregate and other terrigenous components. In this group aggregates are purely terrigenous without biogenic elements. Biogenic components are subdivided in planktonic foraminifera, benthic foraminifera, molluscs, terrestrial biogenic and other biogenic components. Terrestrial biogenic components are biogenic components with a continental origin, as for example wood fragments and charcoal. When a clear identification as mollusc or foraminifera is missing it is classified as other biogenic. Non-identified are components where visual identification and simple petrographic methods cannot yield a clear classification in the above-mentioned groups. Components or rather aggregates with both biogenic and terrigenous elements are classified as none-identified. Pictures of specific components were made using a LEICA MZ16 microscope with 1.0x planapochromatic objective, 10x/21B eyepiece and LEICA MC170 HD camera.

Table 6: Classification of sand components

Groups	Components
Terrigenous	Quartz, Mica, Opaque, Aggregate, Other Terrigenous
Biogenic	Planktonic Foraminifera, Benthic Foraminifera, Molluscs, Terrestrial Biogenic, Other Biogenic

2.3.3. Counting Methodology

In micropaleontological studies of fossil assemblages Fatela and Taborda (2002) show that counting 100 elements has satisfactory statistical reliability. Then again, they suggest counting 300 elements of the assemblages is necessary when the study is mainly concerned with detailed quantitative aspects. But because samples were small, some of them did not reach 300 grains. In respect of sample limitations and for further justification of the amount of counts, a preliminary study was conducted using the count-data of 5 samples.

To test whether counting 100 or 300 grains in each sample in this study is statistically significant or result interpretation differ, a pilot study was conducted. A second objective of this pilot study is to test which fraction might be best suited to identify and cluster samples of the HEELs and the normal marine background sedimentation. For this test 5 randomly chosen samples, including 2 high-energy event samples, from the core M107 were analysed. In each sample 100 grains were identified and counted in the fractions 1000-500 µm (0-1 Φ), 500 – 250 µm (1 – 2 Φ) and 250 – 125 µm (2 – 3 Φ). In addition, 300 grains were identified and counted in the fractions 1 – 2 Φ and 2 – 3 Φ using the methodology as described in chapter 2.3.2.

The count of 100 and 300 grains were tested for differences in means using negative binominal regression (NBR) separately for the fraction 1 – 2 Φ and 2 – 3 Φ µm. In contrast to general linear models (GLMs) ordinary linear models like analysis of variance (ANOVA) require model assumptions that cannot be met with count data in general and particularly with the present data set. Also, transformation of the data can lead to less interpretability (O'Hara and Kotze, 2010; Warton et al., 2016). Because the present data set shows overdispersion and an upper boundary with 100 and 300 respectively for the two methods, NBR with a log-link function (e.g. Lawless, 1987) incorporating a fixed offset on a log scale was chosen for the hypothesis testing. Overdispersion was tested by a likelihood ratio test between a negative binomial and Poisson model. The nested log-linear model for the NBR was carried out on the raw count data by the two methods, counting 100 and 300 grains, and by components [1]. The null hypothesis implies that there is no difference when counting 100 or 300 grains and between

[1] R-code (MASS-package): glm.nb(Count ~ offset(log(Denominator)) + factor(Component) + factor(Method) + factor(Component):factor(Method) + factor(Fraction))

the two fractions, whereas the alternative hypothesis implies that there is a statistically difference when counting 100 or 300 grains or between the fractions.

The counts of the 100 grains in the 3 fractions were analysed using principle component analysis (PCA) to establish relations of samples based on their textural composition and hereby suggest the best suited fraction to analyse for the main study. Since PCA is a linear method and hence not adapted to analysis of species abundance data, the counts were pre-transformed using Hellinger-transformation after Legendre and Gallagher (2001). For the PCA the function 'rda' of the r-package 'vegan' (Oksanen et al., 2019) was used.

The results derived from the PCA used in this context are regarded as preliminary results, because the data matrix for the PCA contains a small number of samples compared to the number of variables. Thus, these results might be lacking in robustness.

2.3.4. Microtextural Characteristics of Quartz Grains

Quartz grains were collected for further investigation on grain-surface microtextural features in 3 samples of the M107 core in the 2-3 Φ fraction. Every sample represents 3 different chronological sedimentation regimes: Pre – HEEL, HEEL and post – HEEL (**Table 7**). Of each sample 30 randomly chosen quartz grains were picked up using a binocular microscope. For the microtextural analysis high resolution images of 90 quartz grains were made with a scanning electron microscope (SEM) instrument (IPMA Lisbon, Portugal). Images were processed using the software 'Mirone' (Luis, 2007; http://w3.ualg.pt/~jluis/mirone/main.html) and 'R' for the calculation of area percentages. Following the semi-quantitative approach of Costa et al. (2012a; 2012b) focus was given to 5 microtextural families of grain surface features: angularity, fresh surfaces, percussion marks, adhering particles and dissolution (**Figure 16**). The angularity was scaled from 0 (very rounded) to 5 (very angular) using Power scale (M. C. Powers, 1953). To classify the microtextural occupation of individual grains each textural surface feature was scaled as: 0 (absent), 1 (0-10 % of grain surface), 2 (10-25 % of grain surface), 3 (25-50 % of grain surface), 4 (50-75 % of grain surface) and 5 (> 75 % of grain surface). For more objectivity all image names were given a code name and every image was processed twice to reduce influence of observer interpretation. To aid interpretation of results, p-values were calculated to test if there are statistical differences in mean values of the 3 populations using Kruskal – Wallis test (Kruskal and Wallis, 1952) from the base R-package 'stats' (R Development Core Team, 2017).

Table 7: Samples used for microtextural analysis of quartz grains. HEEL = high-energy event layer. Distance from top in cm.

Core	Layer Depth [cm]	Chronological Regime
MW14-GC-107 (M107)	15 – 14	Post – HEEL
MW14-GC-107 (M107)	19 – 18	HEEL
MW14-GC-107 (M107)	26 – 25	Pre – HEEL

2.3.5. Statistical Analyses

Both univariate and multivariate statistics, namely negative binomial regression (NBR), principal component analyses (PCA) and Kruskal-Wallis test (KW), have been used in the present work.

NBR is a method to model the relations between features and responses. Hence, it is often use to model count data. Unlike general linear models (GLM) NBR uses two parameters, the mean and the dispersion. However, the NBR is mostly calculated like a GLM and the dispersion parameter is calculated afterwards (see Hilbe, 2014). Thus, this statistical model allows to test if there are differences in the response variable between different features.

PCA is a multivariate statistical analysis often used for count data to explore even small variations in a bigger dataset (see Borcard et al., 2018). Hereby, the relation between objects, as the sediment levels, are investigated. This method attempts to find underlying gradients in the dataset and thus to combine the redundancy in a dataset. The resulting principle components (here component assemblages) conflates objects with similar proportional amounts of differing variables (here sand components). After this calculation results are represented in two matrices, the loading matrix and score matrix. Loadings have values between -1 and 1 for every variable. This value describes the proportion of the respective principle component, whereby values > 0.4 are considered as significant (Malmgren and Haq, 1982). Scores are either negative or positive, describing the proportion of a variable to the respective principle component. Results of the PCA are displayed in 2 different ways. First, the generated PCA-loadings (**Annex D**) of each component assemblages (principle components) are plotted against the core depths, showing the sequence of the component assemblages. Component assemblages were merged using the scores of each component (variable) for the respective principle component. Second, PCA-biplots are displayed, showing the spatial distribution of the samples and their responsible vectors, the components. Here, the axes of the biplots were chosen by a compromise to have the most explained variance (usually principle component 1 and 2) and showing the greatest

difference between “tsunami” and “non-tsunami” samples. Thus, component assemblages are chosen by having either high positive correlations (loadings) or high negative correlations for the levels within the high energy event layer.

KW are used to find differences between several classificatory groups (here samples) having the same continuous dependent variable (here microtexture percentage). The KW is based on an analysis of variance, examining if pivotal quantities of several independent random samples differ from each other The null-hypothesis implies that there are no differences between groups. Therefore, p-values lower than the significant level (here > 0.005) are implying a difference between the groups.

Note that all statistics have been computed using the software ‘R’ (R Development Core Team, 2017). Distinct ‘R’ – packages of important functions and other software that were used to obtain results of the present study are named and cited in the respective chapters. All utilized software can be downloaded and used free of charge.

2.4. Numerical Modelling of the 1755 Tsunami

For simulations of tsunami event time frame as times between waves and backwash currents, as well as for wave characteristics of the incoming tsunami wave a numerical model was conducted. The preparation of the bathymetry grids and the initial condition of the tsunami wave were made with the program Mirone (Luis, 2007) . The tsunami waves were modelled using the NSWING (Non-linear Shallow Water model wIth Nested Grids) code (Miranda et al., 2014) [2]. The 1755 earthquake source parameters were selected from previous studies that modelled a 1755 Lisbon alike maximum credible earthquake scenario. Therefore, the initial conditions of the wave were produced by the offset of two faults, the Horseshoe Abyssal Thrust Fault (HF) and the Marquês de Pombal Fault (MPF). This multi-fault scenario is suggested as an candidate source of the 1755 earthquake and tsunami (Matias et al., 2013; Tavares, 2014). Also, both HF and MPF scenario were considered as stand-alone triggering fault causing the 1755 Lisbon earthquake and tsunami (Omira et al., 2009; Omira et al., 2012; Ramalho et al., 2018). The fault parameters that triggered the earthquake and tsunami are listed in **Table 8**. To improve the resolution of the model a nested grid approach with 2 different bathymetry grids (source: http://w3.ualg.pt/~jluis/mirone/data-links.html, 06.07.2019) with different resolution (~250 m and ~10 m closer to the coast) was conducted. For time series data of the wave

[2] Model input-code: nswing.exe layer0.grd multi_initial.grd -1layer1.grd -t2 -N6000 -Zoutput,30 -M -M- -M+ -f -T1,mare_all.dat -S+m+s -D

properties (wave height, velocity, velocity angle and period) at the core positions (**Table 2**) three tide gauges with coordinates of the core location were simulated within the tsunami model (mareographs). Horizontal velocities (U_x) are calculated with equation (1):

(1)

$$U_x = \sqrt{v_{longitude} + v_{latitude}}$$

For reducing the noise in the mareographs a smoothing operation was conducted using a generalized additive model (GAM) within the *geom_smooth()*-function of ggplot2 (Wickham, 2016). For evaluating the energy transferred to the bottom velocities of the landward propagating tsunami waves are calculated using equation (2) assuming the theoretical considerations of Weiss and Bahlburg (2006). U_{surf} is the velocity at the surface but since tsunamis are shallow water waves due to their enormous wavelengths $U_{sur} = U_{bottom}$ can be assumed (e.g. Weiss and Bahlburg, 2006).

(2)

$$U_{sur} = \frac{2\pi A}{T} \frac{\cosh(2\pi \frac{d}{L})}{\sinh(2\pi \frac{d}{L})}$$

Equation (2) is based on Bernoulli's theorem (e.g. Allen, 1985) and assumes (i) that fluid is incompressible and inviscid and (ii) that harmonic functions describes the wave orbits. Also, it assumes, that (iii) only the horizontal component is required for the drag to set grains in motion. In equation (2) A is the amplitude, d is the depth (here mean water depth of core locations = 77.36 m), L is the wavelength and T the wave period.

Table 8: Source parameters for the 1755 Lisbon Tsunami as proposed by Matias et al. (2013).

Structural Fault	Epicentre: Lat.; Long.	M_w	Depth	Plane: Φ; δ; λ	Dimension: L; W	Fault Slip	Fault Area
Marquês de Pombal Fault (MPF)	35.796; -9.913	8.75	5 km	23°; 45°; 90°	60 km; 120 km	10 m	7.2 x 10^3 km
Horseshoe Thrust Fault (HF)	36.574; -9.890		5 km	235°; 45°; 90°	150 km; 120 km	10 m	18 x 10^3 km

Latitude (Lat.) and Longitude (Long.) in decimal degrees are assumed values, Magnitude in Moment Magnitude (Mw) is a computed value.

3. Results

3.1. Age Models

Results of the age modelling of the cores are displayed in (**Figure 3**, **Figure 4** and **Figure 5**) and age models reflect increasing uncertainties with greater distance from calibrated sample ages (blue probability distributions). The pre-detected high energy event layers (grey horizontal bars) assume abrupt accumulation, different to the other core sections. The age model of core POP2 (**Figure 3**) suggest an age of ca. 321 BCE at the base, resulting in a mean accumulation rate of ~ 0.077 cm/year for the entire core. For the studied section of POP2, between 80 and 50 cm, single best model age interval of 1357 CE to 1655 CE were determined.

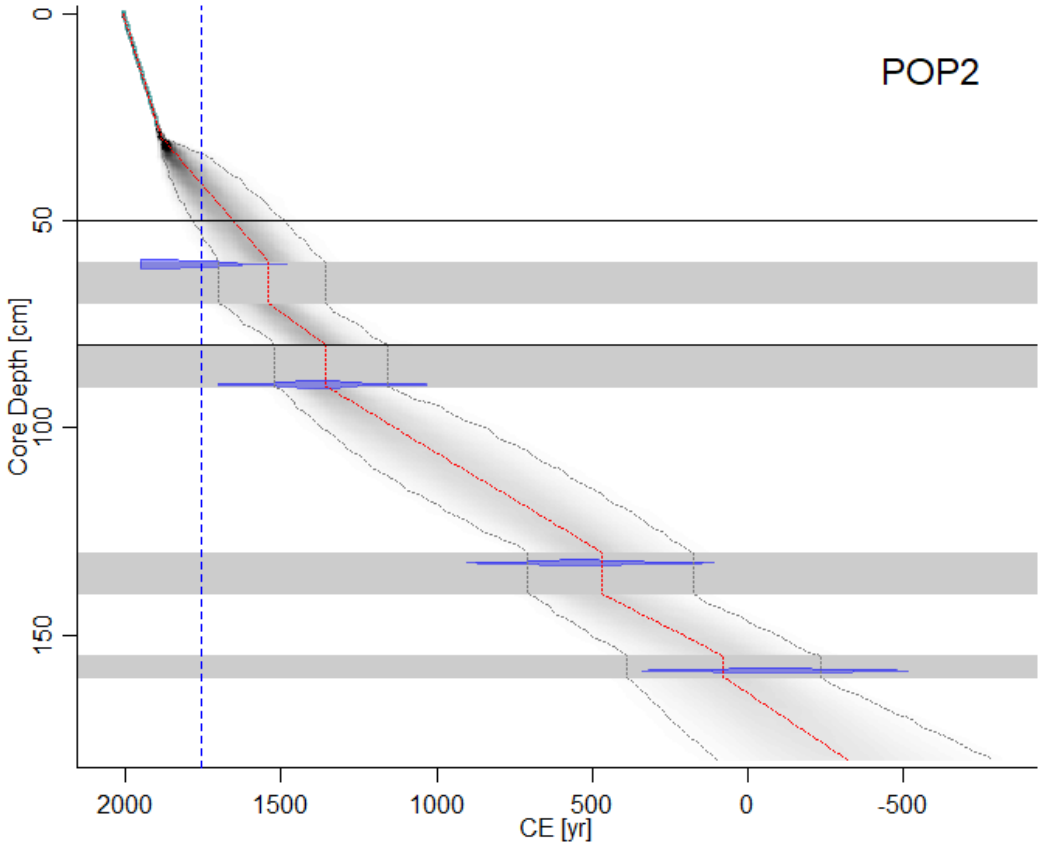

Figure 3: Age depth model output for the core POP2 including calibrated ^{14}C -ages (transparent blue). Red curve shows single 'best' model based on the weighted mean age for each depth. Darker grey indicates CE-ages that are more likely and dashed grey lines represent the 95 % confidence intervals (max. and min. CE-ages). Horizontal grey bars represent the anomalous layers detected by Drago et al. *(2016)*. Black horizontal lines show the studied core section and the blue dashed line indicates the year 1755 CE.

Regarding the 1755 tsunami event, this implies that the studied section cannot be clearly related to this event, although maximum age of the 95 % confidence interval includes the year

1755 CE in the studied section at level 53 cm. This result suggests, that the section in core POP2 needs to be extended to fully include event sediments related to the 1755 tsunami.

The age model of core M106 (**Figure 4**) suggest a mean age of 766 BCE at the core base. The consequent mean accumulation rate for the entire core is ~ 0.21 cm/year. In general, the accumulation rate within this core decreases with greater core depths. The studied section, 80 cm to 52 cm core depth, includes single best model ages from 1676 CE to 1790 CE, clearly relating the 1755 Lisbon event to this core section. Suggested mean age for the tsunami layer (70 – 60 cm core depth) is 1733 with an 95 % confidence interval from 1627 CE to 1818 CE.

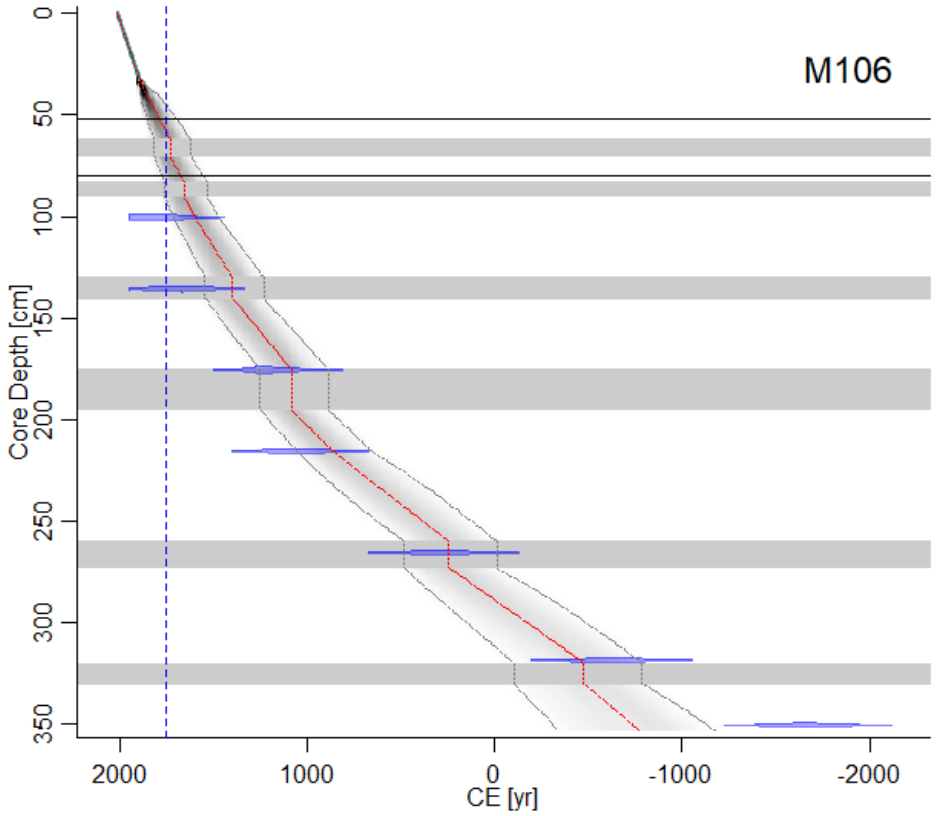

Figure 4: Age depth model output for the core M106 including calibrated 14C -ages (transparent blue). Red curve shows single 'best' model based on the weighted mean age for each depth. Darker grey indicates CE-ages that are more likely and dashed grey lines represent the 95 % confidence intervals (max. and min. CE-ages). Horizontal grey bars represent the anomalous layers detected by Drago et al. (2016). Black horizontal lines show the studied core section and the blue dashed line indicates the year 1755 CE.

Core M107 includes the longest chronological sedimentary sequence of the 3 studied cores with a suggested age of 3879 BCE for the base of the cores (**Figure 5**). Hence, mean accumulation rate throughout the entire core is the lowest compared to the 3 cores with ~ 0.021 cm/year. The studied core section is including single best model ages from 1152 CE to 1915 CE and 95 % confidence interval ages from 826 CE to 1916 CE. The 1755 Lisbon tsunami can be related to the proposed tsunami layer (22 cm to 18 cm core depth), because this age lies within the 95 % confidence interval of the corresponding core depths. Estimated single best model age for the tsunami layer is 1656 CE with a 95 % confidence interval between 1386 CE and 1809 CE.

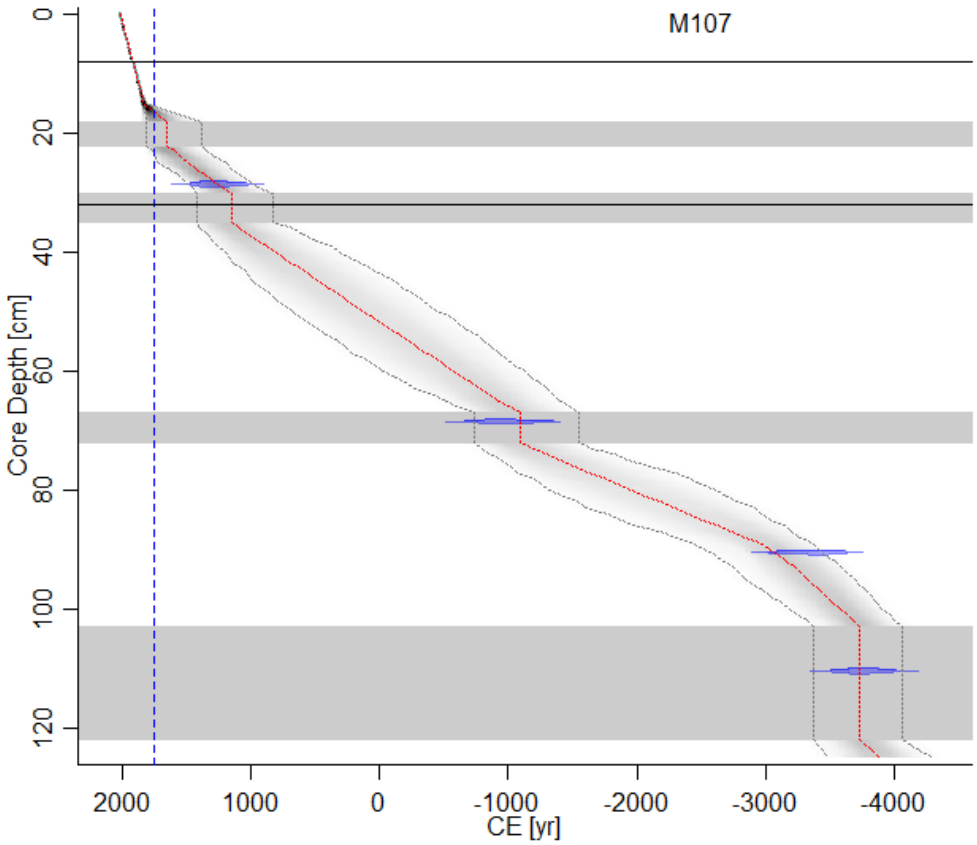

Figure 5: Age depth model output for the core M107 including calibrated ^{14}C -ages (transparent blue). Red curve shows single 'best' model based on the weighted mean age for each depth. Darker grey indicates CE-ages that are more likely and dashed grey lines represent the 95 % confidence intervals (max. and min. CE-ages). Horizontal grey bars represent the anomalous layers detected by Drago et al. *(2016)*. Black horizontal lines show the studied core section and the blue dashed line indicates the year 1755 CE.

HEEL in the studied core sections are related to the 1755 tsunami event, although core POP2 is lacking accuracy in the correlation to this event. Therefore, HEEL will from now on speculatively be called tsunami layer. Likewise, the sections before and after the HEEL are named as pre and post tsunami sections.

3.2. Justification of Count Numbers

Within the component percentages of the two different methods, counting 300 and 100 grains, there are generally only a few apparent differences (**Figure 6**). In the coarser fraction 500-250 µm (1-2 Φ) differences of ~ 15 % can be seen between the two methods of the quartz-grains percentages in level 15 – 16 cm and 25 – 26 cm. In level 21 – 22 cm percentages of other biogenic components differ 10 %.

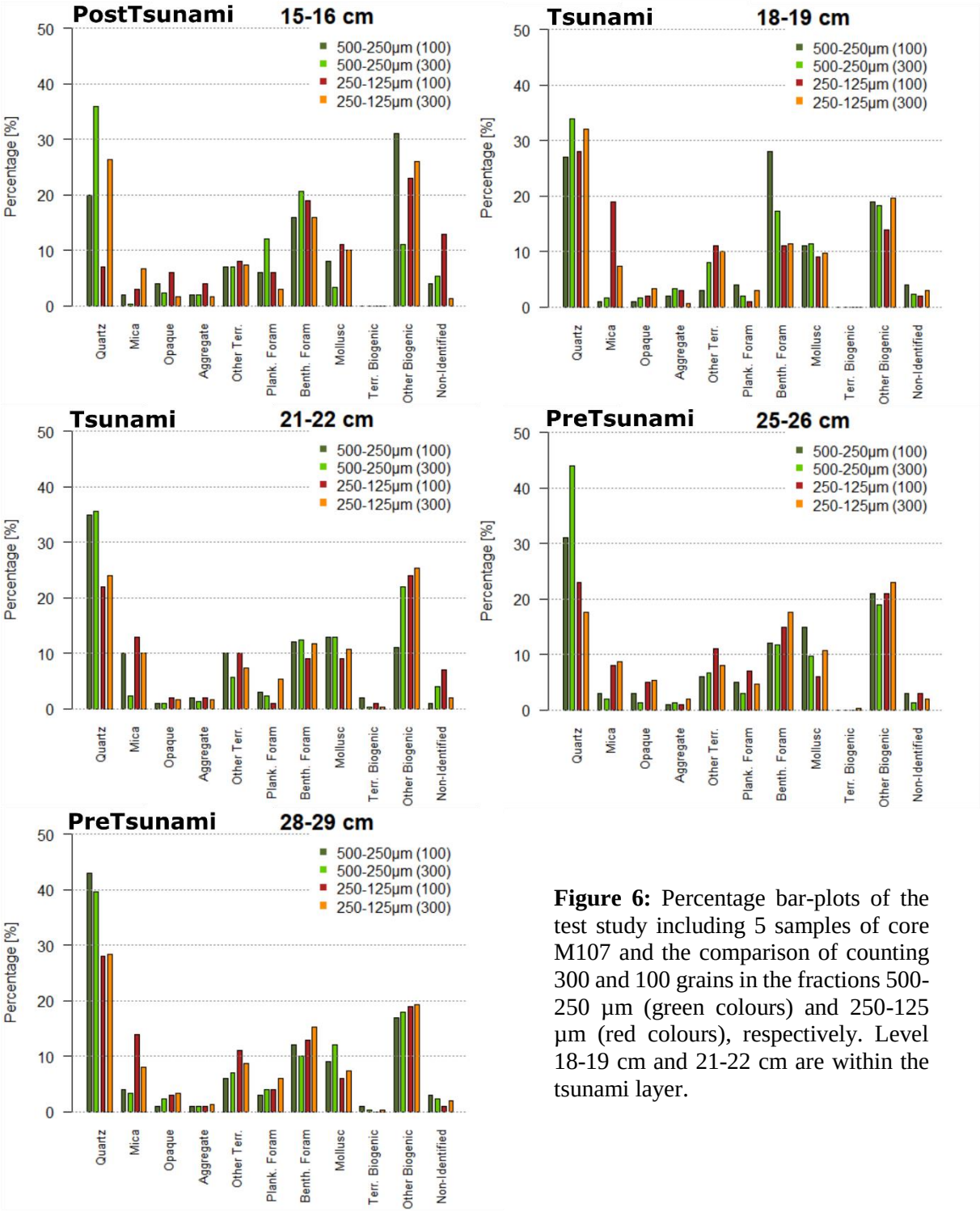

Figure 6: Percentage bar-plots of the test study including 5 samples of core M107 and the comparison of counting 300 and 100 grains in the fractions 500-250 µm (green colours) and 250-125 µm (red colours), respectively. Level 18-19 cm and 21-22 cm are within the tsunami layer.

Percentages of other biogenic components are ~ 12 % higher when 100 grains were counted compared to 300 counted grains. In level 18 – 19 cm benthic foraminifera have ~ 10 % distinction. In the finer fraction 250-125 µm (2-3 Φ) level 15 – 16 cm quartz-grain percentages have almost 20 % differences between the two methods. In the same level non-identified components differ in 10 %. Mica percentages show higher differences in the finer fraction in level 18 – 19 cm and 28 – 29 cm with ~ 11 % and ~ 7 %, respectively. In all other component percentages differences are < 5 %. When compared the two different fractions have minor differences. However, there is a clear trend of higher percentages of quartz and lower percentages of mica in the coarser fraction.

Results of the negative binomial regression are listed in (**Table 9**). As expected, the sources (factors) 'component' and 'fraction' are statistically significant and the null-hypothesis can be rejected. Source 'method' and the nested related source 'component:method' are not statistically significant with p-values of 0.31 and 0.24, respectively. This implies that the null-hypothesis can be accepted and there is no statistical difference in this data set by counting 100 or 300 grains. Another implication is, that fractions affect the number of different components because source 'fraction' is significance, although it is around 0.1.

Table 9: Pilot-study summary of the negative binomial regression model for the 250-125 µm (red) and 500-250 µm fraction (see chapter 2.3.3). Df = degree of freedom, Dev = deviance, Res. Df = residuals degree of freedom, Res. Dev = residuals deviance. Significant sources (factors) are highlighted with red colour.

Source	Df	Dev	Res. Df	Res. Dev.	P value	Significance
Component	10	1370.69	209	243.26	< 2e-16	***
Method	1	1.02	208	242.25	0.31367	
Fraction	1	2.74	207	239.51	0.09799	.
Component:Method	10	12.73	197	226.78	0.23924	

Significant codes: 0 '***' 0.001'**' 0.01 '*' 0.05 '.' 0.1 '-' 1

In conclusion, results of this preliminary study suggest counting 100 instead of 300 grains is reliable and does not reduce the quality of information for the geological interpretation. A further implication of those results is that fractions, as expected, have an influence within this methodology. Thus, it is necessary to establish the best suited fraction for the sediment composition analysis.

To follow the statistical analysis of NBR-results, principle component analysis was conducted to see which fraction has greatest difference between tsunami related layers and layers of the normal background sedimentation. In the PCA-biplots (**Figure 7**) components are

illustrated as vectors controlling the spatial distribution of the samples. Principle components 1 and 2 were chosen to get the most explained variance in every fraction (> 85%). The fraction 2-3 Φ shows a differentiation between high-energy event samples and samples of the normal background sedimentation regime. Vectors that are responsible for this difference are mainly the components mica and terrestrial biogenic while components planktonic and benthic foraminifera shells are pointing in the opposite direction. In the two other fractions no clear

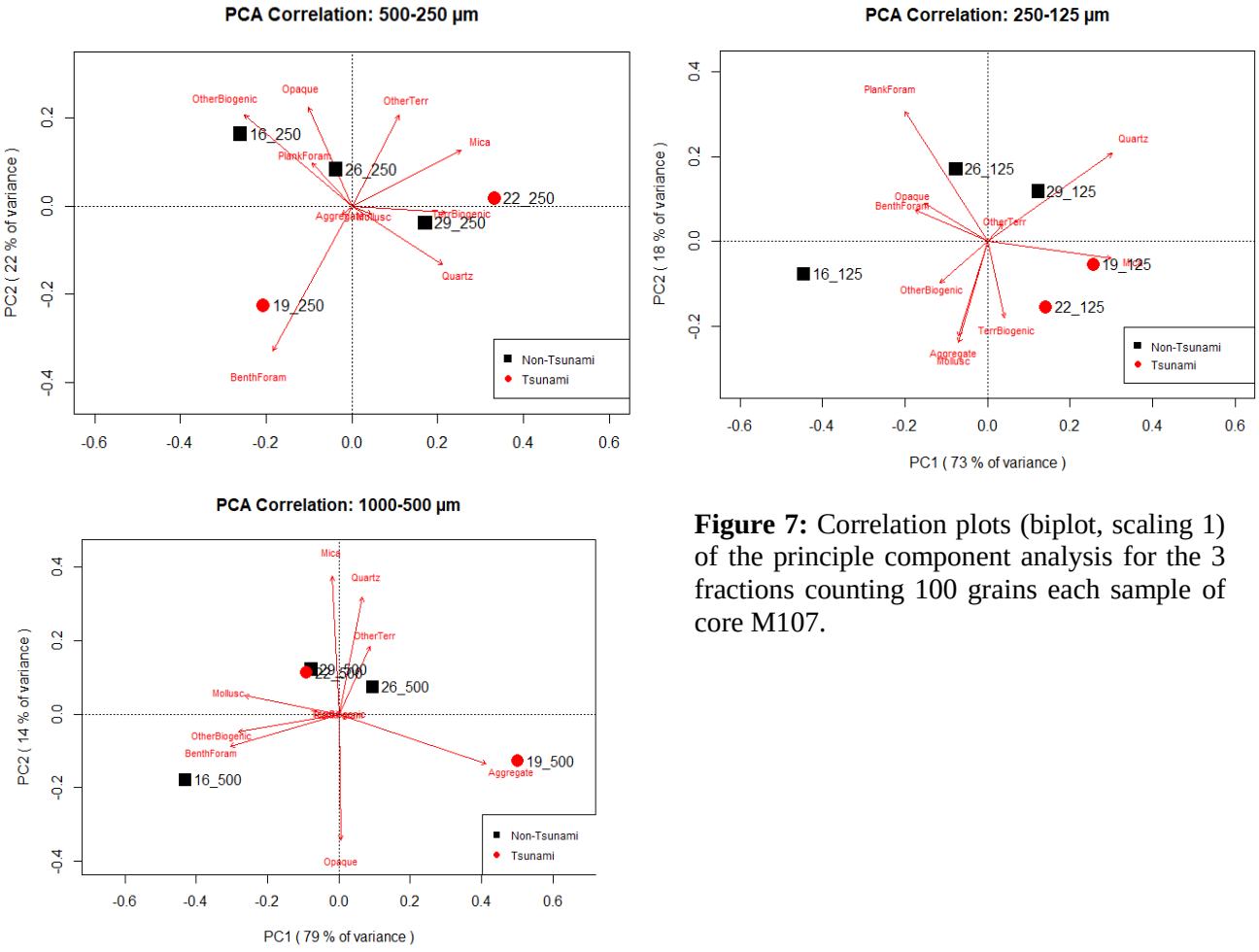

Figure 7: Correlation plots (biplot, scaling 1) of the principle component analysis for the 3 fractions counting 100 grains each sample of core M107.

differentiation between the two type of samples can be observed. Thus, the component quartz has a slight correlation with the two tsunami samples. Therefore, PCA-results suggest using the 2-3 Φ fraction for the sand composition analysis because differentiation of tsunami and non-tsunami samples is more significant. Also, results show that PCA is an appropriate tool to illustrate and visualize differences between tsunami and non-tsunami samples even when the difference is small and not clearly visible with common illustrations as bar plots (**Figure 6**).

3.3. Mean Grain Size Distribution of the Sand Fraction

Results of the grain size analysis is based purely on the sand fraction 2000 – 63 µm (-1 – 4 Φ). In general cores POP2 and M106 have less variation and lower values of the mean grain size of the sand fraction than core M107 along core depths (**Figure 8**).

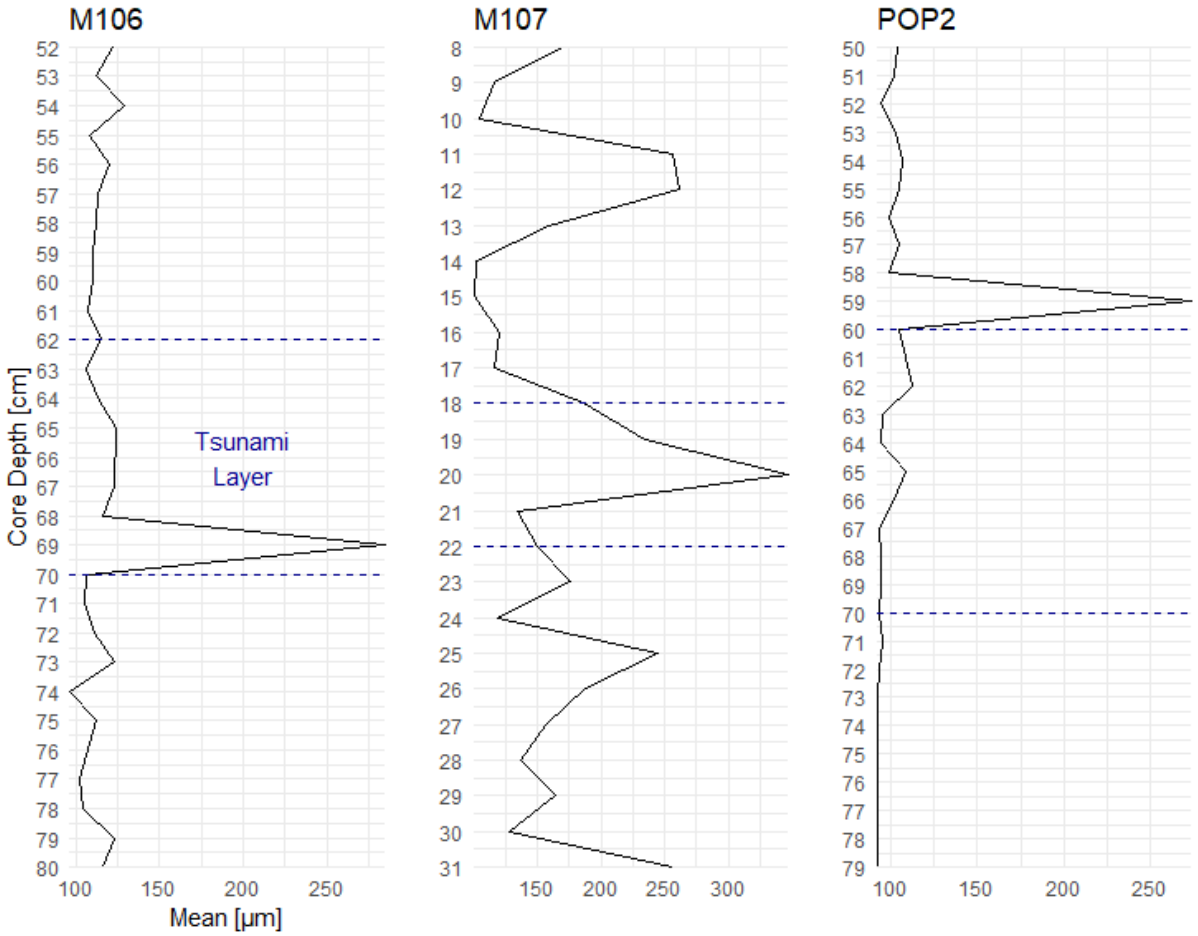

Figure 8: Grain size analysis: Mean grain size distribution resulting from the sieving. Blue dashed lines represent boundaries of the tsunami layer. Blue dashed lines represent the tsunami layer boundaries in each core. Note the different scale in core M107 compared to cores POP2 and M106.

However, in both finer cores, M106 and POP2, there are 2 anomalous peaks in mean grain size at level 69 cm and 59 cm, respectively. Bot peaks correspond to mollusc shells in the fraction > 2000 µm (-1 Φ). Since the amount of sample is very low both shells contribute to a large amount of the total weight of sample, thus distort the grain size distribution curve. Interestingly, both shells are close to the boundary of the tsunami layer. Mean grain size in core M106 is varying from 97 to 129 µm and a tends to coarsen up towards the top of the studied section. Core POP2 also coarsening up towards the top and mean grain size is varying between 92 and 111 µm. In core M107 mean grain size is varying from 100 to 347 µm and there are 4

pronounced maxima at level 31, 25, 20 and 12 cm. Regarding the high energy event layer, both finer grained cores POP2 and M106 do not show any pronounced pattern in mean grain size, except the extremes/outliers corresponding to the mollusc shells in the fraction > -1 Φ. However, in core M106 exist a small plateau in mean grain size ranging from core depths from 67 to 65 cm, in the middle of the tsunami layer, with values of ~ 123 µm. Only in core MW107 there is a pronounced increase in mean grain size in the high energy event layer and a maximum at level 25 cm near the beginning of the tsunami layer with an increase of 347 µm.

3.4. Sand Composition

For the sand composition a total of 79 samples, originating from 3 cores, were analysed. By counting and identifying 100 grains in each sample a total of 79000 grains were analysed (**Annex C**), while 385 (< 5 %) of those were kept unidentified, mostly because these grains were aggregates containing both biogenic and terrestrial constituents. Samples with > 5 % of non-identified components of are listed in **Table 10**.

Overall, components show minor fluctuation in their percentages in all 3 cores (**Figure 9**). Also, general differences in sand composition between the 3 cores are displayed: Core M107 has high percentages of terrigenous components with ca. 50 % compared to core M106 with around 30 % and core POP2 with around 25 %. Besides, percentages of benthic foraminifera are high, and percentages of molluscs are low in the latter cores compared to core M107.

Table 10: Levels with > 5 % of non-identified components of total counts.

Core	Levels [cm] (% of non-identified)
MW14-GC-106 (M106)	52-53 (7), 67-68 (7), 68-69 (6), 71-72 (6), 77-78 (6), 78-79 (6), 80-81 (9)
MW14-GC-107 (M107)	15-16 (13), 21-22 (7)
POPEI2-1CGP (POP2)	50-51 (7), 51-52 (8), 53-54 (5), 54-55 (6), 55-56 (7), 56-57 (7), 57-58 (6), 58-59 (7), 59-60 (11), 61-62 (9), 62-63 (11), 63-64 (12), 64-65 (11), 65-66 (9), 66-67 (16), 67-68 (8), 68-69 (7), 69-70 (9), 70-71 (12), 71-72 (8), 73-74 (8), 74-75 (10), 75-76 (8), 76-77 (8), 78-79 (5)

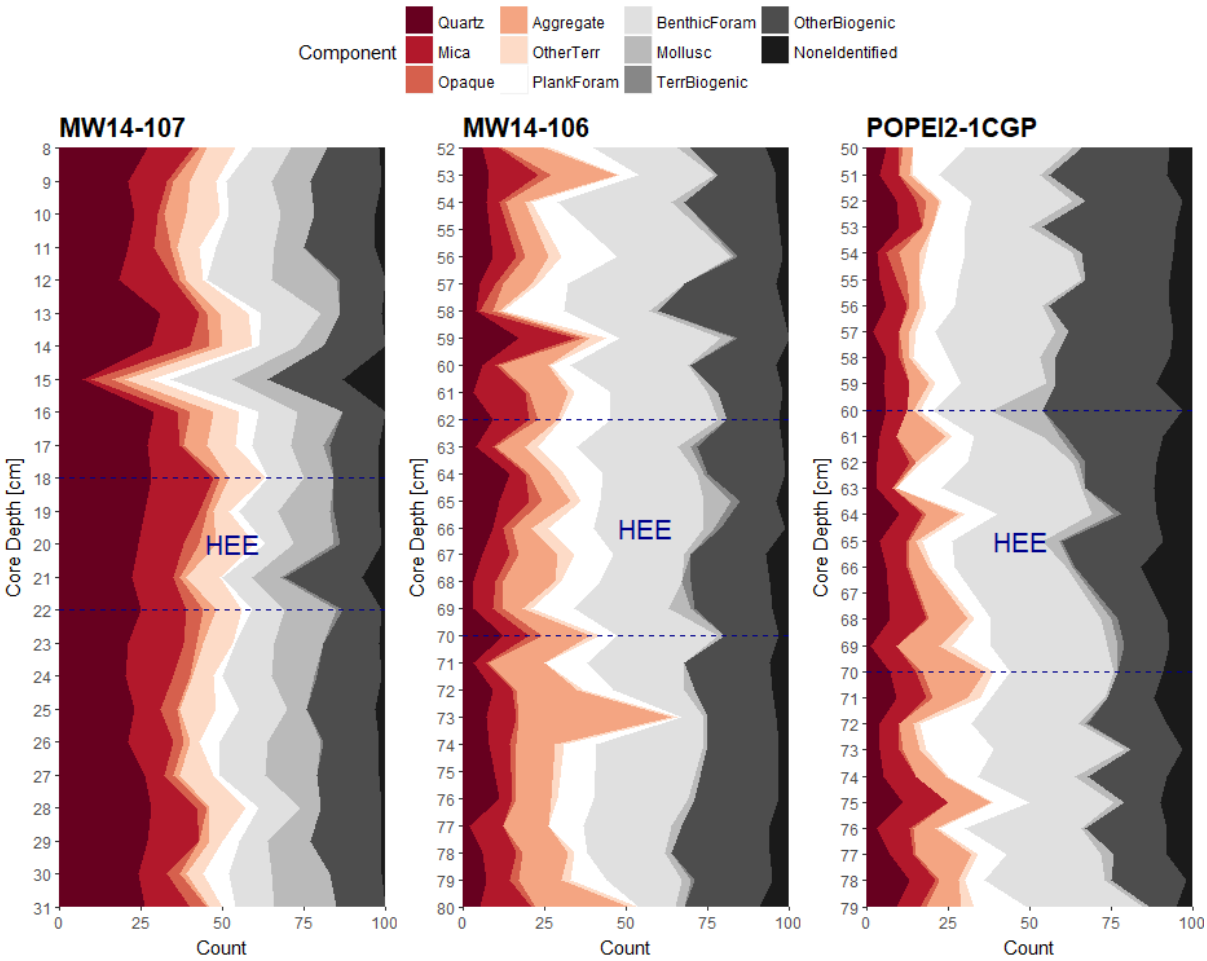

Figure 9: Percentage of each component along core depth in all 3 cores. Red colours show terrigenous components while black and white colours show biogenic and none-identified components. HEE = high-energy event layer. OtherTerr = other terrestrial, PlankForam = planktonic foraminifera, BenthForam = Benthic Foraminifera, TerrBiogenic = Terrestrial Biogenic.

Core M107 show a slight trend of decreasing biogenic components towards the top of the studied section, with one maximum in level 15 cm. Another maximum of biogenic components is present in level 21 cm and both of those maxima have also a peak of non-identified components. The terrigenous part is made up of mainly quartz and mica, while opaques, other terrigenous components and aggregates are low on percentages (< 8 %). The biogenic components are mainly other biogenic, molluscs and benthic foraminifera. Terrestrial biogenic components have very low percentages throughout the studied core section.

Although core M106 shows fluctuations in the sand composition there is no general trend in the studied section. There are 4 maxima in terrestrial components at level 80 cm, 73 cm, 59 cm and 53 cm with percentages higher than 50 % and none of them occur in the tsunami layer. In every level, except of the maximum at level 73 cm, all terrigenous components increase, while at level 73 cm the maximum of terrigenous components is present due to the

increase of mainly aggregates. In general, the terrigenous part in this core is mainly quartz, mica and aggregates, while opaques and other terrigenous components are underrepresented. The biogenic part is dominated by other biogenic components and benthic foraminifera (up to 25 %), but also planktonic foraminifera contribute to the total biogenic components with up to 10 %. Molluscs and terrestrial biogenic components are low in this core with maximal percentages of ca. 5%.

Core POP2 shows similar patterns in the sand fraction composition as core MW14-GC-106. The amplitude of fluctuations in components are low compared to the other cores. There are 2 greater maxima in terrigenous components at level 75 cm and between 71 cm to 68 cm. Also, a peak in molluscs percentages with 19 % is present at level 60 cm, although molluscs are generally underrepresented together with terrestrial biogenic components. Therefore, main components of the biogenic part are other biogenic, which are increasing towards the top section, benthic foraminifera and to a lower amount planktonic foraminifera. Terrestrial components are generally low and are mainly consisting of quartz, mica and aggregates. Aggregate percentages have a peak around the lower boundary of the tsunami layer. In this core the percentage of non-identified components is highest with percentages up to 10 %. Reason is the high amount of aggregates with both, terrigenous and biogenic constituents, which are classified as non-identified (**Table 6**).

3.4.1. Sand Composition in the Tsunami Layers

A similar trend at the onset of the tsunami layer can be seen in all cores with a relative increase of terrigenous material. Although, peaks of terrigenous components are present and even more pronounced in other layers in every core. In core M106 and POP2, a higher percentage of mollusc shells are present in the high energy event layer. Also, both latter cores show two peaks of biogenic components within the high energy event layers at 68 cm and 63 cm and 65 and 60 cm, respectively. The peak of biogenic components in core POP2 at 60 cm marks the upper boundary of the high energy event layer. In this peak, a maximum of molluscs is present with highest percentages throughout the studied core section of this core. Core M107 has one peak of biogenic components at 21 cm core depth. In core M106 and M107 is a small increase of terrigenous components towards the top of the high energy event layer. In core M107 this increase is mainly contributed by an increase in mica. A decline of mollusc shells highlights the end of the high energy event layers in the POP2 core at 60 cm but relatively higher number in mollusc shells are present till level 56 cm.

3.4.2. Principle Component Analysis of the Sand Composition

For each core a separate principle component analysis was conducted. In every PCA the solution of 4 components was chosen and, in every case, the total variance within these principle components explain > 75 % of the total variance in the data set (**Table 11**). Also, the samples of each core are classified in the 3 sections pre-tsunami, tsunami and post-tsunami.

Table 11: Scores (species score, weighted orthonormal) of the rotation matrix of the PCA. Red highlighted numbers are the main contributors for the respective principle component/ component assemblage. Grey principle component assemblages are selected for the PCA biplots. Expl. Var. = Explained total Variance; Planktonic Foram = planktonic foraminifera; Benthic Foram = benthic foraminifera.

	PC1_ 107	PC2_ 107	PC3_ 107	PC4_ 107	PC1_ 106	PC2_ 106	PC3_ 106	PC4_ 106	PC1_ POP	PC2_ POP	PC3_ POP	PC4_ POP
Expl. Var. [%]	29.0	20.9	13.6	13.6	43.3	21.3	8.2	7.7	39.0	20.0	11.2	8.2
Quartz	-0.324	0.432	-0.029	-0.309	0.041	-0.431	0.293	-0.135	-0.149	0.184	-0.505	0.041
Mica	-0.617	0.002	0.300	0.128	-0.261	-0.366	-0.017	0.644	-0.147	0.076	0.108	-0.010
Opaque	0.291	-0.199	-0.007	0.501	0.100	-0.203	0.162	-0.119	-0.114	-0.292	-0.498	0.622
Aggregate	0.091	0.204	-0.714	-0.070	-0.693	0.219	0.244	-0.189	-0.664	0.381	-0.029	-0.310
Other Terrestrial	0.145	0.466	-0.121	0.426	0.053	-0.355	0.053	-0.425	-0.220	0.139	0.204	0.451
Planktonic Foram	0.313	-0.097	-0.123	-0.560	0.500	0.340	0.160	-0.012	0.054	-0.480	0.249	-0.261
Benthic Foram	0.303	-0.170	0.100	0.044	0.397	0.020	0.238	0.373	-0.124	-0.453	0.014	-0.038
Mollusc	0.185	-0.650	-0.162	-0.123	0.089	-0.349	-0.750	-0.066	0.135	0.419	0.192	0.212
Terrigenous Biogenic	-0.298	-0.232	-0.460	0.341	0.147	-0.239	0.179	-0.397	-0.081	0.013	0.571	0.443
Other Biogenic	0.292	0.018	0.350	0.062	0.002	0.413	-0.387	-0.188	0.641	0.316	-0.128	-0.023

In core POP2 component assemblages PC1_POP and PC3_POP were selected and together they explain 50.2 % of the total variance. Main contributors of assemblage PC1_POP are molluscs and other biogenic component and of assemblage PC3_POP planktonic foraminifera and terrestrial biogenic components. For core M106 component assemblages PC1_106 and PC4_106 were selected, explaining 50 % of the total variance. The first assemblage is mostly correlated with the components planktonic and benthic foraminifera and the fourth with benthic foraminifera and mica. For core MW107 selected component assemblages are PC1_107 and PC2_107, explaining 49.9 % of the total variance. Components

with highest scores for the first assemblage are again planktonic and benthic foraminifera and for the second assemblage quartz and other terrigenous components.

3.4.2.1. Sand Composition PCA Results of Core POP2

The first component assemblages (PC1_POP) of core POP2 has negative loadings, except for level 72 cm till the middle of the tsunami layer, where a shift to positive loadings occurs till the end of the studied section at level 50 cm (**Figure 10**). This assemblage resembles biogenic components as mollusc, planktonic foraminifera and other biogenic components (**Table 11**). At the base of the tsunami layer, this assemblage is not present at all. The second assemblages consist of mainly aggregates and molluscs and is mostly underrepresented but exist throughout the whole studied section. However, in level 73 cm, level 63 - 62 cm (tsunami layer) and in 55 cm this assemblage is not present. A significant appearance is located at level 61 - 60 cm with relatively high loadings with values > 0.4. The third component assemblage (PC3_POP) is generally absent in pre and post tsunami layers but present in the tsunami layer. This assemblage consists of planktonic foraminifera and terrestrial biogenic components. A maximum of this assemblage with loadings > 0.4 exist in level 69 cm, which is the base of the tsunami layer. The fourth component assemblage starts to be present in the base of the tsunami layer, with one exception in level 63 cm, and then exists in alternation in the post event section.

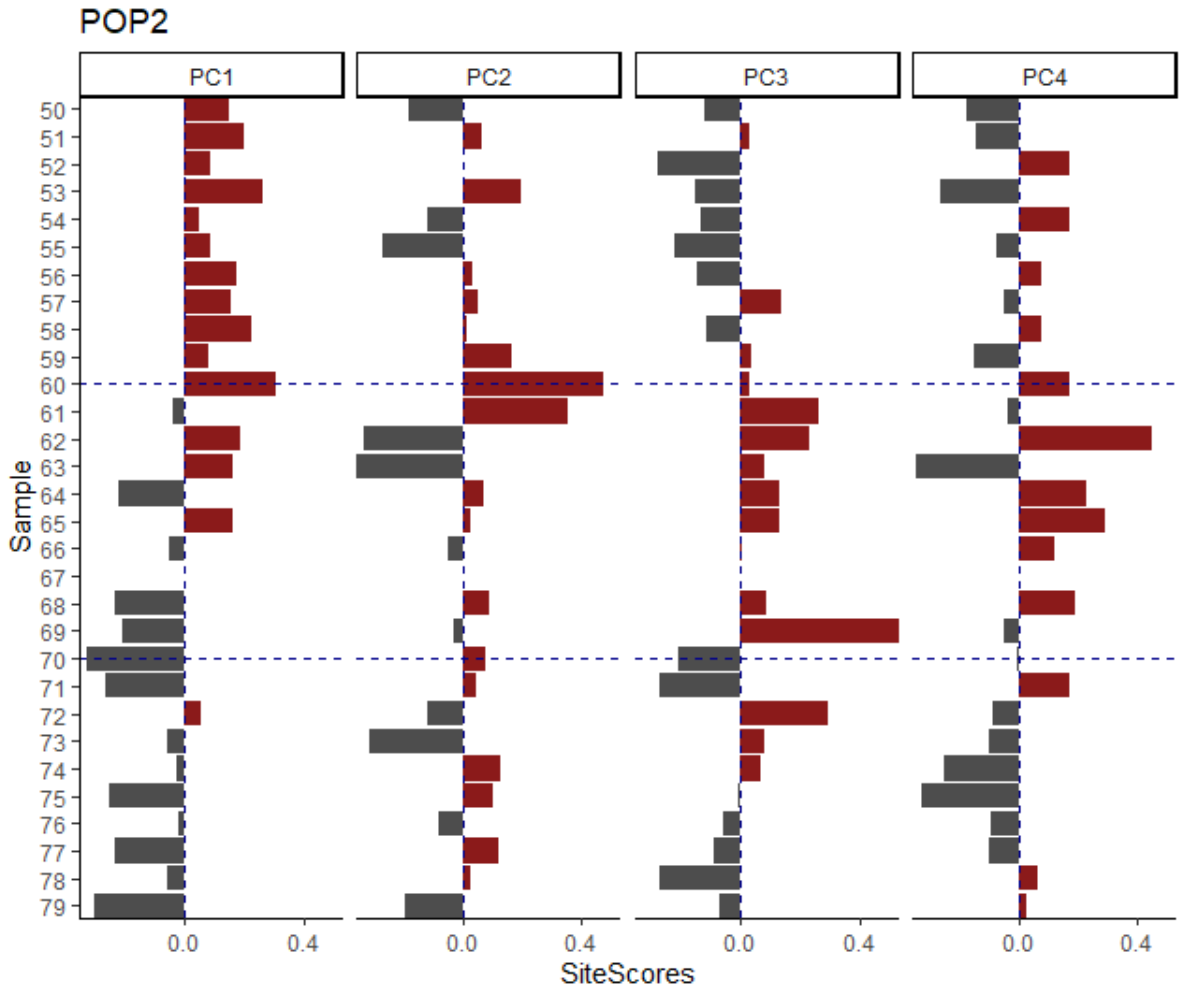

Figure 10: PCA loadings along core depths of core POP2. HEE = High Energy Event layer. Components with highest score for each principle component: PC1 = Mollusc and other biogenic, PC2 = Aggregate and mollusc, PC3 = Planktonic foraminifera and terrestrial biogenic, PC4 = Other terrigenous and terrigenous biogenic.

In the PCA biplot (**Figure 11**) the 3 sections show different spatial distributions along the axes PC1_POP and PC3_POP. Pre-tsunami samples are mainly clustered in the bottom left due to higher numbers of planktonic foraminifera and in a lower contribution of increases in other biogenic components. Tsunami samples are located at the top because of increased mollusc shells but also other biogenic component, aggregates, quartz, mica and other terrigenous contribute to this clustering of tsunami samples. Pre-tsunami samples are clustered in the bottom left controlled by opaque components and benthic foraminifera.

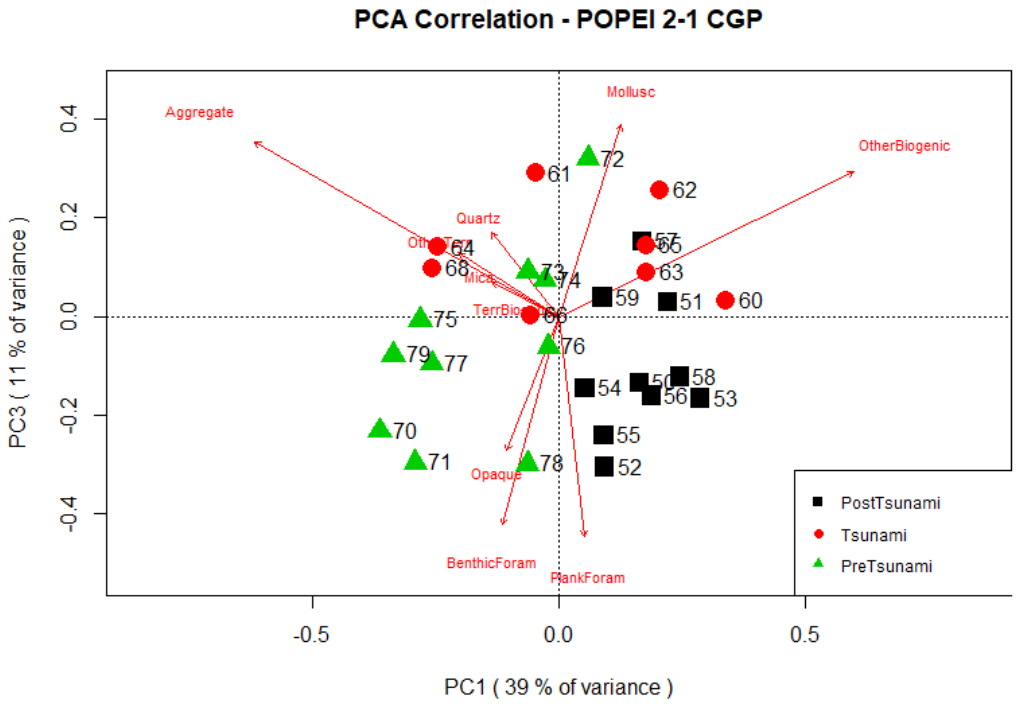

Figure 11: PCA biplot (scaling 1) of the sand components among the layers of the core POP2 using component assemblages PC1_POP and PC3_POP.

Also aggregates and planktonic components are contributors. In both, the pre and post tsunami section, 3 samples are also located in the top part and differ from the other samples of the respective sections. These are levels 74-72 cm in the pre tsunami layer and levels 59 cm, 57 cm, and 51 cm in the post tsunami layer. This implies, that tsunami samples contain a mixture of pre tsunami sands. Besides there are less foraminifera, distinguishing the tsunami layer from the sections below and above.

3.4.2.2. Sand Composition PCA Results of Core M106

The first component assemblage (PC1_106) of core M106 consists of planktonic and benthic foraminifera. The assemblage is predominantly absent in the pre tsunami layer and starts to be present in the tsunami layer until the end of the studied core section. Although, there are some short-term disappearances at level 68 cm, 61 cm and 53 cm (**Figure 12**). The second component assemblage (PC2_106) is generally present in the pre tsunami section and mostly absent in post and tsunami layer. Representative components of this assemblage are planktonic foraminifera and other biogenic components. There are two minor appearances at level 68 cm and 60 cm located directly after the tsunami layer. Another bigger appearance is present at level 58 - 57 cm. The third assemblage (PC3_106) is mostly alternating along the studied section. However continuing appearances are between level 77 – 70 cm and 57 – 56 cm without reaching

loadings of 0.4. The fourth component assemblage (PC4_106) is alternating in the pre tsunami layer, absent in the tsunami layer and appears almost continuous in the post tsunami layer. Main components of this assemblage are other terrigenous and terrestrial biogenic components.

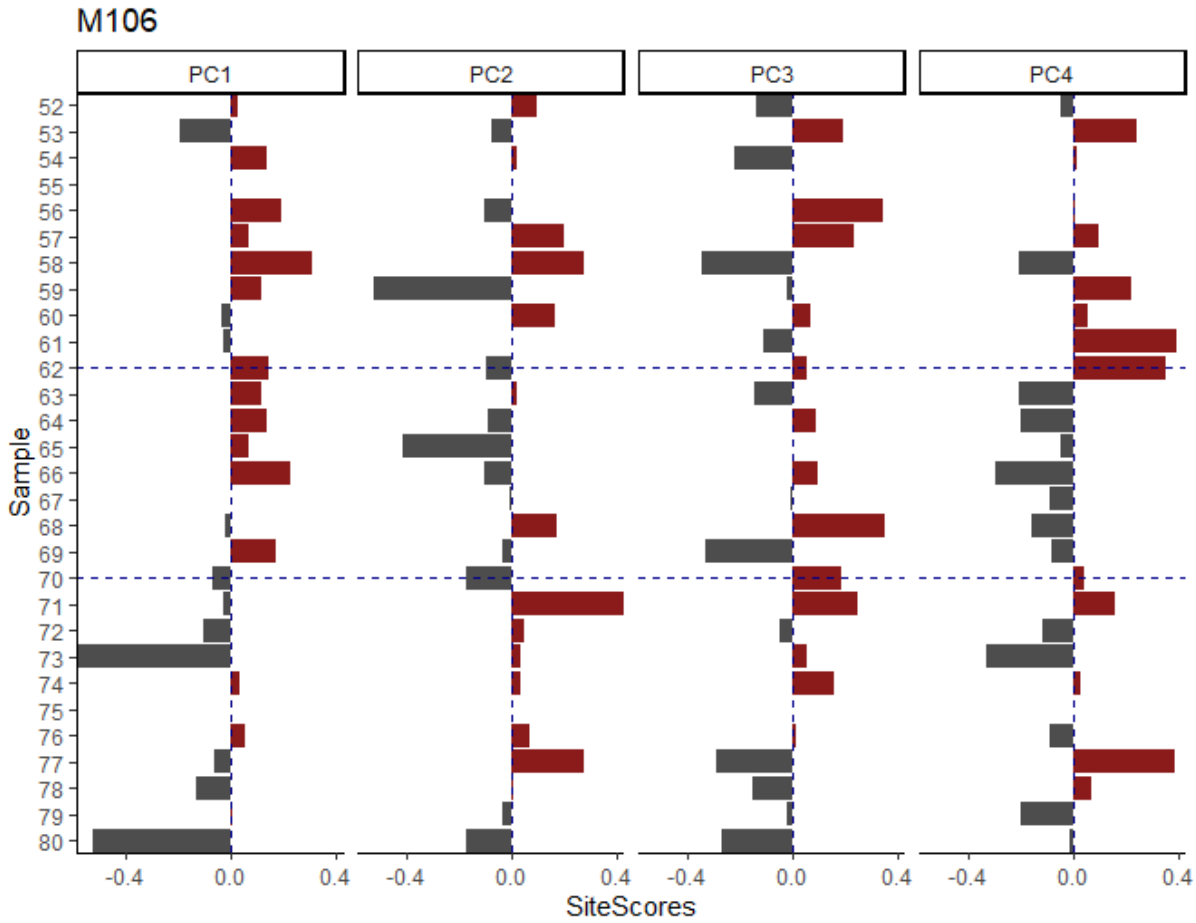

Figure 12: PCA-loadings along M106. HEE = High Energy Event layer. Components with highest score for each principle component: PC1 = Planktonic and benthic foraminifera, PC2 = Planktonic foraminifera and other biogenic, PC3 = Quartz and benthic foraminifera, PC4 = Mica and benthic foraminifera.

The spatial differentiation in the PCA-biplot of samples from core M106 (**Figure 13**) is similar to samples of core POP2. Pre-tsunami samples are spread in the left part of the biplot, except of level 76 cm and 74 cm. Responsible vectors are mica and aggregates. Tsunami samples are mostly located on the bottom right, only level 62 cm is located at top, because of higher numbers in benthic foraminifera and other biogenic components. Samples above the tsunami layer are mainly located to the centre, due to a very mixed composition of components. Only a spreading to the top right is present, because of planktonic foraminifera and other biogenic components. One possible outlier, level 58 cm, is located in between the tsunami sample cluster in the bottom left. Here, although a differentiation of sand composition can be

seen in all 3 groups, it seems that the composition of the tsunami sand contains material of the pre tsunami layer.

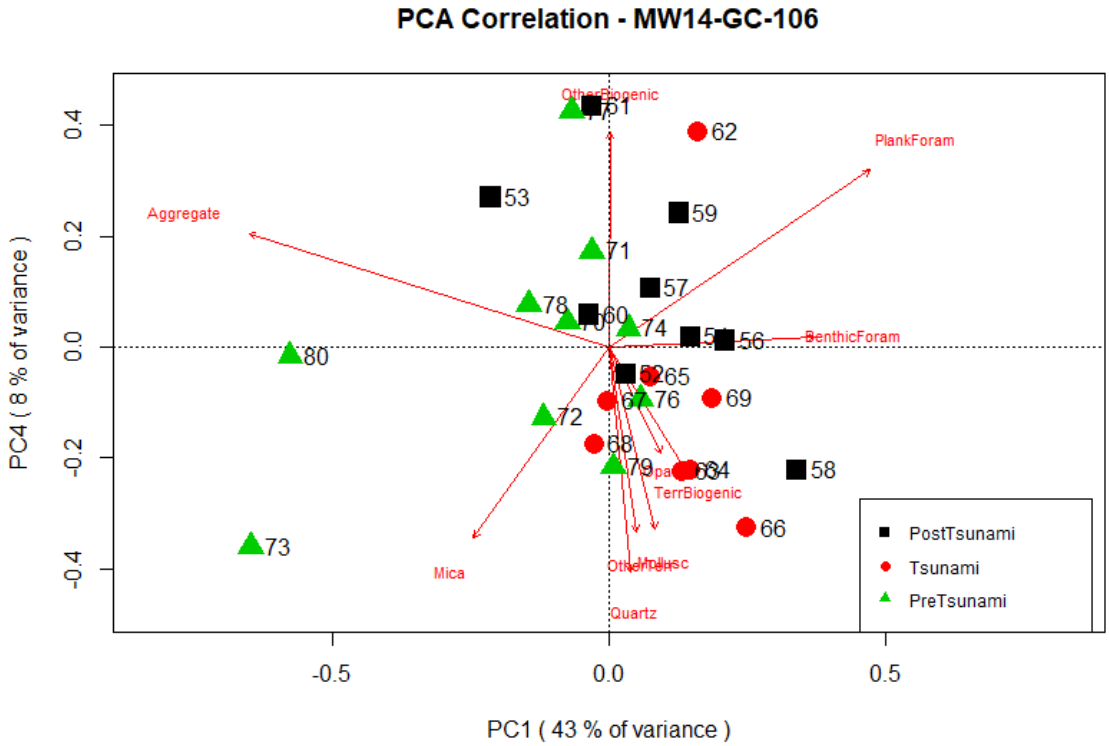

Figure 13: PCA biplot (scaling 1) of the sand components among the layers of the core M106.

3.4.2.3. Sand Composition PCA Results of Core M107

First component assemblage (PC1_107) of core M107 is alternating in the pre tsunami layer, absent in the tsunami layer and shows a strong presence, except of level 12 cm, with loadings up to 0.6 in the post tsunami section (**Figure 14**). Strong members of this assemblage are planktonic and benthic foraminifera. The second assemblage (PC2_107) is alternating throughout the whole studied section but has a pronounced presence in the post tsunami section, although there are also 2 levels, at 15 cm and 12 cm, where the assemblage is absent. Main components of this assemblage are quartz and other terrigenous components. Important components of the third assemblage (PC3_107) are mica and other biogenic components. The assemblage is present throughout the pre tsunami layer, mostly absent in the tsunami layer and afterwards till level 15 cm in the post tsunami layer. From 15 cm on, in the post event layer, it is alternating with small negative and positive loadings till the end of this section. Fourth assemblage consist mainly of opaques and other biogenic components. This assemblage appears especially in the tsunami layer and in levels before, starting at level 25 cm. In the other

part of the pre tsunami layer it is absent. After the tsunami layer this assemblage is alternating with lower loadings.

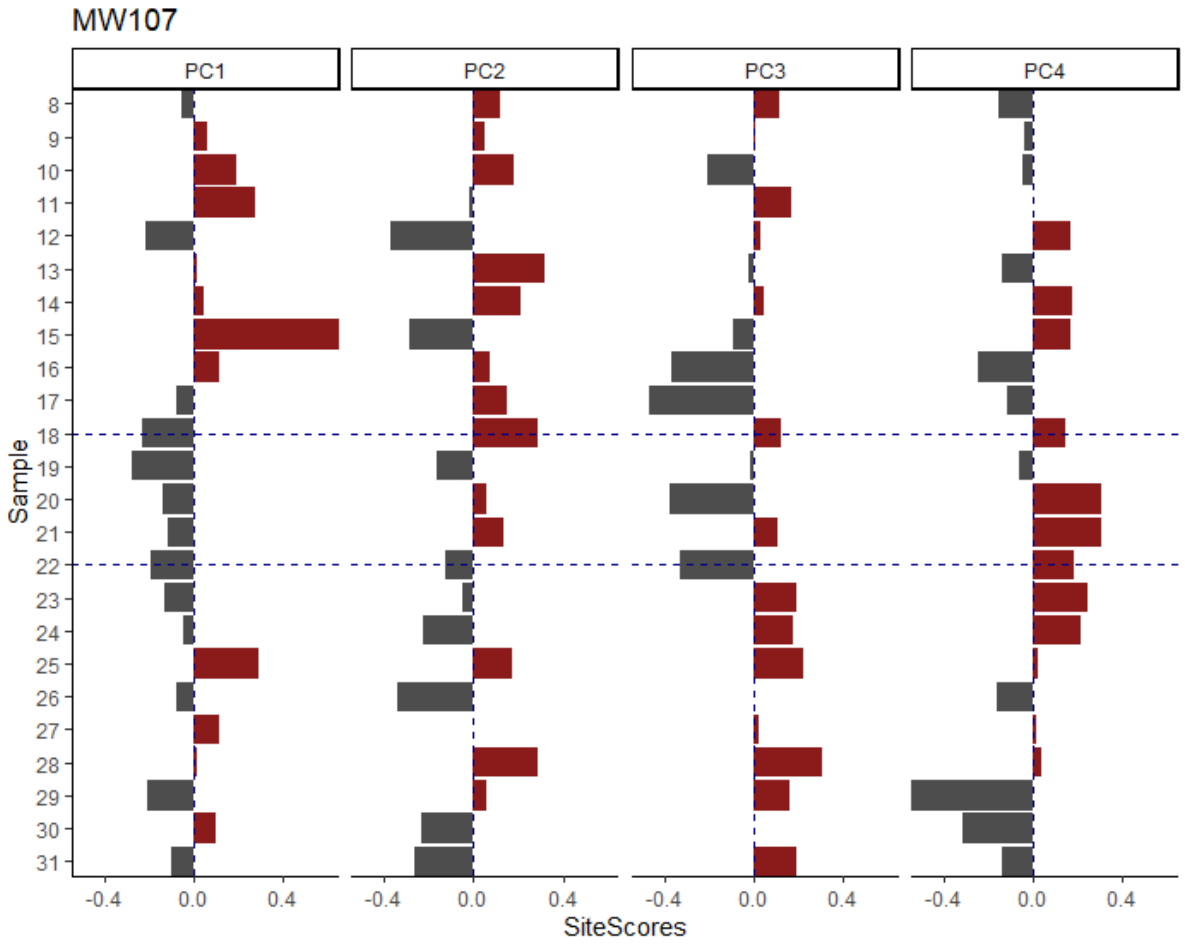

Figure 14: PCA-loadings along M107. Components with highest score for each principle component: PC1 = Planktonic and benthic Foraminifera, PC2 = Quartz and other terrigenous, PC3 = Mica and other biogenic, PC4 = Opaque and other terrigenous. Red means positively related and grey negatively. Tsunami layer is in between the two blue dashed lines.

The PCA biplot of core M107 shows again a clear spatial differentiation between the 3 distinct sections (**Figure 15**). Pre tsunami samples are located at the bottom left controlled by higher numbers of terrestrial biogenic components and molluscs. Possible outliers are level 28 cm and 25 cm, which are located in between the post tsunami samples at the top right due to higher abundance of aggregates and other terrigenous components. Post tsunami sample are clustered at the top right because of higher numbers in aggregates, other biogenic and other terrigenous components. Here, possible outliers of this sample group are level 15 cm and level 12 cm. The first outlier is located at the bottom right due to higher numbers of benthic and planktonic foraminifera. Latter outlier is located at the bottom right within the group of pre tsunami samples. Tsunami samples are located at the top left, except of level 19 cm, which is also located at the left but shifted to the pre tsunami group. Increased numbers of quartz, mica

and to a lower amount terrestrial biogenic component cluster the tsunami samples differentially to the pre and post tsunami samples. Concluding remarks match core POP2, because here tsunami samples also have clear differentiation, but a mixture with pre tsunami can be seen.

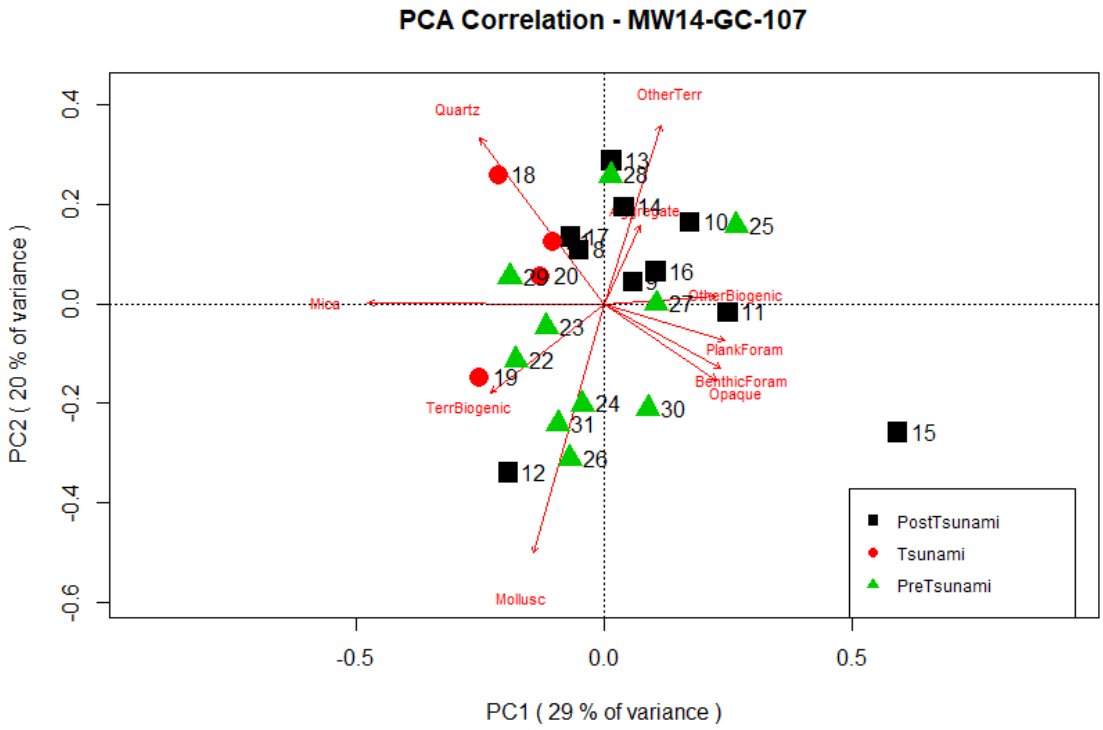

Figure 15: PCA biplot (scaling 1) of the sand components among the layers of the core M107.

3.5. Microtextural Surface Occupation of Quartz Grains

A total of 90 scanning eclectron microscope images of quartz grains were analysed of their microtextural surface occupation. The created R-script and the data is provided in **Annex E** und **Annex F**. In general, samples show minor differences (**Figure 17**) and display predominantly dissolution and in some cases on the whole grain surfaces. Second most abundant microtextural feature are fresh surfaces. Adering particles and percussion marks occupy minor percentages of the grain surface. However, tsunami grains are ,compared to both non-tsunami samples, characterized by a larger number of fresh surfaces. This is supported by a p-value of 0.044 and different medians. But the upper limit of fresh surfaces is similar in all samples with 75 %, while the lower limit is at least 10 % in tsunami samples and in both other samples 0 % is possible. The mean value of dissolution is smaller in tsunami samples, but medians are not distinct and the p-value is not significant (p = 0.1761) between the 3 samples. Althought, tsunami and post-tsunami samples can have grains that cover only 10 % of grain

surfaces with dissolution, while pre-tsunami samples always show high dissoltuion percentages of ca. 50 – 60 %. Tsunami sample show a slightly higher mean value of percussion marks compared to pre- and post-tsunami samples, but again medians are not distinct and the p-value of 0.2474 is not significant. Medians and means are around 1 (0 – 10 %). Here, pre-tsunami and tsunami sample have a higher upper limit with 50 % of the grain surface than the post-tsunami sample with maximal 25 %. Adhering particles are similar in all samples with mean and medians around 1 (0 -10% of grain surface). Mean values of angularity is lowest (more rounded) in the pre-tsunami sample and highest (more angular) in the post-tsunami sample, showing that generally grains are rounder the deeper the core depth of the sample. However, only the post-tsunami sample shows a different median with 3 (sub-angular) compared to 2 (sub-rounded) of both other samples.

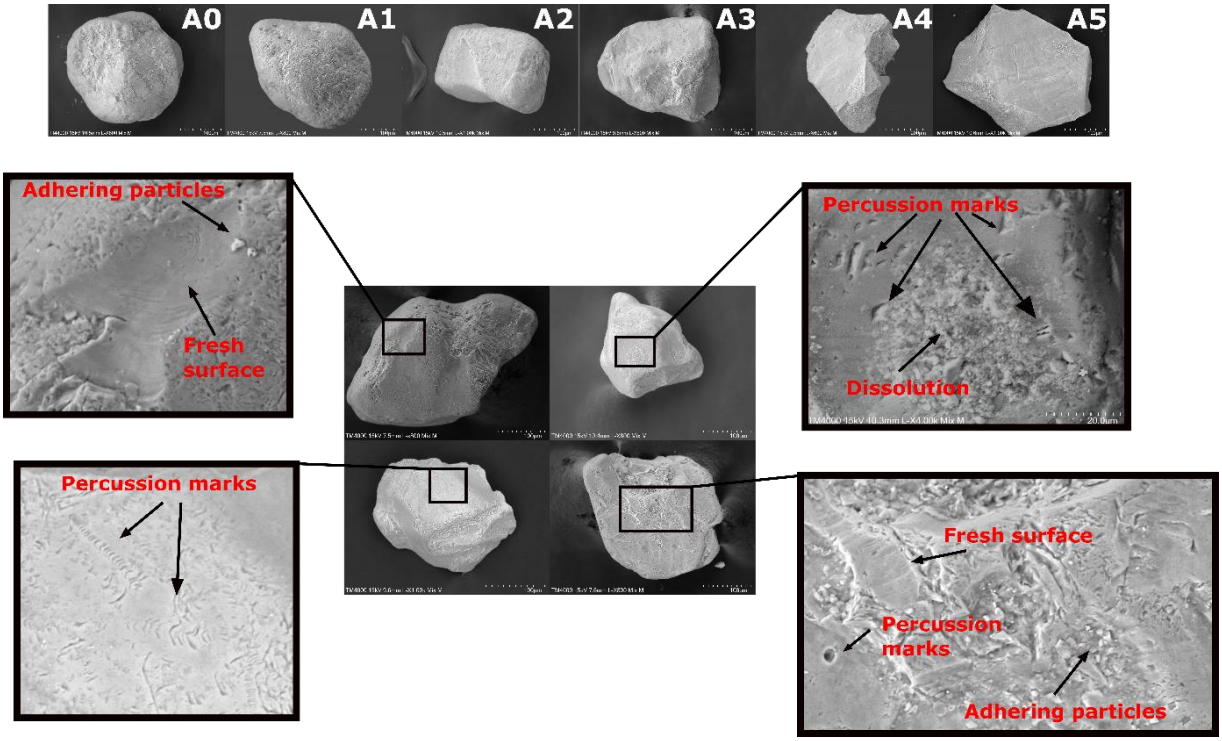

Figure 16: Examples for the studied microtextural features. On top angularity examples from (A0 (very rounded) to A5 (very angular).

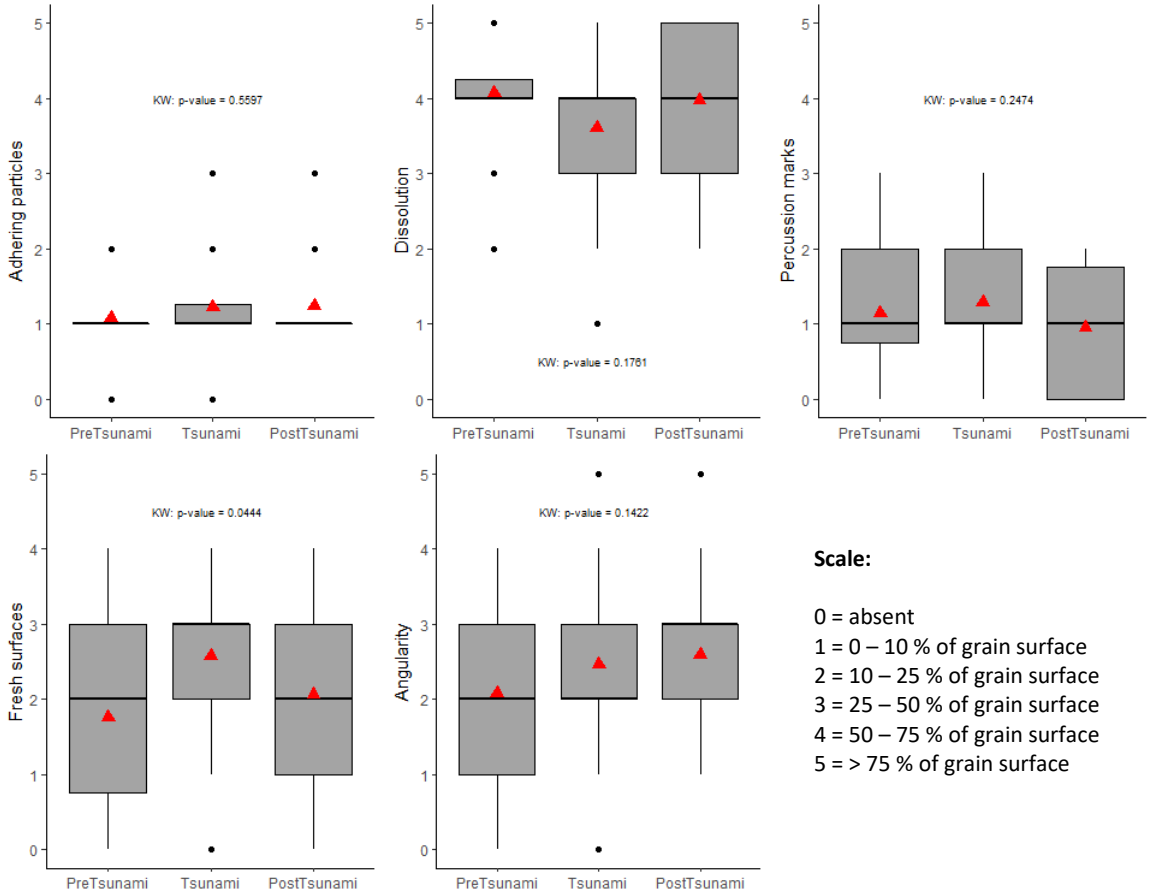

Figure 17: Boxplots of each microtextural family and p-values of Kruskal-Wallise test (Kruskal and Wallis, 1952). Black points represent outliers and red triangles indicate mean values. Note that angularity is scaled different (see chapter 2.3.4).

3.6. Numerical Modelling

The simulated 1755 Lisbon alike earthquakes generated tsunami waves leading to a significant perturbation of the sea surface (**Figure 18** and **Figure 19**). The resulting initial tsunami wave has a height of around 5 – 6 m and a wavelength about 120 km triggered by the simulated earthquakes. Wave heights are high close to the coast. However, maximal wave heights (~ 13 m) in the study are westward of Quarteira and high between Faro and Quarteira (~ 8 m), compared to east of Faro (~ 4 m).

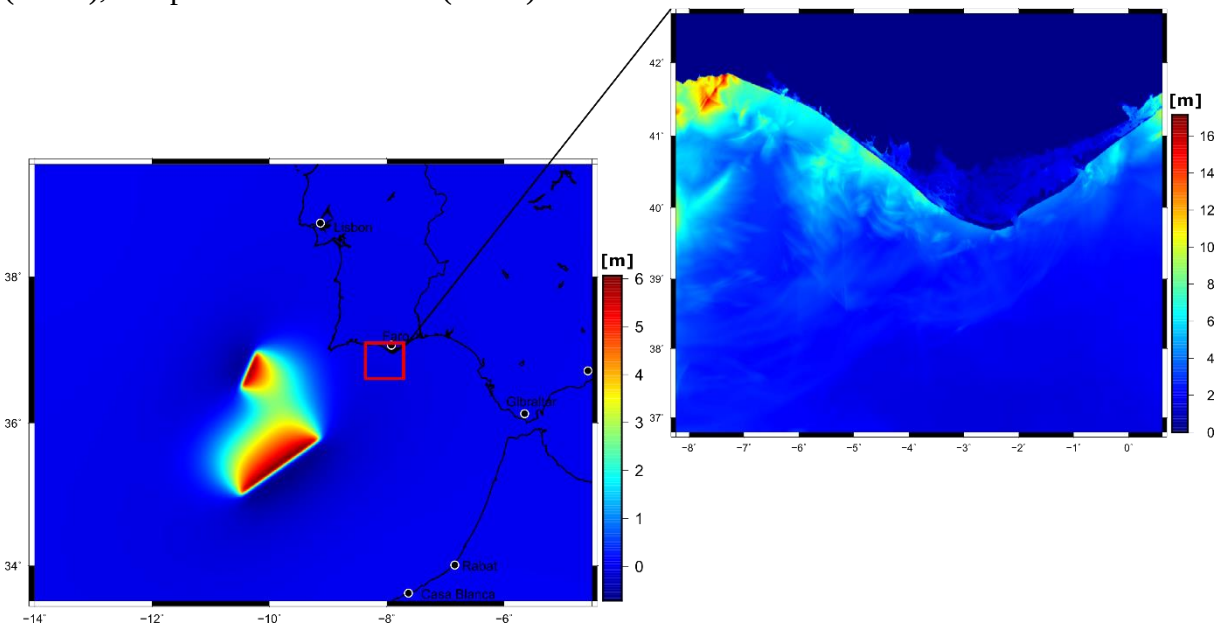

Figure 18: Initial conditions (wave height) of the tsunami wave generated by the earthquakes (left) and maximum sea surface elevation in the study area (right).

Horizontal velocities on the surface (U_{sur}) are generally higher at the core location of M107 compared to the other 2 core locations and values are > 0.2 m/s throughout the tsunami event for all core locations. Maximal values are between 25 – 50 min and 85 – 105 min after the earthquake. However, horizontal velocities displayed in **Figure 20** need to be interpreted with caution. In most cases $U_{sur} \neq U_{bottom}$ (horizontal bottom velocities), because this applies only when water depth is smaller than 1/20 of the wavelength.

By reducing the noise of the sea surface elevation data, 3 pronounced tsunami waves can be detected propagating through all 3 core locations. Thus, at the core locations 3 propagation phases were detected within 150 mins after the earthquake. Characteristics of the 3 landward propagating tsunami waves at core locations and corresponding bottom velocities calculated with equation (2) are listed in **Table 12**.

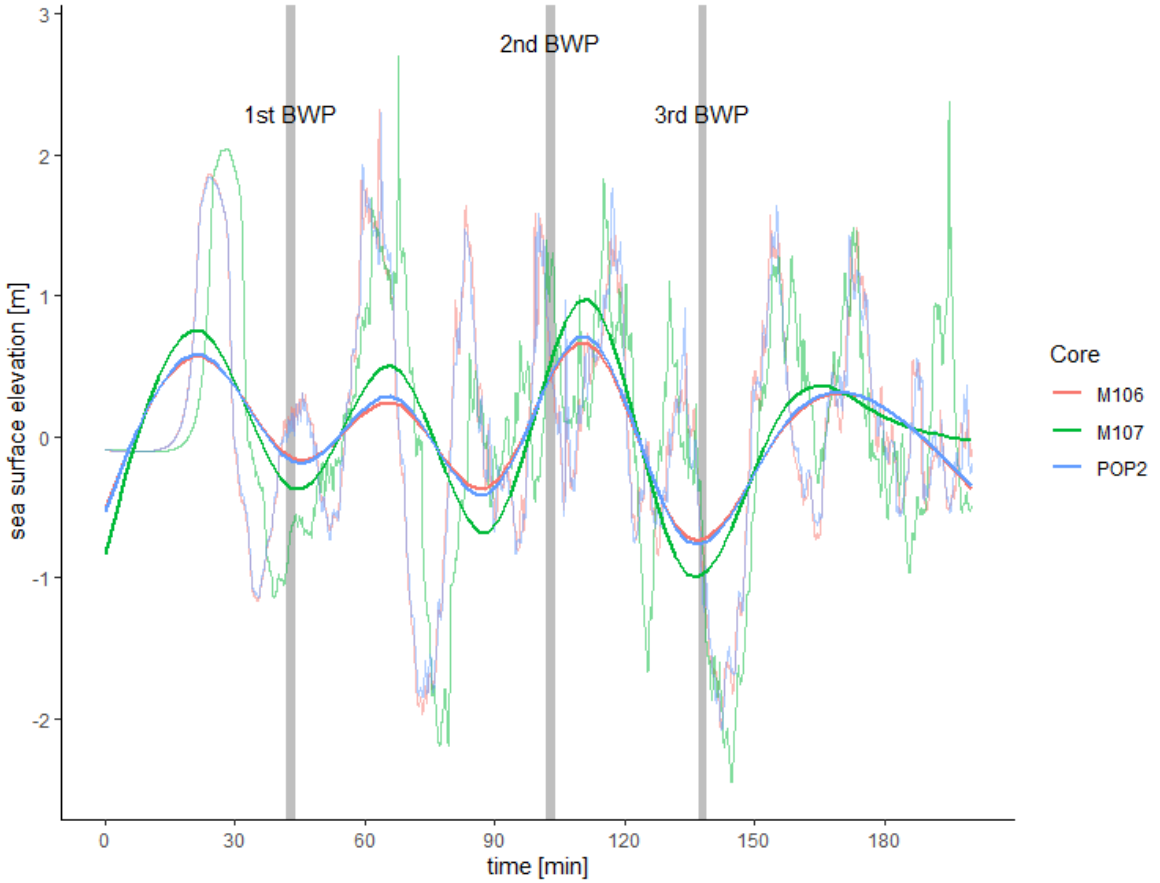

Figure 19: Sea surface elevation at the 3 core locations during the simulated 1755 tsunami event. At time=0 the earthquake occurred. Strong coloured lines are smoothed (see chapter 2.4), while brighter colours represent the raw model output data. Grey lines indicate the times of the backwash phases represented by the vector field maps in **Figure 21**. BWP = backwash phase.

Table 12: Modelled tsunami wave characteristic. The wavelengths were calculated using $L = T\sqrt{g\,d}$ with g=9.81 and d = mean core depths (**Table 2**). Bottom velocities were calculated using the mean value of the respective amplitude ranges (max. and mean values) by applying equation (2). AEQ = after earthquake.

Wave Parameter	1st Tsunami Wave 22 min AEQ	2nd Tsunami Wave 65 min AEQ	3rd Tsunami Wave 118 min AEQ
Max Amplitude (Mean) [m]	1.8 – 2 (0.5 – 0.75)	2.3 – 2.6 (0.25 – 0.5)	1.5 – 1.8 (0.65 – 1)
Period [s]	2700	2700	3300
Wavelength [m]	74378	74378	90907
Max Bottom velocity (Mean) [m/s]	0.68 (0.22)	0.87 (0.13)	0.59 (0.29)

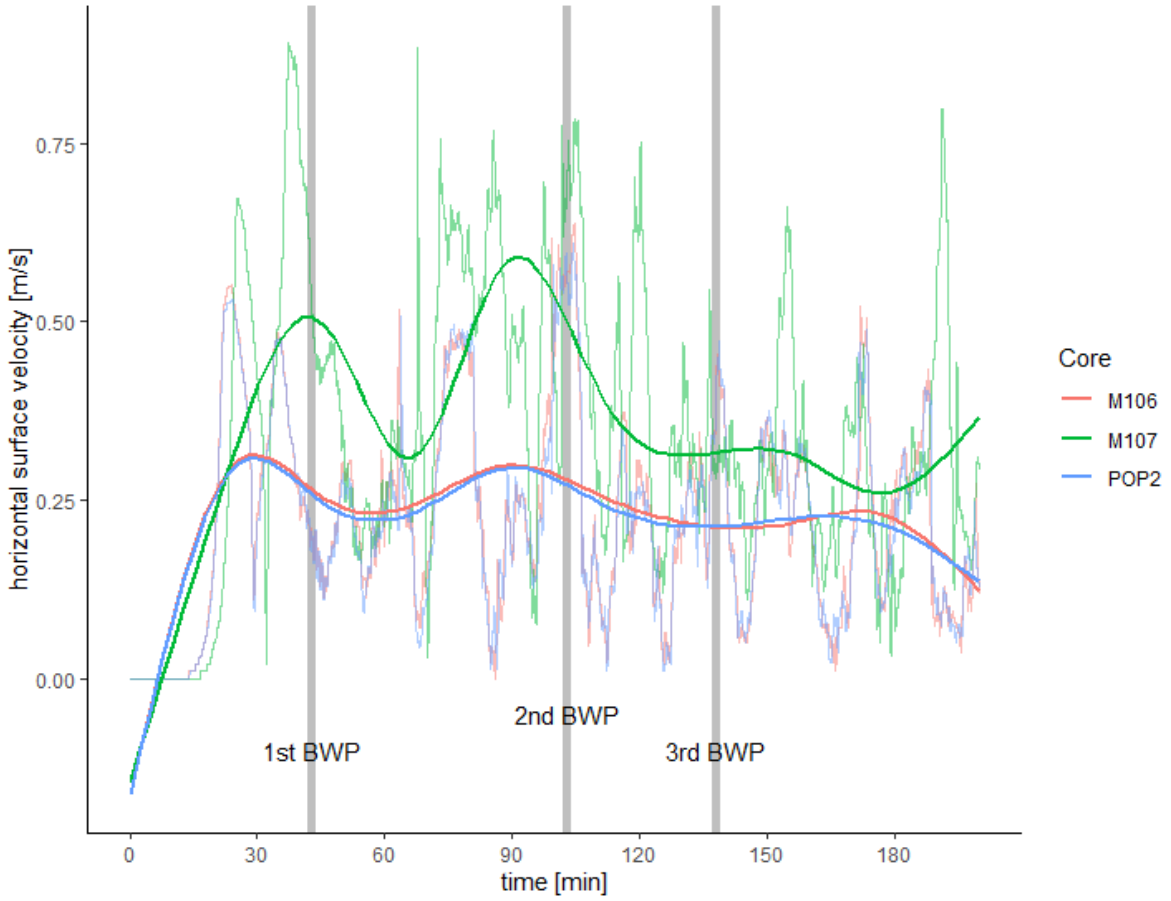

Figure 20: Horizontal velocity of water particles at the surface during the simulated 1755 tsunami event. Time starts with the earthquake. Strong coloured lines are smoothed (see chapter 2.4), while brighter colours represent the raw model output data. Grey lines indicate the times of the backwash vector field maps in Figure 22. BWP = backwash phase.

To elaborate backwash phases of the event, velocity vector maps of each minute after the earthquake were analysed and times having most of the vectors aligned to the south were chosen, indicating offshore flowing traction currents. Thereby, backwash phases of the 1755 tsunami are detected after the first, second and third tsunami wave, at minutes 43, 104 and 138, respectively (**Figure 21**). The first and second backwash phases coincide with high values of horizontal surface velocities > 0.5 m/s at core locations and are therefore more distinctive as the third backwash phase with velocities of ~ 0.3 m/s. Vector field maps indicate, that backwash currents are strongest close to the coast, decrease when flowing offshore and almost disappear when reaching the outer edge of the continental shelf. Large scale flow patterns show similar behaviour in the 3 backwash phases. A rip current can be seen in all 3 vector field maps starting between Faro and Quarteira and flowing offshore in south-west direction. Thus, flow directions are south-east at the core location of POP2 and south at core locations of M106 and M107. Possible provenance of backwash sediments contributing to the tsunami deposit at all 3 core locations might be the coastal area between Faro and Quarteira.

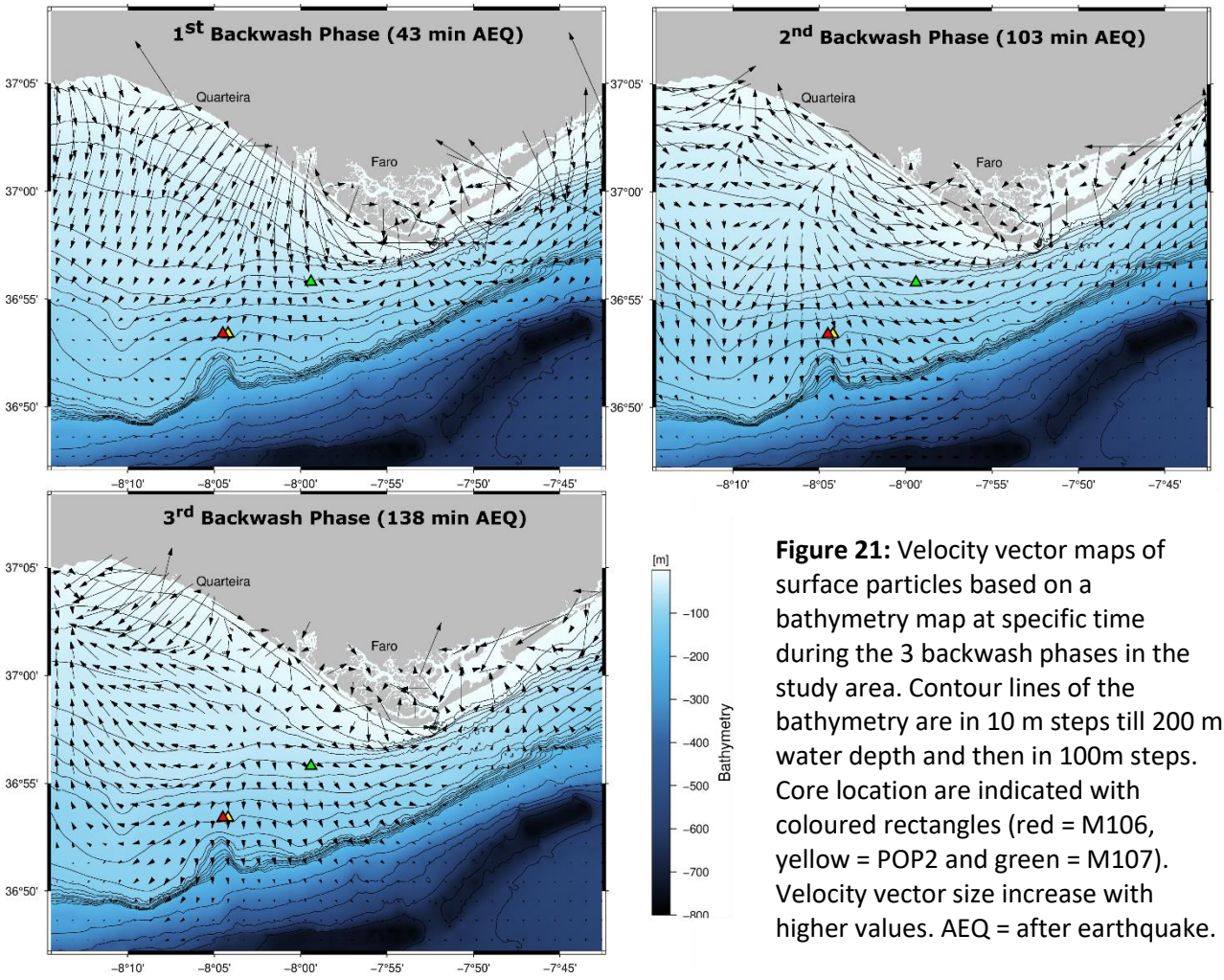

Figure 21: Velocity vector maps of surface particles based on a bathymetry map at specific time during the 3 backwash phases in the study area. Contour lines of the bathymetry are in 10 m steps till 200 m water depth and then in 100m steps. Core location are indicated with coloured rectangles (red = M106, yellow = POP2 and green = M107). Velocity vector size increase with higher values. AEQ = after earthquake.

4. Discussion

4.1. Conformity of Tsunami Layers with the 1755 Tsunami Event

In the case of the present study, it is crucial to have a confident accordance of the tsunami layers with the age of the 1755 Lisbon tsunami event. Results of the established age-depth relations of tsunami layers in core M106 and M107 meet this requirement (**Figure 4** and **Figure 5**), but the tsunami layer of core POP2 is lacking accordance (**Figure 3**). However, close to the location of core POP2, Quintela et al. (2016) studied and discussed the tsunamigenic imprint of the 1755 Lisbon tsunami event in another core (VC2B). They extended the possible tsunami layer to lower core depths, because of a proportional increase in coastal foraminifera group starting at level 34 cm persistent until level 81 cm. Also, their age-depth relation results constrain this section to be younger than 800 years. In combination of this micropaleontological tsunamic signature and age-estimations they relate this core section to the 1755 event. Veiga-Pires and Mestre (2009) showed that a unique sedimentary record of cores with almost similar locations (here called "twin cores", with a distance of 0.05 – 0.2 m between them in a transitional region) cannot be assumed. Locations of core VC2B (36.8869447°, -8.0661072°) and core POP2 (36.88595767°, -8.061872°) are ~ 400 m apart. However, the continental shelf is a less dynamic sedimentary system compared to transitional regions and similar core characteristics seems to be more likely, even if distances between "twin cores" are 20 times greater. Thus, setting the upper limit of the tsunami layer related to the 1755 tsunami in core POP2 to a lower core depth seems reasonable. The age models are based on less than 7 given ^{14}C-ages for each core and ^{210}Pb age-estimations in the topmost sections of the core (max. 24.5 cm core depth). Also 8 out of 15 ^{14}C-dating samples in the 3 cores are taken from layers of possible reworked material by tsunami wave action, which can lead to wrong age estimations (Fowler et al., 1986). In the age-model function of 'rbacon' outliers are addressed by considering a student-t distribution instead of assuming an error of the radiocarbon age (σj) (Andrés Christen and Pérez E, 2009), minimizing the effect of outliers (Blaauw and Christen, 2011). Therefore, by using Bayesian age-depth models, most realistic precision and robustness, compensating the low dated levels, can be expected compared to classical methods as linear interpolation (Blaauw et al., 2018).

Storm and tsunami events can leave similar deposits and their discrimination is still problematic (e.g. Nanayama et al., 2003; Morton et al., 2007; Sakuna-Schwartz et al., 2015).

Offshore transport induced by storm events is mostly restricted to the inner shelf (e.g. Ogston et al., 2000), compared to tsunami induced backwash currents. Storm wave erosion of seafloor sediments and possible 1755 tsunami layers needs to be considered, especially regarding the lower accumulation rates in the core locations. When the wave base is the same as the water depth, erosion of sediments is possible. After Weiss and Bahlburg (2006) the water depth (d) where a storm wave affects the bottom sediments (d_b) is:

$$d_b = \frac{\pi g A^2}{25}$$

where g is the gravitational acceleration ($g \approx 9.81$ m/s^2), A the amplitude of wave (A = wave height (H) / 2) and assuming exactly the boundary between deep- (0.5 x wavelength (L) < d) and intermediate-water (0.5L > d < 0.05L). The lowest water depth for the studied cores is ~57 m of core M107. Thus, by assuming d_b = 57 m, the amplitude of the storm wave needs to be > 6.8 m (H = 13.8 m) to be capable of reworking the tsunami sediments. In 1941 CE a storm event occurred in Portugal, which is the biggest storm event of the 20th century hitting the Iberian Peninsula (Freitas and Dias, 2013). Wave data are unavailable for this event, but highest modelled wave heights for the studied area are 13-14 m with periods of 14 s (Fortunato et al., 2017). Considering the southwest direction of the storm, similar wave heights could have reached the present study area, but erosion of the tsunami layers in water depths > 57 m seem still unlikely.

Fluvial floods are other possible events leading to a terrestrial input to the offshore areas. As tsunami backwash flows, flash floods can generate hyperpycnal flows because of their high suspension load. However, there are different sedimentological characteristics between tsunami and flood deposits. Flood deposits show generally better sorting and are composed of less coarser material than tsunami backwash deposits, because of the higher energy involved in tsunami backwash events (Sakuna-Schwartz et al., 2015). Regarding the lower energy in flood events, their sedimentary/hydrodynamic equilibrium is reached in closer proximity to the coast and it is therefore unlikely to have a depositional signature in the outer shelf. Despite this, in the Algarve region, no extreme fluvial flood is reported in the study area, although maximal historical peak discharges of ~ 11,000 m^{3}s^{-1} in 1876 and 1603 are reported for the next biggest river close to the study area, the Guadiana River (Ortega and Garzón, 2009).

4.2. Tsunamigenic Sedimentological Signatures in the Outer Shelf

In all tsunami layers of the different cores a sedimentological signature for high energy events are present as a variation in grain size distribution (usually mean grain size), X-ray fluorescence (XRF) and magnetic parameters suggesting a high energy sedimentation regime in the tsunami/event layers (Drago et al., 2016).

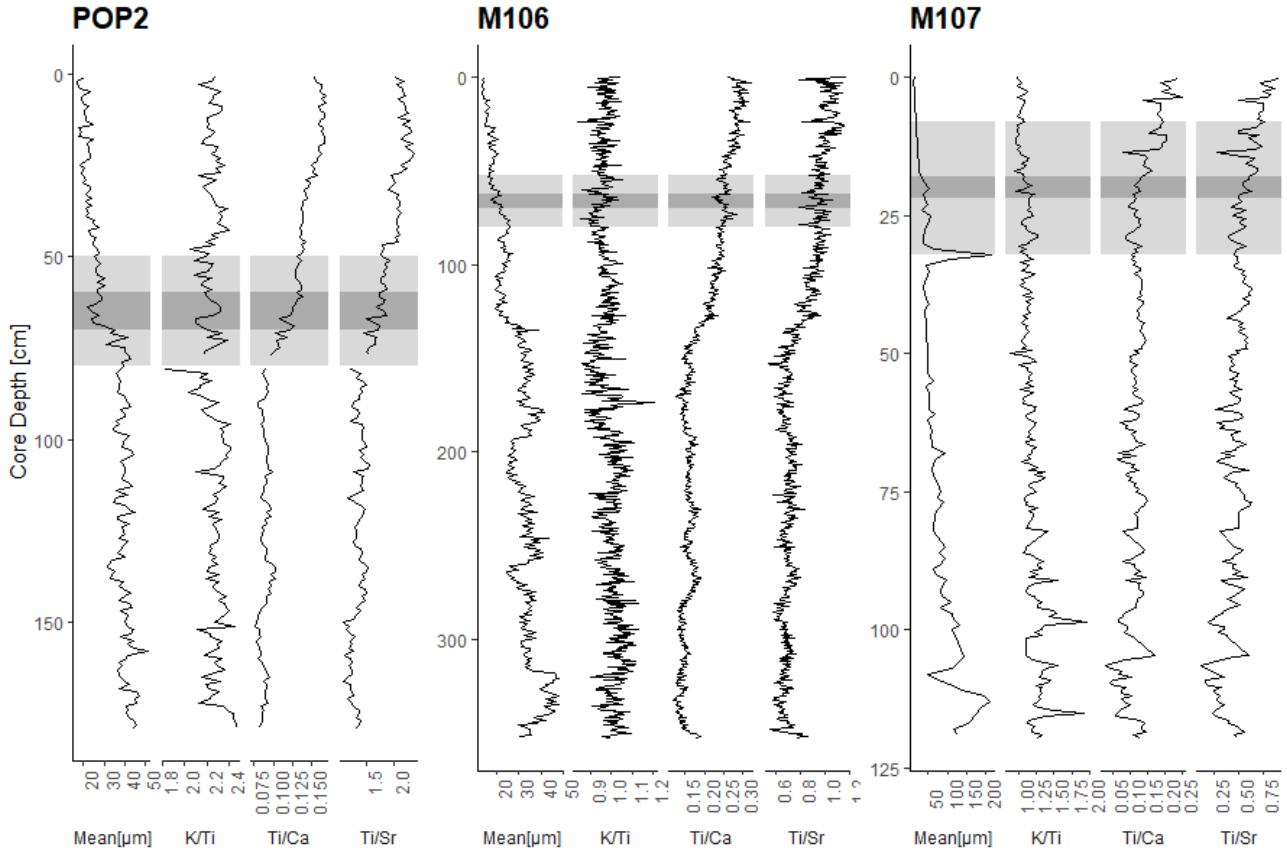

Figure 22: Mean grain size and selected X-ray fluorescence ratios of the 3 cores along core depths. For core M106 and POP2 grain size distribution is purely based on laser diffraction in volume percentage (< 0.001µm – 2mm). In core M107 the fraction < 500 µm was analysed by laser diffraction and > 500 µm by traditional sieving to make the analysis more representative and reliable, because of the general coarser grain-size (Drago et al. 2016). Light grey area indicates the entire studied core sections and darker grey represents the tsunami layers. Note the differences in scales.

Differences between the sedimentary signatures in core M106 and POP2 compared to M107 can be expected because of their different location. Also, accumulation rates play an important role in preservation of tsunami layers. Reworking of seafloor surface sediments by bioturbation is intensified in areas with lower accumulation rates and can alter tsunami layers (Wheatcroft and Drake, 2003). Moreover, studies in Khao Lak (Indonesia) show, that remaining offshore tsunami deposits have been mostly found in sheltered areas with higher accumulation rates (Feldens et al., 2012; Milker et al., 2013). The average accumulation rate of core M107

(0.021 cm/year) is more than 3 times lower than of core M106 (0.21 cm/year) and core POP2 (0.077 cm/year). This suggest a better preservation of tsunami layers in core M106 and POP2 compared to M017.

4.2.1. Mean Grain Size

Along the core depths of each core, there are several pronounced maxima and minima in mean grain size (**Figure 22**) showing that the imprint of tsunami events is not decisive as outlined in chapter 1.4.1..Yet, mean grain size is generally higher in core M107 compared to the other two cores, demonstrating the importance of local geomorphology as bathymetry and sediment sources. The peak in mean grain size of the sand fraction in core M107 coincides with the general mean grain size distribution (**Figure 22**). The other cores show no variation in the mean grain size in the sand fraction of the studied section (**Figure 8**), whereas mean grain size of the total sample show in both cases a decreasing trend in the tsunami layer (**Figure 22**). A same pattern in tsunami deposits was found in southeastern Hokkaido after the 2003 Tokachi-oki tsunami, with finer material in deeper areas and coarser in shallower areas (Noda et al., 2007). It is already known that offshore transport of coarser sand is of limited extent (Tamura et al., 2015). Hence, having no mean grain-size variations in the sand fraction of the two finer cores M106 and POP2 can be explained by the lower energy regime in those water depths (> 84 m). This is also supported by the higher modelled horizontal velocities at the location of core M107 compared to locations of core M106 and POP2 during the entire event (**Figure 20**).

4.2.2. Sand Composition

Tsunami sediments in the studied cores show only small variation in terms of sand composition compared to pre and post tsunami sediments and no remarkable terrigenous signal is present. However, in core POP2 and M107 there is a slight increase of other terrigenous minerals (quartz, mica and opaques are excluded) in the tsunami layer visualized by PCA-generated component assemblages (PC4_POP and PC4_107). More evident is the relative increase in mollusc shell abundance in core M106 and POP2 (**Figure 9**, **Figure 11** and **Figure 13**). Also, two anomalous peaks of mean grain size, at level 59 cm and 69 respectively for core M106 and POP2, induced by mollusc shells (> 2000 µm) indicate a higher abundance in tsunami layers of the latter 2 cores. In cores originating from similar water depths southwest of the Tagus estuary (Portuguese west coast) possible 1755 tsunami layer is also enhanced in shell fragments (Abrantes et al., 2008). They interpreted this peak of shell fragments as an indication

for reworked material. On the other hand, offshore Khao Lak (Indonesia) shell fragments deposited in tsunami sediments were interpreted as a result of backwash flows (Feldens et al., 2008). In the case of the present study shell fragments do not increase the mean grain size (except of the two peaks) in those layers. Shell fragments often show a more planar shape and thus increasing their buoyancy. To reach their hydrodynamic/sedimentary equilibrium, an increased transported distance to offshore areas is needed. A similar behaviour was proposed for mica, suggesting a higher abundance of those components in upper onshore tsunami deposit sections (Jagodziński et al., 2012). In core M107 this increase of mica in the upper section of the tsunami layer can be observed, which is subsequently decreasing again (**Figure 9** and **Figure 15**). In the two other cores a trend in mica cannot be distinguished, probably due to the general higher amount of fine material including more phyllosilicates. This could indicate again another sedimentary regime between the two different core locations. Consequently, it is more likely that backwash flow transport small shell fragments to the offshore areas, originating from shallower coastal areas.

A differentiation between pre, post and tsunami samples is present in all 3 cores, although an admixture of few pre and post tsunami samples in the tsunami layer can also be observed (**Figure 11**, **Figure 13** and **Figure 15**). This indicates a heterogenous composition of the tsunami layer induced by reworking through the successive tsunami waves and following backwash phases. This heterogeneity in tsunami sediments was also detected in onshore tsunami deposits of the same 1755 event at Boca do Rio by diffuse reflectance spectrophotometry in the siliciclastic fraction (Font et al., 2013). In offshore tsunami deposits a mixing characteristic of pre event sediments in the tsunami sediments were also apparent, ascribed to successive wave uprush and backwash phases. (Feldens et al., 2012; Milker et al., 2013; Toyofuku et al., 2014).

4.2.3. X-ray Fluorescence – Terrigenous Material Tracer

To aid the mentioned sedimentological proxies X-ray fluorescence (XRF) data is widely used in tsunami sediments studies (Sakuna et al., 2012; Sakuna-Schwartz et al., 2015; Chagué-Goff et al., 2017; Tyuleneva et al., 2018; Smedile et al., 2019). The Ti/Ca (Titanium/ Calcium) and Ti/Sr (Titanium/ Strontium) – ratio are used as an indicator of terrestrial material because Ti is originating mainly from continental rocks as volcanics, schists and gneiss. In contrast Ca and Sr are tracers for marine sediments because of their abundance in carbonates (e.g. Chagué-Goff et al., 2017). Having an increase in the ratios of Ti/Ca and Ti/Sr is therefore reflecting a

terrigenous input. Based on the same principle, another used tracer of detrital material is the ratio of Potassium/ Titanium (K/Ti) (e.g. Gràcia et al., 2010).

As for the sand composition percentages, the specific element ratio signatures show no distinct short-term variation in the studied section, thought to correspond to the tsunami layers (**Figure 22**). Although there are no pronounced peaks, the ratios are mostly imitating the mean grain-size succession and are serving as supportive proxies for other sedimentological signatures. Similar findings were detected in the western Portuguese shelf sedimentary tsunami (Abrantes et al., 2008), probably because in both cases the coastal cliffs composed of carbonates and not of phyllosilicate rocks. Whereas Smedile et al. (2019) reported better results with these proxies offshore Augusta Bay (Italy) in similar water depths as in the present study. Here, Ti/Sr and Ti/Ca peaks are coinciding with marked coarsening of sediments and peak of organic matter, interpreted as terrestrial run-off. Also, in the study of tsunamigenic turbidite deposits in the southwestern Portuguese margin clear and distinct signals in K/Ti and Ca/Ti are present, suggesting sedimentation of terrigenous material during the 1755 event in this environment (Gràcia et al., 2010) and linked to a schist and grauwacke rocky shore.

4.2.4. Microtextural Surface Features of Quartz Grains

The last sedimentary signature studied is the microtextural features on quartz grain surfaces. This analysis gives only preliminary results and thus can only support other sedimentological tsunami signatures since the sample size is very low with 1 sample for each group (pre, post and tsunami samples). Nonetheless, the present results are coinciding with results of previous studies using the same approach. This consists namely in a significant increase in fresh surface and a slightly increase in percussion mark percentages in tsunami grains compared to pre and post tsunami samples (**Figure 17**). This matches the results of tsunami grains from coastal areas located in the Algarve (south Portugal) corresponding to the same event, as well as in Scotland (Shetland Island and Hebrides Islands) and Lhok Nay Bay (Indonesia) (Costa et al., 2012a). However, Portuguese tsunami grains show high amounts of percussion marks and fresh surfaces, while in the other regions only an increase in fresh surface could be observed. Generally, high subaqueous energy conditions are needed to produce fresh surfaces and percussion marks (**Figure 16**) on grain surfaces (e.g. Mahaney, 2002), which is to be expected during tsunami events when tsunami wave resuspend and erode seafloor sediments. Costa et al. (2012a) discussed that grain flow involving grain interactions can explain the higher abundance of these surface features. Lower concentration of sediments in the turbulent flow are

expected to be the main reason to produce deeper percussion marks and fresh surfaces. In contrary, higher sediment concentration regimes results in higher amount of percussion marks only. This might be due to the shorter distances between single grains and thus less time for accelerations of the grains, resulting in less severe impacts. Hence, the significant higher percentage in fresh surfaces and the subtle increase in percussion marks for tsunami grains does not only present a tsunamigenic sedimentological signature, but also indicates a lower sediment concentration at the seafloor during a tsunami event than on inundated coastal areas. The other analysed microtextures might serve as an indicator of provenance when the sample size is larger.

4.2.5. Provenance of Backwash Sediments

Results obtained by the numerical tsunami modelling suggest the coastal area between Faro and Quarteira as a possible provenance for backwash sediments for all 3 core locations. Sediment sources in that area include beach, dune and coastal lagoon sediments belonging to the Ria Formosa Barrier Island System (Pilkey et al., 1989), containing a diverse composition. The modelled backwash flow predominantly follows a small depression in the topography of the inner shelf in each backwash phase (**Figure 21**). A possible explanation for the weak terrestrial signal in the sedimentological data could be the fact, that the Ria Formosa System with its barrier island inhibits the entrainment of exclusively terrestrial sediments and hence a stronger terrestrial signal. This would coincide with the historical information, that the 1755 tsunami did not inundate further inland than the width of the Ria Formosa in the area around Faro (e.g. Chester and Chester, 2010).

4.3. Dynamic of Tsunami Sedimentation in the Outer Shelf

Considering the different sedimentation processes in offshore environments during a tsunami event (**Figure 1**), the present results provide evidence for sedimentation caused by both, the initial tsunami wave propagation and backwash traction. Although there is no clear sedimentological signature beside the increased mean grain size in core M107 and the findings of Tamura et al. (2015), that coarse sand in tsunami deposits is limited to the nearshore area, calculated bottom velocities > 0.59 m/s of the passing tsunami waves (**Table 12**) suggest an initial erosion of the seafloor sediments compatible with gravel-size sediment (> 2 mm) (Weiss and Bahlburg, 2006). Considering the Green's law (changes of amplitude as a function of water depth) the modelled mean wave amplitudes of > 0.5 m suggest an entrainment of grain with a

size in the range of 1 – 2 mm (very coarse sand) (Weiss, 2008). In a speculative way, the increased amount of fresh surfaces are also suggesting initial resuspending of seafloor sediments induced by the passing tsunami wave, because turbidity current movement only does not result in marking surface textures on quartz grains (Krinsley and Margolis, 1969), but those are present in the tsunami sample. A clear erosion signature is not existing at the base of the studied tsunami layers, probably caused by longer time exposed to post-sedimentary alterations as bioturbation. However, in probable 1755 tsunami deposits in the western Portuguese continental shelf, an erosional contact accompanied by an hiatus of ~ 355 yrs was described (Abrantes et al., 2008). Evidence for the sedimentation caused by backwash are the modelled surface velocities in the backwash phases that are sufficient to transport material to the water depths of the studied core locations (**Figure 21**). Also, sedimentological signatures as the increase in shell fragments in core M106 and POP2, as well as the increase of mica towards the upper tsunami section in core M107 provide evidence of backwash sediments deposited in the outer shelf. Furthermore, the fining grain size distribution in the tsunami layers in core M106 and POP2 suggest backwash induced sedimentation in form of hyperpycnal sediment flows (e.g. Sakuna et al., 2012).

In the case of the 2011 Tohoku-Oki tsunami, Ikehara et al. (2014) were able to define substages of the offshore tsunami deposit sedimentation (~ 122 m water depth) by having sedimentary structures as erosional surfaces and turbiditic sequences coupled with precise chronological evidence due to the release of radionuclides (e.g. ^{134}Cs) by the tsunami related Fukushima No.1 Nuclear Power Plant accident. Thus, surface sediment samples suggest an initial erosional surface followed by 2 turbiditic sequences, interpreted to be deposits by the initial settling of sediments, directly after the tsunami wave propagation and a second deposition caused by the backwash. This also suggests that multiple sequences corresponding to the different tsunami waves and backwash phases (**Figure 20**) are not present in outer shelf sedimentary records. For the case of the 1755 Lisbon tsunami, Quintela et al. (2016) speculatively attributed several peaks of coastal foraminifera to successive backwash phases, forming tsunamigenic subunits in the Portuguese outer shelf. This is supported by the findings of Tamura et al. (2015) but in a shallower environment with conceivable faster sedimentation processes. Several reasons could speak against the preservation of subunits induced by different backwash phases. First, the less precise chronological placement of specific layers in the studied tsunami deposit, as well as the lack in an explicit tsunamigenic sedimentological imprints possibly impedes the clear identification of tsunamigenic sedimentation dynamics in the study

area. Second, the identified heterogenous character of the tsunami deposits indicates a less complex tsunami deposit, covering probably only an initial erosional signature with one or more subsequent settling phases. Third, the amount of time between backwash and incursions of tsunami waves is not sufficient for sediment deposition. For example, a spherical quartz grain with 0.3 mm radius needs ~16 min to reach water depths of ~ 90 m if it is initially located in the upper water column (Rouse, 1938) and probably even longer in denser salt water and prolonging horizontal currents. Considering the settling velocity, it is unlikely to have settling between tsunami waves in offshore regimes with > 90 water depth, because times between the 1755 tsunami waves were approximately 20 – 40 mins (**Figure 19**) (e.g. Omira et al., 2012; Cuven et al., 2013; Ramalho et al., 2018) and directions of the flow at surface changed 180° within this time window (**Figure 20**). Because major part of tsunami sedimentation is probable produced by hyperpycnal bottom flows, the velocity of this current determines if there is a imprint of different tsunami incursions or backwash phases. From studies of hyperpycnal flow characteristics it is known that such currents have velocities of maximal ~ 2 m/s (Mulder et al., 2003), which is not fast enough to reach the core location before the second tsunami wave arrives. Therefore, and based on the Algarve sedimentary record data obtained in this work, we suggest the conceptual model of the sediment processes during the tsunami event leading to offshore tsunami deposits in outer shelf environments with water depths between 60 – 100 m, following the findings of Ikehara et al. (2014): (1) The first passing tsunami wave induces erosion and resuspension of seafloor sediments leaving an erosional contact and probably causing a hiatus. It might also be possible that the earthquake induces liquefaction and resuspension of sediments before the first tsunami wave arrives. (2) Settling of the resuspended sediments leading to a first fining up sequence. Here, sediments are probably not transported to far up in the water column, allowing the settling before the backwash flow arrives. (3) Prolonging highly turbulent water column with high amount of suspended material until conditions change to a lower energy regime again and allow settling of sediments. This implies that offshore tsunami sediment in similar continental shelf settings do not allow differentiation of different tsunami waves or backwash phases (4) Settling of a second fining up sequence with terrigenous material transported by backwash induced hyperpycnal flows. (5) Alteration/ mixing through post-sedimentary processes deteriorating the initial sedimentation pattern.

5. Conclusion and Final Remarks

Core sections of 3 cores from the southern Portuguese shelf were studied to elaborate more evidence for a tsunamigenic origin of before detected high energy event layers by Drago et al. (2016). The cores are sampled from water depths ranging between 57 – 91 m.

Modeled age-depth relations of the levels in the studied sections correlate the high energy event layers to the 1755 Lisbon tsunami event based on Bayesian age modeling of ^{210}Pb and ^{14}C ages. Also, hydrodynamic consideration implies that waves generated by storms, such as the 1941 CE storm event that hit Portugal, cannot reach the seafloor sediments at the locations of the studied cores. Since fluvial floods display different sedimentological characteristics as tsunami deposits and are very rare in the study area it is unlikely that these events deposited the high energy layers. Therefore, it can be assumed that the detected event layers correspond to the 1755 Lisbon tsunami event, which thus left sedimentological signatures in the southern Portuguese outer shelf sedimentary record. Simulated hydrodynamics of the tsunami backwash imply a sediment provenance from the coastal area between Faro and Quarteira, which belongs to the Ria Formosa Barrier Island System. This could explain the weak terrestrial signal in the tsunami layers since entrainment of exclusively terrestrial sediments is inhibited by the Ria Formosa Barrier Island system that impedes further inundation. However, multivariate analysis of the sand composition revealed small but distinguishable differences of tsunami sediments and the background sedimentation. This is supported by a significant increase of fresh surfaces and slightly more abundant percussion marks tsunami quartz grains compared to non-tsunami grains. The microtextural differences could also indicate an initial erosion and resuspension since turbidity current movement only does not result in marking surface textures on quartz grains such as fresh surfaces. The erosion is also backed up by the calculated bottom velocities able to entrain gravel-size sediment (> 2 mm). Sand composition in the studied sections differs between the shallower core location (~ 57 m) and the deeper core location (~ 85 m). Sections from the deeper core locations show in general higher abundance of biogenic components compared to the shallower core, where terrigenous components are more abundant. Also, compared to the pre and post tsunami sections higher mean grain size can be observed in the tsunami layer of the shallower location while lower mean grain size is present in the tsunami layers of the deeper area. Tsunami layers in deeper water depths contain increased shell fragments. This cannot be observed in the tsunami layer of the shallower area but here a higher abundance of mica in the upper part of the tsunami layer indicates similar results: both, shell

fragments and mica have a planar shape, increasing the buoyancy of the particles, and thus they will settle when the energy regime is weakened. These differences of the studied sections can be explained by spatial depositional variations of tsunami sedimentation and different velocities in the respective locations with varying water depths, although a similar fading of the involved sedimentation energy is detected. PCA results of the sand component composition indicate in all core sections a mixing of tsunami samples with pre and post tsunami samples. This heterogeneous sedimentary character of the tsunami layer coupled with hydrodynamic model results suggests, that subunits related to different tsunami wave incursions and backwash phases are unlikely to be preserved in similar environments such as the southern Portuguese outer shelf. The successful application of the new methodologies extends the existing toolkit for the offshore tsunami deposit identification. Also, knowledge of sedimentation dynamic of a tsunami event in a continental shelf setting was improved.

Further studies are needed for better understanding of tsunami-related sedimentation dynamics and processes in outer shelf regions. It would be helpful to study multiple cores aligned in transects perpendicular to the coast and that are located close to areas with maximum inundations, such as Boca do Rio in the southern Algarve. In general, the southern Portuguese shelf seems to be a very good area for studies on tsunamigenic processes. The high numbers of non-identified components in core POP2 is mainly due to the abundant mixed aggregates of both, terrigenous and biogenic components. In the present study no remarkable amount of terrestrial biogenic components such as charcoal are detected. Destroying organic compounds is therefore feasible and thus improve the subsequent statistical analysis. To improve the robustness of the promising microtextural interpretation more samples need to be investigated.

References

Abrantes F, Alt-Epping U, Lebreiro S, Voelker A, Schneider R (2008) Sedimentological record of tsunamis on shallow-shelf areas: The case of the 1969 AD and 1755 AD tsunamis on the Portuguese Shelf off Lisbon. Mar Geol **249**: 283–293

Abrantes F, Lebreiro S, Rodrigues T, Gil I, Bartels-Jónsdóttir H, Oliveira P, Kissel C, Grimalt JO (2005) Shallow-marine sediment cores record climate variability and earthquake activity off Lisbon (Portugal) for the last 2000 years. Quat Sci Rev **24**: 2477–2494

Allen JRL (1985) Principles of Physical Sedimentology. Springer US

Almeida LP, Ferreira Ó, Vousdoukas MI, Dodet G (2011) Historical variation and trends in storminess along the Portuguese South Coast. Nat Hazards Earth Syst Sci **11**: 2407–2417

Andrade C, Freitas MC, Oliveira MA, Costa PJM (2016) On the Sedimentological and Historical Evidences of Seismic-Triggered Tsunamis on the Algarve Coast of Portugal. pp 219–238

Andrade CACF (1990) O ambiente de barreira da Ria Formosa: Algarve-Portugal. Universidade de Lisboa, 645pp.

Andrés Christen J, Pérez E S (2009) A New Robust Statistical Model for Radiocarbon Data. Radiocarbon **51**: 1047–1059

Baptista MA, Heitor S, Miranda JM, Miranda P, Victor LM (1998) The 1755 Lisbon tsunami; evaluation of the tsunami parameters. J Geodyn **25**: 143–157

Baptista MA, Miranda JM (2009) Revision of the Portuguese catalog of tsunamis. Nat Hazards Earth Syst Sci **9**: 25–42

van den Bergh GD, Boer W, De Haas H, van Weering TCE, van Wijhe R (2003) Shallow marine tsunami deposits in Teluk Banten (NW Java, Indonesia), generated by the 1883 Krakatau eruption. Mar Geol **197**: 13–34

Blaauw M, Christen JA (2011) Flexible paleoclimate age-depth models using an autoregressive gamma process. Bayesian Anal **6**: 457–474

Blaauw M, Christen JA, Bennett KD, Reimer PJ (2018) Double the dates and go for Bayes — Impacts of model choice, dating density and quality on chronologies. Quat Sci Rev **188**: 58–66

Blott SJ, Pye K (2001) GRADISTAT: a grain size distribution and statistics package for the analysis of unconsolidated sediments. Earth Surf Process Landforms **26**: 1237–1248

Borcard D, Gillet F, Legendre P (2018) Numerical ecology with R. Springer

Chagué-Goff C (2010) Chemical signatures of palaeotsunamis: A forgotten proxy? Mar Geol **271**: 67–71

Chagué-Goff C, Schneider JL, Goff JR, Dominey-Howes D, Strotz L (2011) Expanding the proxy toolkit to help identify past events - Lessons from the 2004 Indian Ocean Tsunami and the 2009 South Pacific Tsunami. Earth-Science Rev **107**: 107–122

Chagué-Goff C, Szczuciński W, Shinozaki T (2017) Applications of geochemistry in tsunami research: A review. Earth-Science Rev **165**: 203–244

Chester DK, Chester OK (2010) The impact of eighteenth century earthquakes on the Algarve region, southern Portugal. Geogr J **176**: 350–370

Ciavola P, Ferreira Ó, Dias JA, Taborda R (1997) Field measurements of longshore sand transport and control processes on a meso-tidal beach in portugal. J Coast Res **13**: 1119–1129

Coleman PJ (1968) Tsunamis as geological agents. J Geol Soc Aust **15**: 267–273

Costa P, Dourado F, Selle S La, Andrade C, Gelfenbaum G, Silva N, Bosnic I (2019) Modeling sediment transport associated with the AD 1755 tsunami. **21**: 50019

Costa PJM, Andrade C, Dawson AG, Mahaney WC, Freitas MC, Paris R, Taborda R (2012a) Microtextural characteristics of quartz grains transported and deposited by tsunamis and storms. Sediment Geol **275**–**276**: 55–69

Costa PJM, Andrade C, Freitas MC, Oliveira MA, Lopes V, Dawson AG, Moreno J, Fatela F, Jouanneau JM (2012b) A tsunami record in the sedimentary archive of the central Algarve coast, Portugal: Characterizing sediment, reconstructing sources and inundation paths. Holocene **22**: 899–914

Cuven S, Paris R, Falvard S, Miot-Noirault E, Benbakkar M, Schneider JL, Billy I (2013) High-resolution analysis of a tsunami deposit: Case-study from the 1755 lisbon tsunami in southwestern spain. Mar Geol **337**: 98–111

Daniell J, Vervaeck A (2012) Damaging earthquakes database 2011—The year in re-view. 17

Dawson AG, Hindson R, Andrade C, Freitas C, Parish R, Bateman M (1995) Tsunami sedimentation associated with the Lisbon earthquake of 1 November AD 1755: Boca do Rio, Algarve, Portugal. The Holocene **5**: 209–215

Dawson AG, Stewart I (2007) Tsunami deposits in the geological record. Sediment Geol **200**: 166–183

Drago T, Silva P, Lopes A, Magalhães V, Roque C, Rodrigues AI, Noiva J, Terrinha P, Mena A, Francés G, et al (2016) Searching for tsunamis evidences on the Algarve (Southern Portugal) continental shelf sedimentary record. EGU Gen. Assem. 2016, held 17-22 April. 2016 Vienna Austria, id. EPSC2016-16997 18:

Drago, T., Silva, P.F., Magalhães, V., Roque, C., Lopes, A., Rodrigues, A.I., Noiva, J., Terrinha, P., Mena, A., Francés, G., Kopf, A., Völker, D., Salgueiro, E., Alberto, A., Baptista, M.A. (2018). Anomalous sedimentary levels on the south Portuguese continental shelf as potential tsunami evidence, IX Simpósio da Margem Ibérica Atlântica - MIA2018. Universidade de Coimbra, Coimbra, Portugal, pp. 219-220

Einsele G, Chough SK, Shiki T (1996) Depositional events and their records—an introduction. Sediment Geol **104**: 1–9

Fatela F, Taborda R (2002) Confidence limits of species proportions in microfossil assemblages. Mar Micropaleontol **45**: 169–174

Feldens P, Schwarzer K, Sakuna D, Szczuciński W, Sompongchaiyakul P (2012) Sediment distribution on the inner continental shelf off Khao Lak (Thailand) after the 2004 Indian Ocean tsunami. Earth, Planets Sp **64**: 875–887

Feldens P, Schwarzer K, Szczuciński W, Stattegger K, P DS, Kiel D (2008) Impact of the 2004 Indian Ocean Tsunami on seafloor morphology and sediments offshore Pakarang Cape , Thailand The research area Methods. Methods **18**: 63–68

Folk RL, Ward WC (1957) Brazos River bar [Texas]; a study in the significance of grain size parameters. J Sediment Res **27**: 3–26

Font E, Nascimento C, Omira R, Baptista MA, Silva PF (2010) Identification of tsunami-induced deposits using numerical modeling and rock magnetism techniques: A study case of the 1755 Lisbon tsunami in Algarve, Portugal. Phys Earth Planet Inter **182**: 187–198

Font E, Veiga-Pires C, Pozo M, Nave S, Costas S, Ruiz Muñoz F, Abad M, Simões N, Duarte S, Rodríguez-Vidal J (2013) Benchmarks and sediment source(s) of the 1755 Lisbon tsunami deposit at Boca do Rio Estuary. Mar Geol **343**: 1–14

Fortunato AB, Freire P, Bertin X, Rodrigues M, Ferreira J, Liberato MLR (2017) A numerical study of the February 15, 1941 storm in the Tagus estuary. Cont Shelf Res **144**: 50–64

Fowler AJ, Gillespie R, Hedges REM (1986) Radiocarbon Dating of Sediments. Radiocarbon **28**: 441–450

Freitas JG, Dias JA (2013) 1941 windstorm effects on the Portuguese Coast. What lessons for the future? J Coast Res **65**: 714–719

Fujiwara O, Kamataki T (2007) Identification of tsunami deposits considering the tsunami waveform: An example of subaqueous tsunami deposits in Holocene shallow bay on southern Boso Peninsula, Central Japan. Sediment Geol **200**: 295–313

Goff J, Chagué-Goff C, Nichol S, Jaffe B, Dominey-Howes D (2012) Progress in palaeotsunami research. Sediment Geol **243**–**244**: 70–88

Goodman-Tchernov BN, Austin JA (2015) Deterioration of Israel's Caesarea Maritima's ancient harbor linked to repeated tsunami events identified in geophysical mapping of offshore stratigraphy. J Archaeol Sci Reports **3**: 444–454

Goodman-Tchernov BN, Dey HW, Reinhardt EG, McCoy F, Mart Y (2009) Tsunami waves generated by the Santorini eruption reached Eastern Mediterranean shores. Geology **37**: 943–946

Goodman Tchernov B, Katz T, Shaked Y, Qupty N, Kanari M, Niemi T, Agnon A (2016) Offshore Evidence for an Undocumented Tsunami Event in the 'Low Risk' Gulf of Aqaba-Eilat, Northern Red Sea. PLoS One **11**: e0145802

Gràcia E, Vizcaino A, Escutia C, Asioli A, Rodés Á, Pallàs R, Garcia-Orellana J, Lebreiro S, Goldfinger C (2010) Holocene earthquake record offshore Portugal (SW Iberia): testing turbidite paleoseismology in a slow-convergence margin. Quat Sci Rev **29**: 1156–1172

Hamblin (1962) X-ray Radiography in the Study of Structures in Homogeneous Sediments. SEPM J Sediment Res **Vol. 32**: 201–210

Helal MA, Mehanna MS (2008) Tsunamis from nature to physics. Chaos, Solitons & Fractals **36**: 787–796

Hilbe JM (2014) Negative Binomial Regression. Model. Count Data. Cambridge University Press, Cambridge, pp 126–161

Hindson R a., Andrade C, Dawson a. G (1996) Sedimentary processes associated with the tsunami generated by the 1755 Lisbon earthquake on the Algarve coast, Portugal. Phys Chem Earth **21**: 57–63

Hindson RA, Andrade C (1999) Sedimentation and hydrodynamic processes associated with the tsunami generated by the 1755 Lisbon earthquake. Quat Int **56**: 27–38

Ikehara K, Irino T, Usami K, Jenkins R, Omura A, Ashi J (2014) Possible submarine tsunami deposits on the outer shelf of Sendai Bay, Japan resulting from the 2011 earthquake and tsunami off the Pacific coast of Tohoku. Mar Geol **349**: 91–98

Jagodziński R, Sternal B, Szczuciński W, Sugawara D (2012) Heavy minerals in the 2011 Tohoku-oki tsunami deposits—insights into sediment sources and hydrodynamics. Sediment Geol **282**: 57–64

Johnston AC (1996) Seismic moment assessment of earthquakes in stable continental regions-III. New Madrid 1811-1812, Charleston 1886 and Lisbon 1755. Geophys J Int **126**: 314–344

Jonathan MP, Srinivasalu S, Thangadurai N, Rajeshwara-Rao N, Ram-Mohan V, Narmatha T (2012) Offshore depositional sequence of 2004 tsunami from Chennai, SE coast of India. Nat Hazards **62**: 1155–1168

Kastens KA, Cita MB (1981) Tsunami-induced sediment transport in the abyssal Mediterranean Sea. Geol Soc Am Bull **92**: 845–857

Krinsley D, Margolis S (1969) Section of geological sciences: a study of quartz sand grain surface textures with the scanning electron microscope. Trans N Y Acad Sci **31**: 457–477

Kruskal WH, Wallis WA (1952) Use of Ranks in One-Criterion Variance Analysis. J Am Stat Assoc **47**: 583–621

Lawless JF (1987) Negative binomial and mixed poisson regression. Can J Stat **15**: 209–225

Legendre P, Gallagher ED (2001) Ecologically meaningful transformations for ordination of species data. Oecologia **129**: 271–280

Lobo F., Sánchez R, González R, Dias JM., Hernández-Molina F., Fernández-Salas L., Díaz del Río V, Mendes I (2004) Contrasting styles of the Holocene highstand sedimentation and sediment dispersal systems in the northern shelf of the Gulf of Cadiz. Cont Shelf Res **24**: 461–482

Luis JF (2007) Mirone: A multi-purpose tool for exploring grid data. Comput Geosci **33**: 31–41

M. C. Powers MC (1953) A New Roundness Scale for Sedimentary Particles. SEPM J Sediment Res **Vol. 23**: 117–119

Magalhães F (2001) Os sedimentos da plataforma continental portuguesa: contrastes espaciais.

Mahaney WC (2002) Atlas of sand grain surface textures and applications. Oxford University Press, USA

Maher BA, Watkins SJ, Brunskill G, Alexander J, Fielding CR (2009) Sediment provenance in a tropical fluvial and marine context by magnetic "fingerprinting" of transportable sand fractions. Sedimentology **56**: 841–861

Malmgren BA, Haq BU (1982) Assessment of quantitative techniques in paleobiogeography. Mar Micropaleontol **7**: 213–236

Matias LM, Cunha T, Annunziato A, Baptista MA, Carrilho F (2013) Tsunamigenic earthquakes in the Gulf of Cadiz: Fault model and recurrence. Nat Hazards Earth Syst Sci **13**: 1–13

Milker Y, Wilken M, Schumann J, Sakuna D, Feldens P, Schwarzer K, Schmiedl G (2013) Sediment transport on the inner shelf off Khao Lak (Andaman Sea, Thailand) during the 2004 Indian Ocean tsunami and former storm events: Evidence from foraminiferal transfer functions. Nat Hazards Earth Syst Sci **13**: 3113–3128

Miranda JM, Luis JF, Reis C, Omira R, Baptista MA (2014) Validation of NSWING , a multi-core finite difference code for tsunami propagation and run-up. Poster 1–2

Moita I (1986) Noticia Explicativa da Carta dos Sedimentos Superficiais da Plataforma, Folha SED 8. Inst. Hidrográfico

Monge Soares AM (1993) The 14C content of marine shells: Evidence for variability in coastal upwelling off Portugal during the Holocene. IAEA, International Atomic Energy Agency (IAEA)

Moreira S, Costa PJM, Andrade C, Ponte Lira C, Freitas MC, Oliveira MA, Reichart G-J (2017) High resolution geochemical and grain-size analysis of the AD 1755 tsunami deposit: Insights into the inland extent and inundation phases. Mar Geol **390**: 94–105

Morton RA, Gelfenbaum G, Jaffe BE (2007) Physical criteria for distinguishing sandy tsunami and storm deposits using modern examples. Sediment Geol **200**: 184–207

Mulder T, Syvitski JPM, Migeon S, Faugères JC, Savoye B (2003) Marine hyperpycnal flows: Initiation, behaviorand related deposits. A review. Mar Pet Geol **20**: 861–882

Nanayama F, Satake K, Furukawa R, Shimokawa K, Atwater BF, Shigeno K, Yamaki S (2003) Unusually large earthquakes inferred from tsunami deposits along the Kuril trench. Nature **424**: 660–663

Neumann B, Vafeidis AT, Zimmermann J, Nicholls RJ (2015) Future coastal population growth and exposure to sea-level rise and coastal flooding - A global assessment. PLoS One. doi: 10.1371/journal.pone.0118571

Noda A, Katayama H, Sagayama T, Suga K, Uchida Y, Satake K, Abe K, Okamura Y (2007) Evaluation of tsunami impacts on shallow marine sediments: An example from the tsunami caused by the 2003 Tokachi-oki earthquake, northern Japan. Sediment Geol **200**: 314–327

Nomaki H, Arai K, Suga H, Toyofuku T, Wakita M, Nunoura T, Oguri K, Kasaya T, Watanabe S (2016) Sedimentary organic matter contents and porewater chemistry at upper bathyal depths influenced by the 2011 off the Pacific coast of Tohoku Earthquake and tsunami. J Oceanogr **72**: 99–111

O'Hara RB, Kotze DJ (2010) Do not log-transform count data. Methods Ecol Evol **1**: 118–122

Ogston AS, Cacchione DA, Sternberg RW, Kineke GC (2000) Observations of storm and river flood-driven sediment transport on the northern California continental shelf. Cont Shelf Res **20**: 2141–2162

Oksanen J, Blanchet FG, Friendly M, Kindt R, Legendre P, McGlinn D, Minchin PR, O'Hara RB, Simpson GL, Solymos P, et al (2019) vegan: Community Ecology Package.

Omira R, Baptista MA, Matias L, Miranda JM, Catita C, Carrilho F, Toto E (2009) Design of a sea-level tsunami detection network for the Gulf of Cadiz. Nat Hazards Earth Syst Sci **9**: 1327–1338

Omira R, Baptista MA, Mellas S, Leone F, Richemond NM De, Zourarah B, Cherel J (2012) The November , 1 st , 1755 Tsunami in Morocco : Can Numerical Modeling Clarify the Uncertainties of Historical Reports ? doi: 10.5772/2614

Ortega JA, Garzón G (2009) A contribution to improved flood magnitude estimation in base of palaeoflood record and climatic implications - Guadiana River (Iberian Peninsula). Nat Hazards Earth Syst Sci **9**: 229–239

Papadopoulos G (2015) Tsunamigenic Sources and Generation Mechanisms. Tsunamis Eur. Reg. Elsevier, pp 101–119

Paris R, Fournier J, Poizot E, Etienne S, Morin J, Lavigne F, Wassmer P (2010) Boulder and fine sediment transport and deposition by the 2004 tsunami in Lhok Nga (western Banda Aceh, Sumatra, Indonesia): A coupled offshore–onshore model. Mar Geol **268**: 43–54

Pilarczyk JE, Sawai Y, Matsumoto D, Namegaya Y, Nishida N, Ikehara K, Fujiwara O, Gouramanis C, Dura T, Horton BP (2019) Constraining sediment provenance for tsunami deposits using distributions of grain size and foraminifera from the Kujukuri coastline and shelf, Japan. Sedimentology sed.12591

Pilkey OH, Neal WJ, Monteiro JH, Dias JMA (1989) Algarve barrier islands: a noncoastal-plain system in Portugal. J Coast Res **5**: 239–261

Pongpiachan S (2014) Application of binary diagnostic ratios of polycyclic aromatic hydrocarbons for identification of tsunami 2004 backwash sediments in khao lak, Thailand. Sci World J. doi: 10.1155/2014/485068

Pongpiachan S, Thumanu K, Na Phatthalung W, Tipmanee D, Kanchai P, Feldens P, Schwarzer

K (2013) Using Fourier Transform Infrared (FTIR) to characterize tsunami deposits in near-shore and coastal waters of Thailand. Int J Tsunami Soc **20**: 57–102

Quintela M, Costa PJM, Fatela F, Drago T, Hoska N, Andrade C, Freitas MC (2016) The AD 1755 tsunami deposits onshore and offshore of Algarve (south Portugal): Sediment transport interpretations based on the study of Foraminifera assemblages. Quat Int **408**: 123–138

Ramalho I, Omira R, El Moussaoui S, Baptista MA, Zaghloul MN (2018) Tsunami-induced morphological change – A model-based impact assessment of the 1755 tsunami in NE Atlantic from the Morocco coast. Geomorphology **319**: 78–91

Reed AJ, Mann ME, Emanuel KA, Lin N, Horton BP, Kemp AC, Donnelly JP (2015) Increased threat of tropical cyclones and coastal flooding to New York City during the anthropogenic era. Proc Natl Acad Sci U S A **112**: 12610–12615

Reimer PJ, Bard E, Bayliss A, Beck JW, Blackwell PG, Ramsey CB, Buck CE, Cheng H, Edwards RL, Friedrich M, et al (2013) IntCal13 and Marine13 Radiocarbon Age Calibration Curves 0–50,000 Years cal BP. Radiocarbon **55**: 1869–1887

Reinhardt EG, Goodman BN, Boyce JI, Lopez G, van Hengstum P, Rink WJ, Mart Y, Raban A (2006) The tsunami of 13 December A.D. 115 and the destruction of Herod the Great's harbor at Caesarea Maritima, Israel. Geology **34**: 1061

Rhodes B, Tuttle M, Horton B, Doner L, Kelsey H, Nelson A, Cisternas M (2006) Paleotsunami research. Eos, Trans Am Geophys Union **87**: 205

Riou B, Chaumillon E, Schneider J-L, Corrège T, Chagué C (2018) The sediment-fill of Pago Pago Bay (Tutuila Island, American Samoa): New insights on the sediment record of past tsunamis. Sedimentology. doi: 10.1111/sed.12574

Robbins JA (1978) Geochemical and geophysical applications of radioactive lead. Biochem. lead Environ. Elsevier Scientific, pp 283–393

Röbke BR, Vött A (2017) The tsunami phenomenon. Prog Oceanogr **159**: 296–322

Roque, C.; Hernández-Molina, F. J.; Lobo, F.; Somoza, L.; Díaz-de-Río, V.; Vázquez, J. T. & Dias J (2010) Geomorphology of the Eastern Algarve proximal continental margin (South Portugal , SW Iberia Peninsula): sedimentary dynamics and its relationship with the last asymmetrical eustatic cycle. Ciencias da Terra 17 **17**: 7–28

Rouse H (1938) Nomogram for the settling velocity of spheres.

Le Roux JP, Vargas G (2005) Hydraulic behavior of tsunami backflows: insights from their modern and ancient deposits. Environ Geol **49**: 65–75

Sakuna-Schwartz D, Feldens P, Schwarzer K, Khokiattiwong S, Stattegger K (2015) Internal structure of event layers preserved on the Andaman Sea continental shelf, Thailand: tsunami vs. storm and flash-flood deposits. Nat Hazards Earth Syst Sci **15**: 1181–1199

Sakuna D, Szczuciński W, Feldens P, Schwarzer K, Khokiattiwong S (2012) Sedimentary deposits left by the 2004 Indian Ocean tsunami on the inner continental shelf offshore of Khao Lak, Andaman Sea (Thailand). Earth, Planets Sp **64**: 931–943

Scheffers SR, Haviser J, Browne T, Scheffers A (2009) Tsunamis, hurricanes, the demise of coral reefs and shifts in prehistoric human populations in the Caribbean. Quat Int **195**: 69–87

Shanmugam G (2012) Process-sedimentological challenges in distinguishing paleo-tsunami deposits. Nat Hazards **63**: 5–30

Smedile A, De Martini PM, Pantosti D (2012) Combining inland and offshore paleotsunamis evidence: The Augusta Bay (eastern Sicily, Italy) case study. Nat Hazards Earth Syst Sci **12**: 2557–

2567

Smedile A, De Martini PM, Pantosti D, Bellucci L, Del Carlo P, Gasperini L, Pirrotta C, Polonia A, Boschi E (2011) Possible tsunami signatures from an integrated study in the Augusta Bay offshore (Eastern Sicily-Italy). Mar Geol **281**: 1–13

Smedile A, Molisso F, Chagué C, Iorio M, De Martini PM, Pinzi S, Collins PEF, Sagnotti L, Pantosti D (2019) New coring study in Augusta Bay expands understanding of offshore tsunami deposits (Eastern Sicily, Italy). Sedimentology. doi: 10.1111/sed.12581

Srinivasalu S, Jonathan MP, Thangadurai N, Ram-Mohan V (2010) A study on pre- and post-tsunami shallow deposits off SE coast of India from the 2004 Indian Ocean tsunami: a geochemical approach. Nat Hazards **52**: 391–401

Sugawara D, Goto K (2012) Numerical modeling of the 2011 Tohoku-oki tsunami in the offshore and onshore of Sendai Plain, Japan. Sediment Geol **282**: 110–123

Sugawara D, Minoura K, Nemoto N, Tsukawaki S, Goto K, Imamura F (2009) Foraminiferal evidence of submarine sediment transport and deposition by backwash during the 2004 Indian Ocean tsunami. Isl Arc **18**: 513–525

Tamura T, Sawai Y, Ikehara K, Nakashima R, Hara J, Kanai Y (2015) Shallow-marine deposits associated with the 2011 Tohoku-oki tsunami in Sendai Bay, Japan. J Quat Sci **30**: 293–297

Tavares R (2014) Tsunami and Storm Surge Modelling in the North East Atlantic. doi: 10.2788/18260

Team R (2017) R: A language and environment for statistical computing (Version 3.4. 2)[Computer software]. Vienna, Austria R Found. Stat. Comput.

Tipmanee D, Deelaman W, Pongpiachan S, Schwarzer K, Sompongchaiyakul P (2012) Using Polycyclic Aromatic Hydrocarbons (PAHs) as a chemical proxy to indicate Tsunami 2004 backwash in Khao Lak coastal area, Thailand. Nat Hazards Earth Syst Sci **12**: 1441–1451

Toyofuku T, Duros P, Fontanier C, Mamo B, Bichon S, Buscail R, Chabaud G, Deflandre B, Goubet S, Grémare A, et al (2014) Unexpected biotic resilience on the Japanese seafloor caused by the 2011 To¯hoku-Oki tsunami. Sci Rep. doi: 10.1038/srep07517

Tyuleneva N, Braun Y, Katz T, Suchkov I, Goodman-Tchernov B (2018) A new chalcolithic-era tsunami event identified in the offshore sedimentary record of Jisr al-Zarka (Israel). Mar Geol **396**: 67–78

Umitsu M, Tanavud C, Patanakanog B (2007) Effects of landforms on tsunami flow in the plains of Banda Aceh, Indonesia, and Nam Khem, Thailand. Mar Geol **242**: 141–153

Veerasingam S, Venkatachalapathy R, Basavaiah N, Ramkumar T, Venkatramanan S, Deenadayalan K (2014) Identification and characterization of tsunami deposits off southeast coast of India from the 2004 Indian Ocean tsunami: Rock magnetic and geochemical approach. J Earth Syst Sci **123**: 905–921

Veiga-Pires C, Mestre NC (2009) Is it possible to use "twin cores" as a unique sedimentary record? An experimental design based on sediment color . IOP Conf Ser Earth Environ Sci **5**: 012011

Vigliotti L, Andrade C, Conceição F, Capotondi L, Gallerani A, Bellucci LG (2019) Paleomagnetic, rock magnetic and geochemical study of the 1755 tsunami deposit at Boca do Rio (Algarve, Portugal). Palaeogeogr Palaeoclimatol Palaeoecol **514**: 550–566

Ward SN (2001) Landslide tsunami. J Geophys Res Solid Earth **106**: 11201–11215

Warton DI, Lyons M, Stoklosa J, Ives AR (2016) Three points to consider when choosing a LM or GLM test for count data. Methods Ecol Evol **7**: 882–890

Weiss R (2008) Sediment grains moved by passing tsunami waves: Tsunami deposits in deep water. Mar Geol **250**: 251–257

Weiss R, Bahlburg H (2006) A Note on the Preservation of Offshore Tsunami Deposits. J Sediment Res **76**: 1267–1273

Wheatcroft RA, Drake DE (2003) Post-depositional alteration and preservation of sedimentary event layers on continental margins, I. The role of episodic sedimentation. Mar Geol **199**: 123–137

Wickham H (2016) ggplot2: Elegant Graphics for Data Analysis. Springer-Verlag New York

Yang W, Zhou X, Xiang R, Wang Y, Sun L (2017) Palaeotsunami in the East China Sea for the past two millennia: A perspective from the sedimentary characteristics of mud deposit on the continental shelf. Quat Int **452**: 54–64

Zitellini N, Gràcia E, Matias L, Terrinha P, Abreu MA, DeAlteriis G, Henriet JP, Dañobeitia JJ, Masson DG, Mulder T, et al (2009) The quest for the Africa–Eurasia plate boundary west of the Strait of Gibraltar. Earth Planet Sci Lett **280**: 13–50

Annex

Annex A: Sample and Fraction Weights

Weights of the fractions and the total sample weight. C. Sed. = Coarse Sediment (< -1 Φ – 4 Φ); F. Sed. = Fine Sediment (> 4 Φ).

POP2 (POPEI2-1-CGP)

Sample [cm]	< -1 Φ [g]	0 | -1 Φ [g]	0 - 1 Φ [g]	1 | 2 Φ [g]	2 | 3 Φ [g]	3 | 4 Φ [g]	C. Sed. [g]	F. Sed. [g]	Total [g]
50-51	0.0004	0.003	0.0029	0.0144	0.0402	0.231	0.2919	6.098	6.3899
51-52	0	0	0.0017	0.0126	0.033	0.1897	0.237	5.344	5.581
52-53	0	0	0.0012	0.0056	0.0179	0.1352	0.1599	3.949	4.1089
53-54	0	0	0.001	0.005	0.0133	0.0756	0.0949	1.708	1.8029
54-55	0	0	0.001	0.0115	0.0363	0.1592	0.208	4.276	4.484
55-56	0	0.0041	0.0013	0.0089	0.0434	0.1996	0.2573	4.354	4.6113
56-57	0	0	0.0024	0.0113	0.0373	0.2295	0.2805	5.659	5.9395
57-58	0	0.0016	0.0028	0.0133	0.0409	0.2135	0.2721	5.176	5.4481
58-59	0	0.0015	0.0005	0.0123	0.0412	0.2487	0.3042	6.281	6.5852
59-60	0.08	0.0002	0.0016	0.0172	0.0345	0.2109	0.3444	5.877	6.2214
60-61	0	0	0.0004	0.0079	0.0175	0.0929	0.1187	1.724	1.8427
61-62	0.0093	0.003	0.0031	0.022	0.0383	0.2728	0.3485	6.689	7.0375
62-63	0.008	0	0.0021	0.0199	0.0359	0.2038	0.2697	4.88	5.1497
63-64	0	0.0002	0.0017	0.0253	0.0515	0.4048	0.4835	8.695	9.1785
64-65	0	0.0035	0.0029	0.0033	0.0331	0.2438	0.2866	5.925	6.2116
65-66	0.0259	0	0.0009	0.0206	0.0438	0.3298	0.421	6.786	7.207
66-67	0	0.0001	0.002	0.0154	0.0353	0.2186	0.2714	5.388	5.6594
67-68	0	0.002	0.005	0.015	0.046	0.451	0.519	8	8.519
68-69	0	0	0.0023	0.0121	0.0469	0.3517	0.413	6.845	7.258
69-70	0	0	0.0016	0.0112	0.0445	0.3558	0.4131	5.718	6.1311
70-71	0	0	0.0028	0.0107	0.0372	0.3764	0.4271	6.48	6.9071
71-72	0	0	0.0007	0.006	0.0365	0.2266	0.2698	3.661	3.9308
72-73	0	0.0007	0.0001	0.0162	0.0611	0.5948	0.6729	7.963	8.6359
73-74	0	0.0008	0.0004	0.0146	0.0556	0.6521	0.7235	8.49	9.2135
74-75	0	0	0.0005	0.0085	0.0361	0.3805	0.4256	5.497	5.9226
75-76	0	0.0022	0.005	0.0066	0.0378	0.4488	0.5004	7.043	7.5434
76-77	0	0.0035	0.0024	0.0108	0.0486	0.5743	0.6396	7.229	7.8686
77-78	0	0	0.0005	0.0099	0.0521	0.5275	0.59	6.321	6.911
78-79	0	0	0	0.001	0.0079	0.0736	0.0825	0.635	0.7175
79-80	0	0.002	0.0022	0.0044	0.0276	0.289	0.3252	3.162	3.4872

M106 (MW-GC-106)

Sample [cm]	< -1 Φ [g]	0 | -1 Φ [g]	0 - 1 Φ [g]	1 | 2 Φ [g]	2 | 3 Φ [g]	3 | 4 Φ [g]	C. Sed. [g]	F. Sed. [g]	Total [g]
52-53	0	0.0012	0.0018	0.0026	0.011	0.0292	0.0458	3.788	3.8338
53-54	0	0	0.0001	0.0012	0.0034	0.012	0.0167	1.44	1.4567
54-55	0.0054	0	0.0007	0.0042	0.0107	0.0401	0.0611	4.98	5.0411
56-57	0	0.0013	0	0.0017	0.0057	0.0279	0.0366	3.199	3.2356
57-58	0	0.0021	0.0012	0.0025	0.0085	0.0308	0.0451	3.501	3.5461
58-59	0	0.0014	0.0001	0.0035	0.0102	0.0393	0.0545	4.291	4.3455
59-60	0	0	0.0001	0.002	0.0064	0.0214	0.0299	2.746	2.7759
60-61	0	0	0.0005	0.0019	0.0079	0.0272	0.0375	3.119	3.1565
61-62	0	0.0007	0.0005	0.0029	0.013	0.0455	0.0626	4.464	4.5266
62-63	0	0.0002	0.0007	0.0014	0.0064	0.028	0.0367	3.111	3.1477
63-64	0	0	0.0009	0.0052	0.0157	0.0481	0.0699	4.882	4.9519
64-65	0	0.0007	0.0005	0.0031	0.0096	0.0468	0.0607	4.577	4.6377
65-66	0	0	0.0002	0.0027	0.0112	0.0322	0.0463	3.487	3.5333
66-67	0	0.0016	0.0019	0.0028	0.0055	0.0275	0.0393	2.86	2.8993
67-68	0.0007	0.003	0.0005	0.0051	0.0173	0.0453	0.0719	4.391	4.4629
68-69	0	0	0.0005	0.0042	0.0087	0.0314	0.0448	2.861	2.9058
69-70	0.0289	0.001	0.0029	0.009	0.0212	0.0678	0.1308	5.829	5.9598
70-71	0	0.0006	0	0.0014	0.0064	0.0269	0.0353	1.937	1.9723
71-72	0	0	0.0004	0.0045	0.0171	0.0734	0.0954	5.578	5.6734
72-73	0	0	0.0001	0.0017	0.0079	0.024	0.0337	2.567	2.6007
73-74	0	0	0.0002	0.0016	0.0074	0.0126	0.0218	1.076	1.0978
74-75	0	0	0	0.0018	0.0047	0.032	0.0385	1.904	1.9425
76-77	0.003	0.0008	0.0009	0.0021	0.0076	0.0448	0.0592	2.357	2.4162
77-78	0	0	0.0001	0.0061	0.0246	0.1161	0.1469	5.717	5.8639
78-79	0	0	0.0004	0.0028	0.0082	0.0423	0.0537	2.228	2.2817
79-80	0	0	0.005	0.0036	0.0124	0.0401	0.0611	2.755	2.8161
80-81	0	0	0.0001	0.0044	0.0276	0.0585	0.0906	4.298	4.3886

M107 (MW-GC-107)

Sample [cm]	< -1 Φ [g]	0 | -1 Φ [g]	0 - 1 Φ [g]	1 | 2 Φ [g]	2 | 3 Φ [g]	3 | 4 Φ [g]	C. Sed. [g]	F. Sed. [g]	Total [g]
8-9	0.1585	0.0041	0.0469	0.062	0.0961	0.8339	1.2015	2.336	3.5375
9-10	0.0425	0.0303	0.0245	0.0596	0.1178	0.8664	1.1411	2.451	3.5921
10-11	0	0.0033	0.0238	0.0497	0.1121	0.7376	0.9265	1.926	2.8525
11-12	0.2251	0.0309	0.0393	0.0611	0.1026	0.8467	1.3057	2.367	3.6727
12-13	0.2463	0.0196	0.0485	0.0613	0.1001	0.8313	1.3071	2.274	3.5811
13-14	0.1189	0.0259	0.0572	0.0722	0.1216	0.8484	1.2442	2.402	3.6462
14-15	0	0.011	0.032	0.0681	0.1415	1.0731	1.3257	2.48	3.8057
15-16	0	0.0076	0.0263	0.0727	0.1822	1.2702	1.559	2.968	4.527
16-17	0.0537	0.0496	0.0428	0.0827	0.1535	1.1105	1.4928	2.665	4.1578
17-18	0.037	0.032	0.0476	0.0856	0.1438	1.1046	1.4506	2.457	3.9076

18-19	0.2045	0.0493	0.0561	0.0761	0.1708	1.1202	1.677	2.315	3.992
19-20	0.1892	0.1595	0.0988	0.0648	0.1153	0.9398	1.5674	2.087	3.6544
20-21	0.3884	0.1258	0.2413	0.0981	0.1203	0.7859	1.7598	1.372	3.1318
21-22	0.1022	0.0589	0.0743	0.1193	0.1839	1.4042	1.9428	2.442	4.3848
22-23	0.1665	0.0239	0.0858	0.1139	0.1929	1.2746	1.8576	2.075	3.9326
23-24	0.0975	0.0453	0.2078	0.1256	0.1504	1.021	1.6476	1.459	3.1066
24-25	0	0.0394	0.1002	0.0916	0.1449	1.1738	1.5499	1.8	3.3499
25-26	0.304	0.0796	0.0918	0.115	0.1684	1.2255	1.9843	1.875	3.8593
26-27	0.1476	0.1077	0.1521	0.1276	0.165	1.1813	1.8813	1.419	3.3003
27-28	0.0625	0.0973	0.1134	0.1288	0.1705	1.1588	1.7313	1.539	3.2703
28-29	0.0707	0.0496	0.0933	0.1095	0.1639	1.2128	1.6998	1.588	3.2878
29-30	0.0762	0.1244	0.0972	0.1085	0.1612	1.1738	1.7413	2.232	3.9733
30-31	0.0371	0.0451	0.1157	0.1239	0.1742	1.359	1.855	2.034	3.889
31-32	0.3103	0.1145	0.1698	0.1975	0.1602	1.0857	2.038	1.749	3.787

Annex B: Count Table of Pilot Study

Abbreviations: Other Terr. = Other Terrigenous; Plank. Foram = Planktonic Foraminifera; Benth. Foram = Benthic Foraminifera; Terr. Biogenic = Terrestrial Biogenic.

Sample	M107 15-16 cm					M107 18-19 cm					M107 21-22 cm				
Fraction	1000-500 µm	500-250 µm	250-125 µm	500-250 µm	250-125 µm	1000-500 µm	500-250 µm	250-125 µm	500-250 µm	250-125 µm	1000-500 µm	500-250 µm	250-125 µm	500-250 µm	250-125 µm
Quartz	24	20	7	108	79	42	27	28	102	96	54	35	22	107	72
Mica	0	2	3	1	20	0	1	19	5	22	1	10	13	7	30
Opaque	1	4	6	7	5	1	1	2	5	10	0	1	2	3	5
Aggregate	4	2	4	6	5	43	2	3	10	2	10	2	2	4	5
Other Terr.	1	7	8	21	22	4	3	11	24	30	3	10	10	17	22
Plank. Foram	0	6	6	36	9	0	4	1	6	9	0	3	1	7	16
Benth. Foram	9	16	19	62	48	0	28	11	52	34	3	12	9	37	35
Mollusc	28	8	11	10	30	8	11	9	34	29	18	13	9	39	32
Terr. Biogenic	0	0	0	0	0	0	0	0	0	0	0	2	1	1	1
Other Biogenic	14	31	23	33	78	1	19	14	55	59	11	11	24	66	76
Non-Identified	19	4	13	16	4	1	4	2	7	9	0	1	7	12	6
Total Counts	100	100	100	300	300	100	100	100	300	300	100	100	100	300	300

Continuation of table:

Sample	M107 25-26 cm					M107 28-29 cm				
Fraction	1000-500 µm	500-250 µm	250-125 µm	500-250 µm	250-125 µm	1000-500 µm	500-250 µm	250-125 µm	500-250 µm	250-125 µm
Quartz	41	31	23	132	53	45	43	28	119	85

Mica	1	3	8	6	26	2	4	14	10	24
Opaque	0	3	5	4	16	0	1	3	7	10
Aggregate	21	1	1	4	6	12	1	1	3	4
Other Terr.	7	6	11	20	24	4	6	11	21	26
Plank. Foram	0	5	7	9	14	0	3	4	12	18
Benth. Foram	1	12	15	35	53	4	12	13	30	46
Mollusc	23	15	6	29	32	27	9	6	36	22
Terr. Biogenic	0	0	0	0	1	0	1	0	1	1
Other Biogenic	6	21	21	57	69	5	17	19	54	58
Non-Identified	0	3	3	4	6	1	3	1	7	6
Total Counts	100	100	100	300	300	100	100	100	300	300

Annex C: Sand Component Counts

Raw counts of the sand components. Sa = Sample; Qz = Quartz; Oq = Opaque; Ag = Aggregate; OT = Other Terrigenous; PF = Planktonic Foraminifera; BF = Benthic Foraminifera; Ml = Mollusc; TB = Terrestrial Biogenic; OB = Other Biogenic; NI = Non-Identified. E.g. sample '50' stands for the interval 50 – 51 cm etc.

POP2 (POPEI2-1-CGP

Sa	Qz	Mi	Oq	Ag	OT	PF	BF	Ml	TB	OB	NI
50	6	4	1	3	0	16	33	3	0	27	7
51	4	6	0	3	1	8	31	3	0	36	8
52	9	6	3	4	1	9	31	4	0	30	3
53	10	7	0	3	0	10	20	4	0	41	5
54	3	3	4	6	2	12	33	3	0	28	6
55	4	5	3	4	0	12	38	1	0	26	7
56	6	6	1	3	2	9	27	2	0	37	7
57	2	8	0	3	2	6	37	4	0	32	6
58	6	4	1	2	1	11	28	5	0	35	7
59	5	8	0	6	2	8	26	3	0	31	11
60	6	6	0	2	2	4	18	16	0	43	3
61	4	5	0	15	2	7	21	5	2	30	9
62	3	10	2	0	2	14	32	2	2	22	11
63	3	5	0	1	0	14	43	1	0	21	12
64	10	7	1	10	2	10	29	7	2	11	11
65	4	8	1	2	2	9	28	5	1	31	9

66	6	6	1	6	1	7	34	2	1	20	16
68	7	11	1	12	2	5	34	3	2	15	8
69	1	8	0	13	4	12	36	3	2	14	7
70	7	8	2	19	3	5	32	1	0	14	9
71	9	9	2	11	4	3	35	1	0	14	12
72	4	6	0	4	2	16	33	2	1	24	8
73	4	6	1	5	2	21	40	2	0	16	3
74	5	10	0	9	1	9	30	4	0	24	8
75	11	14	0	13	1	11	26	3	0	11	10
76	3	10	1	7	1	8	36	1	0	25	8
77	7	7	1	17	2	9	29	4	0	16	8
78	13	8	1	6	2	6	37	2	0	23	2
79	9	7	2	11	4	16	36	2	0	8	5

M106 (MW14-GC-106)

Sa	Qz	Mi	Oq	Ag	OT	PF	BF	Ml	TB	OB	NI
52	6	5	1	13	2	13	26	4	0	23	7
53	8	15	4	20	1	6	23	1	0	18	4
54	7	4	2	6	2	8	35	4	0	28	4
56	9	7	3	7	4	17	35	1	1	14	2
57	5	5	2	9	2	9	36	0	0	28	4
58	4	1	4	2	1	19	26	3	0	38	2
59	17	17	3	2	5	4	31	4	1	16	0
60	6	4	1	15	1	6	36	1	0	26	4
61	3	16	1	12	2	11	30	3	0	20	2
62	9	11	3	6	1	15	33	3	0	16	3
63	4	5	1	9	4	12	31	4	2	26	2
64	14	5	1	7	4	12	29	2	1	24	1
65	11	9	4	9	3	6	32	8	3	11	4
66	9	3	3	6	5	14	34	3	2	20	1
67	6	8	3	12	5	12	22	2	0	23	7
68	3	7	2	16	2	12	25	0	3	24	6
69	3	6	3	6	3	13	29	7	1	24	5
70	12	8	4	15	3	5	31	2	0	17	3
71	3	4	1	17	0	13	30	0	0	26	6
72	9	6	1	19	2	9	22	3	0	24	5
73	7	9	1	47	2	1	7	1	0	21	4
74	8	6	2	12	3	10	33	1	0	22	3
76	11	4	1	11	2	11	29	2	0	26	3
77	2	10	0	14	0	11	27	3	0	27	6
78	6	10	2	14	2	4	24	2	0	30	6
79	7	7	3	13	3	11	23	3	1	24	5
80	5	16	1	29	3	0	11	3	0	23	9

M107 (MW14-GC-107)

Sa	Qz	Mi	Oq	Ag	OT	PF	BF	Ml	TB	OB	Nl
8	27	14	2	2	9	5	12	11	0	16	2
9	21	12	2	5	8	3	14	12	0	22	1
10	23	7	2	7	10	3	16	10	0	19	3
11	21	8	5	2	7	5	18	9	0	22	3
12	18	17	2	2	5	1	20	20	1	14	0
13	31	12	2	4	9	4	18	6	0	13	1
14	28	12	6	4	9	2	12	8	0	19	0
15	7	3	6	4	8	6	19	11	0	23	13
16	29	7	4	7	8	6	12	14	0	13	0
17	27	10	1	7	9	5	12	10	2	15	2
18	28	19	2	3	11	1	11	9	0	14	2
19	26	17	2	2	5	3	12	16	1	14	2
20	24	14	5	5	12	3	9	12	2	13	1
21	22	13	2	2	10	1	9	9	1	24	7
22	25	14	5	4	8	3	10	16	2	12	1
23	21	17	4	2	9	1	12	15	0	17	2
24	20	15	5	1	6	3	15	13	1	20	1
25	23	8	5	1	11	7	15	6	0	21	3
26	21	14	3	2	3	6	15	16	1	17	2
27	26	6	3	2	10	2	14	16	0	19	2
28	28	14	3	1	11	4	13	6	0	19	1
29	27	16	0	3	4	5	9	13	0	22	1
30	24	9	4	2	5	8	13	18	0	16	1
31	26	14	5	1	4	4	12	19	0	15	0

Annex D: Principle Component Analysis – Loadings

M107 (MW-GC-107)

Sample	PC1	PC2	PC3	PC4
8	-0.056	0.119	0.116	-0.157
9	0.063	0.047	0.005	-0.038
10	0.191	0.180	-0.208	-0.049
11	0.275	-0.021	0.168	-0.002
12	-0.213	-0.374	0.030	0.165
13	0.016	0.316	-0.022	-0.136
14	0.044	0.214	0.044	0.171
15	0.652	-0.285	-0.087	0.164
16	0.114	0.071	-0.367	-0.244
17	-0.074	0.147	-0.469	-0.113
18	-0.235	0.284	0.121	0.143
19	-0.277	-0.164	-0.017	-0.061
20	-0.142	0.060	-0.371	0.305
21	-0.114	0.137	0.108	0.304

22	-0.196	-0.126	-0.330	0.184
23	-0.129	-0.052	0.195	0.244
24	-0.049	-0.224	0.175	0.215
25	0.292	0.172	0.227	0.020
26	-0.076	-0.344	-0.001	-0.166
27	0.115	-0.001	0.026	0.017
28	0.014	0.284	0.305	0.037
29	-0.209	0.059	0.159	-0.545
30	0.097	-0.234	0.002	-0.318
31	-0.103	-0.268	0.191	-0.141

M106 (MW-GC-106)

Sample	PC1	PC2	PC3	PC4
52	0.027	0.093	-0.139	-0.045
53	-0.194	-0.074	0.194	0.244
54	0.133	0.022	-0.220	0.016
56	0.190	-0.106	0.346	0.011
57	0.067	0.197	0.235	0.096
58	0.307	0.273	-0.347	-0.202
59	0.114	-0.522	-0.019	0.219
60	-0.033	0.161	0.067	0.053
61	-0.028	0.000	-0.113	0.394
62	0.145	-0.094	0.052	0.352
63	0.118	0.018	-0.147	-0.203
64	0.134	-0.092	0.089	-0.202
65	0.068	-0.416	0.001	-0.050
66	0.225	-0.102	0.096	-0.296
67	-0.002	-0.007	-0.009	-0.088
68	-0.025	0.172	0.354	-0.159
69	0.169	-0.036	-0.327	-0.083
70	-0.069	-0.170	0.186	0.040
71	-0.028	0.429	0.250	0.157
72	-0.108	0.049	-0.049	-0.115
73	-0.586	0.031	0.056	-0.327
74	0.032	0.035	0.159	0.030
76	0.051	0.069	0.014	-0.085
77	-0.061	0.276	-0.287	0.385
78	-0.131	0.008	-0.152	0.069
79	0.007	-0.037	-0.020	-0.196
80	-0.522	-0.175	-0.271	-0.016
78	-0.131	0.008	-0.152	0.069
79	0.007	-0.037	-0.020	-0.196
80	-0.522	-0.175	-0.271	-0.016

POP2 (POPEI2-1-CGP)

Sample	PC1	PC2	PC3	PC4
50	0.148	-0.181	-0.123	-0.172
51	0.201	0.067	0.027	-0.143
52	0.085	-0.001	-0.279	0.176
53	0.261	0.194	-0.151	-0.260
54	0.048	-0.119	-0.132	0.173
55	0.083	-0.268	-0.220	-0.075
56	0.171	0.033	-0.147	0.077
57	0.153	0.053	0.138	-0.050
58	0.223	0.011	-0.112	0.080
59	0.080	0.162	0.035	-0.148
60	0.309	0.473	0.030	0.170
61	-0.043	0.352	0.265	-0.037
62	0.186	-0.332	0.234	0.449
63	0.162	-0.356	0.082	-0.345
64	-0.225	0.070	0.128	0.226
65	0.160	0.029	0.131	0.291
66	-0.052	-0.049	0.002	0.121
68	-0.234	0.090	0.089	0.193
69	-0.210	-0.030	0.533	-0.046
70	-0.332	0.079	-0.212	-0.003
71	-0.267	0.048	-0.270	0.175
72	0.053	-0.118	0.293	-0.085
73	-0.058	-0.312	0.083	-0.095
74	-0.027	0.126	0.067	-0.250
75	-0.257	0.103	-0.006	-0.327
76	-0.019	-0.081	-0.056	-0.092
77	-0.236	0.123	-0.087	-0.096
78	-0.059	0.028	-0.273	0.066
79	-0.307	-0.195	-0.071	0.027

Annex E: Microtexture Surface Occupation

All values are in %, except for angularity which is scaled from 0 (very round) – 5 (very angular) after Powers (1953). The microtextures were later scaled to 0 – 5 (see **Figure 17**).

Sample	Dissolution	FreshSurface	PercussionMark	AdheringParticle	Angularity
PostTsunami	50.68	37.600	0.000	10.680	4.000
PostTsunami	79.31	17.460	0.740	1.340	1.000
PostTsunami	12.13	71.090	9.480	7.850	4.000
PostTsunami	72.27	18.400	0.000	4.930	2.000
PostTsunami	67.73	21.170	3.860	4.940	3.000
PostTsunami	89.91	0.000	5.370	3.980	3.000
PostTsunami	47.88	44.730	5.490	1.960	2.000

PostTsunami	46.74	38.340	10.030	1.900	3.000
PostTsunami	21.79	47.550	20.110	7.010	3.000
PostTsunami	79.21	9.770	0.000	6.630	1.000
PostTsunami	75.69	0.000	7.470	15.850	2.000
PostTsunami	57.4	25.880	6.840	8.860	3.000
PostTsunami	88.82	6.030	0.000	9.980	3.000
PostTsunami	84.36	2.970	0.000	9.110	3.000
PostTsunami	29.93	46.130	18.620	5.110	3.000
PostTsunami	69.76	19.450	1.420	8.910	2.000
PostTsunami	87.79	7.880	0.000	3.100	2.000
PostTsunami	42.89	44.100	5.390	6.660	4.000
PostTsunami	56.22	19.030	16.560	5.670	2.000
PostTsunami	55.78	25.320	14.470	3.190	1.000
PostTsunami	21.02	60.180	12.040	6.080	3.000
PostTsunami	25.5	52.630	11.280	10.070	5.000
PostTsunami	84.8	8.470	0.000	5.970	3.000
PostTsunami	42.38	34.210	9.010	13.430	3.000
PostTsunami	30.53	49.870	14.100	4.980	1.000
PostTsunami	63.12	28.420	2.290	4.380	2.000
PostTsunami	75.74	15.130	4.600	4.040	2.000
PostTsunami	40.39	34.470	15.060	10.070	3.000
PostTsunami	78.53	16.520	0.000	3.100	3.000
PostTsunami	84.65	0.000	2.800	12.710	2.000
PostTsunami	100.71	0.000	0.000	3.620	4.000
PostTsunami	85.7	0.000	9.920	4.060	2.000
PostTsunami	61.94	33.100	0.000	4.230	2.000
PostTsunami	74.29	0.000	0.000	26.190	2.000
PreTsunami	91.94	2.520	0.000	4.310	1.000
PreTsunami	68.93	23.840	0.000	7.210	3.000
PreTsunami	88.85	0.000	3.720	6.230	2.000
PreTsunami	74.51	9.210	7.130	8.170	1.000
PreTsunami	65.36	28.790	0.000	5.340	4.000
PreTsunami	68.32	25.770	4.860	0.000	3.000
PreTsunami	65.84	16.040	0.000	17.160	2.000
PreTsunami	18.34	69.110	8.860	2.530	4.000
PreTsunami	78.46	8.010	11.090	1.210	1.000
PreTsunami	91.77	0.000	0.000	7.760	0.000
PreTsunami	38.75	45.430	9.990	5.660	2.000
PreTsunami	94.48	0.000	0.000	4.790	1.000
PreTsunami	65.88	23.970	5.840	3.030	3.000
PreTsunami	63.37	28.560	5.010	2.680	2.000
PreTsunami	40.04	49.920	10.550	0.000	3.000
PreTsunami	50.94	29.960	7.430	10.980	2.000
PreTsunami	85.24	0.000	7.380	7.230	1.000
PreTsunami	69.21	16.710	4.700	9.610	2.000
PreTsunami	54.03	14.050	19.650	11.530	2.000
PreTsunami	47.78	14.730	33.340	2.830	1.000
PreTsunami	88.47	0.000	0.000	10.660	2.000

PreTsunami	62.64	17.690	3.690	15.910	3.000
PreTsunami	52.07	36.990	5.350	4.640	3.000
PreTsunami	50.39	30.870	10.080	7.160	3.000
PreTsunami	58.94	0.000	38.740	0.000	1.000
PreTsunami	60.61	12.560	19.040	7.620	2.000
PreTsunami	52.37	22.630	17.060	7.040	2.000
PreTsunami	74.91	0.000	16.990	8.390	2.000
Tsunami	55.45	28.810	10.710	3.050	4.000
Tsunami	25.4	62.140	4.990	6.630	3.000
Tsunami	59.11	29.660	5.280	6.700	3.000
Tsunami	42.28	46.180	9.320	2.250	4.000
Tsunami	87.59	3.250	0.000	9.090	2.000
Tsunami	36.43	40.760	9.910	1.770	2.000
Tsunami	71.87	15.240	5.600	7.550	2.000
Tsunami	63.52	20.280	0.000	15.660	4.000
Tsunami	29.29	50.470	18.550	0.000	3.000
Tsunami	116.53	16.230	20.350	2.790	2.000
Tsunami	50.34	29.880	6.640	12.700	2.000
Tsunami	53.92	16.000	3.960	25.630	0.000
Tsunami	39.55	46.750	10.260	2.290	2.000
Tsunami	81.19	3.110	6.310	9.830	3.000
Tsunami	60.66	23.970	8.900	3.390	2.000
Tsunami	17.42	68.230	6.320	6.920	5.000
Tsunami	61.21	27.840	6.980	4.240	3.000
Tsunami	81.96	5.600	3.910	7.730	3.000
Tsunami	64.91	14.820	12.130	6.610	1.000
Tsunami	9.85	55.500	32.650	0.000	3.000
Tsunami	41.73	29.560	10.200	17.950	2.000
Tsunami	49.34	36.350	9.790	4.210	2.000
Tsunami	84.36	0.000	2.090	13.490	1.000
Tsunami	15.41	70.520	5.340	8.390	4.000
Tsunami	81.75	2.100	4.900	11.170	1.000
Tsunami	36.06	43.120	12.150	9.400	3.000
Tsunami	44.18	29.280	14.720	11.280	2.000
Tsunami	45.91	40.760	7.670	4.310	1.000

Annex F: R-Script for Microtextural Analysis

The R-script below was created and used for the microtextural analysis. There are comments added explaining some commands and to draw attention to code that must be adjusted. Also, images names must have a clear pattern and polygons files, covering the approximate surface area of microtextures must be created before the analysis with this R-script.

In the present study the free software ‘mirone’ (Luis, 2007) (http://w3.ualg.pt/~jluis/mirone/main.html) was used to draw polygons on the image and save them as dat-files. When using another approach, it is important to note, that the polygon files with x and y coordinates need to have same coordinates in the first and the last row. Also intersecting polygons should be avoided.

References:

J. F. Luis. Mirone: A multi-purpose tool for exploring grid data. Computers & Geosciences, 33, 31-41, 2007.

Script:

```
##################################### Microtexture Analysis ##################################

setwd("C:/SEM_Analysis") # change to the path to your images
rm(list=ls()) # cleans the global environment

### Before starting make sure you have a copy of all images in a different directory. Also
### make sure that the images have similar patterns in their name, otherwise it will not work
### with this script.

##################################### Code Name Generation ###################################

filelist <- list.files(path="./",pattern="01\\(") # Choose pattern of your image names e.g. "grain*"

# generates random numbers from 0 to number of images you have
randomnumbers <- sample(0:length(filelist), length(filelist), replace = F)

# Generates the decoding list
x<- paste("image",randomnumbers,".jpg", sep="") # change to your file-format
decoding_list<- data.frame(col1=filelist, col2=x)
write.csv2(decoding_list, file ="decoding_list.csv", append = FALSE, quote = FALSE, sep="\t")

# renames the images with the code names
for(i in 1:length(filelist)){file.rename(filelist[i], paste0("image", randomnumbers[i], ".jpg"))}

################################### Calculate Surface Area ###################################

### Generated polygon files need to have a specific name according to their microtexture.
### Polygon-files (x,y) need to have same starting coordinates and end coordinates and
### saved as dat-file (or change in the script).
### Here, it is "grain001_pollyD.dat" for a dissolution polygon of "image001.jpg".
### (F = Freshsurfaces, P = Percussion Marks, A = Adhering Particles, 100 = outline of grain).
### There can be as many polygons for one microtexture as needed. If more than one, extend
### the file name to "grain001_polyD2.dat" etc.

 # install.packages("geometry") # if not installed you need to execute the command
library(geometry)
# Number of the grain-image and file name:
g_nbr<- 993
# Roundness classification:
R<- 2
# Setting variables
file<- paste("grain",g_nbr,"_poly100.dat", sep="")
file_D<- paste("grain",g_nbr,"_polyD", sep="")
file_F<- paste("grain",g_nbr,"_polyF", sep="")
file_P<- paste("grain",g_nbr,"_polyP", sep="")
file_A<- paste("grain",g_nbr,"_polyA", sep="")
filelist_D <- list.files(path="./",pattern=file_D)
filelist_F <- list.files(path="./",pattern=file_F)
filelist_P <- list.files(path="./",pattern=file_P)
filelist_A <- list.files(path="./",pattern=file_A)
D<- 0; F<- 0; P<- 0; A<- 0
# full grain surface:
poly100<- read.table(file, header = FALSE, sep = "", dec = ".")
x_full<- poly100[,1]
y_full<- poly100[,2]
full<- round((polyarea(x_full,y_full,d=1)), digits=2)
# Dissolution area of grain:
if (identical(filelist_D, character(0))){
```

```
  D_total<- 0
} else {
  for(i in 1:length(filelist_D)){
    polyD<- read.table(filelist_D[i] ,header = FALSE, sep = "", dec = ".")
    xD<- polyD[,1]
    yD<- polyD[,2]
    D[i]<- polyarea(xD,yD, d=1)}
  D_total<- sum(D)
}
# Fresh surfaces area of grain:
if (identical(filelist_F, character(0))){
  F_total<- 0
} else {
  for(i in 1:length(filelist_F)){
    polyF<- read.table(filelist_F[i] ,header = FALSE, sep = "", dec = ".")
    xF<- polyF[,1]
    yF<- polyF[,2]
    F[i]<- polyarea(xF,yF, d=1)}
  F_total<- sum(F)
}
# Percussion marks area of grain:
if (identical(filelist_P, character(0))){
  P_total<- 0
} else {
  for(i in 1:length(filelist_P)){
    polyP<- read.table(filelist_P[i] ,header = FALSE, sep = "", dec = ".")
    xP<- polyP[,1]
    yP<- polyP[,2]
    P[i]<- polyarea(xP,yP, d=1)}
  P_total<- sum(P)
}
# Adhering particles area of grain:
if (identical(filelist_A, character(0))){
  A_total<- 0
} else {
  for(i in 1:length(filelist_A)){
    polyA<- read.table(filelist_A[i] ,header = FALSE, sep = "", dec = ".")
    xA<- polyA[,1]
    yA<- polyA[,2]
    A[i]<- polyarea(xA,yA, d=1)}
  A_total<- sum(A)
}
# Percentages of grain surface features and export as csv-file
pD<- round(((D_total*100)/full), digits=2)
pF<- round(((F_total*100)/full), digits=2)
pP<- round(((P_total*100)/full), digits=2)
pA<- round(((A_total*100)/full), digits=2)
# Creation of text-file with percentages and roundness
surface_occ<- data.frame(col1=pD, col2=pF, col3=pP, col4=pA, col5=R)
names(surface_occ)<- c("Dissolution_Area[%]", "FreshSurface_Area[%]",
                       "PercussionMarks_Area[%]", "AdheringParticle_Area[%]", "Angularity")

final_file_name<- paste("image_",g_nbr,"_surface_occupation.txt", sep="")
write.table(surface_occ, file=final_file_name, append = FALSE, sep = "\t", dec = ".",
            row.names = FALSE, col.names = TRUE)
# Show quick result for checking errors
sum(pD,pF,pP,pA)
# Show angularity that was given
R
# Show image nr.
g_nbr

################################### Decoding and Generation of Data Table ######################

### the txt-files with the calculated percentages ("image_001_surface_occupation.txt") and the
### decodinglist-file needs to be in the same folder as the working directory.

# install.packages("readxl")
library(readxl)
# Generate file list of all txt-files with the calculated percentages
file.list<- list.files(path = "./", pattern = "surface_occupation", full.names = TRUE)
datalist<- lapply(file.list, FUN=read.table, header=TRUE)
# Read decoding list
decoding_list<- read.csv2("decoding_list.csv")
code_name_list<- as.character(decoding_list$col2)
real_name_list<- as.character(decoding_list$col1)
# Setting varibales
image_nr<-0
real_names<-0
# Decoding
for(i in 1:length(file.list)){
  image_nr[i]<- if (nchar(file.list[i])==34){
    substr(file.list[i], 9, 11)
  } else if (nchar(file.list[i])==33){
    substr(file.list[i], 9, 10)
  } else {
    substr(file.list[i], 9, 9)
  }
```

```
}

for(i in 1:length(image_nr)){
  real_names[i]<- substr(real_name_list[grep(image_nr[i], code_name_list)],1,2)}
# change the names and numbers according to your case. Here are only 3 samples but more can be
# added.
real_names<- factor(real_names)
levels(real_names) <- list("PostTsunami"=14, "Tsunami"=18, "PreTsunami"=25)
# Generation of data frame
datafr<- do.call("rbind", datalist)
datafr$sample<- real_names
colnames(datafr)<- c("Dissolution", "FreshSurface", "PercussionMark", "AdheringParticle",
                     "Angularity", "sample")
# recaclculate percentages into a new scale from 0 - 5
for(i in 1:4){
  datafr[,i]<- replace(datafr[,i], datafr[,i] < 0.1, 0)
  datafr[,i]<- replace(datafr[,i], datafr[,i] > 0.1 & datafr[,i] < 10, 1)
  datafr[,i]<- replace(datafr[,i], datafr[,i] > 10 & datafr[,i] < 25, 2)
  datafr[,i]<- replace(datafr[,i], datafr[,i] > 25 & datafr[,i] < 50, 3)
  datafr[,i]<- replace(datafr[,i], datafr[,i] > 50 & datafr[,i] < 75, 4)
  datafr[,i]<- replace(datafr[,i], datafr[,i] > 75, 5)
}

################################## Statistical Analysis ########################################

# install.packages("tidyr")
library(tidyr)
# install.packages("ggplot2")
library(ggplot2)
# install.packages("ggpubr")
library(ggpubr)

# Kruskal Wallis tests:
datafr$sample<- ordered(datafr$sample, levels= c("PreTsunami", "Tsunami", "PostTsunami") )
kt_AdheringParticle<- kruskal.test(AdheringParticle ~ sample, data = datafr)
kt_Dissolution<- kruskal.test(Dissolution ~ sample, data = datafr)
kt_FreshSurface<- kruskal.test(FreshSurface ~ sample, data = datafr)
kt_PercussionMark<- kruskal.test(PercussionMark ~ sample, data = datafr)
kt_Angularity<- kruskal.test(Angularity ~ sample, data = datafr)

# Generation of plots:
p1 <- ggplot(datafr, aes(x=sample, y=AdheringParticle)) +
  coord_cartesian(ylim=c(0,5))+
  geom_boxplot(fill='#A4A4A4', color="black")+
  theme_classic() +
  theme(axis.title.x=element_blank())+
  annotate("text", x = 2, y= 4,
           label = paste("KW: p-value =",round(kt_AdheringParticle$p.value, digits = 4)," "),
           color ="black", cex=2.5)+
  ylab("Adhering particles")+
  stat_summary(fun.y=mean, geom="point", shape=17, size=3, color="red")

p2 <- ggplot(datafr, aes(x=sample, y=Dissolution)) +
  coord_cartesian(ylim=c(0,5))+
  geom_boxplot(fill='#A4A4A4', color="black")+
  theme_classic() +
  theme(axis.title.x=element_blank())+
  annotate("text", x = 2, y= 0.5,
           label = paste("KW: p-value =",round(kt_Dissolution$p.value, digits =4)," "),
           color ="black",cex=2.5)+
  stat_summary(fun.y=mean, geom="point", shape=17, size=3, color="red")

p3 <- ggplot(datafr, aes(x=sample, y=PercussionMark)) +
  coord_cartesian(ylim=c(0,5))+
  geom_boxplot(fill='#A4A4A4', color="black")+
  theme_classic() +
  theme(axis.title.x=element_blank())+
  coord_cartesian(ylim=c(0,5))+
  annotate("text", x = 2, y= 4,
           label = paste("KW: p-value =",round(kt_PercussionMark$p.value, digits = 4)," "),
           color ="black",cex=2.5)+
  ylab("Percussion marks")+
  stat_summary(fun.y=mean, geom="point", shape=17, size=3, color="red")

p4 <- ggplot(datafr, aes(x=sample, y=FreshSurface)) +
  coord_cartesian(ylim=c(0,5))+
  geom_boxplot(fill='#A4A4A4', color="black")+
  theme_classic() +
  theme(axis.title.x=element_blank())+
  annotate("text", x = 2, y= 4.5,
           label = paste("KW: p-value =",round(kt_FreshSurface$p.value, digits = 4)," "),
           color ="black",cex=2.5)+
  ylab("Fresh surfaces")+
  stat_summary(fun.y=mean, geom="point", shape=17, size=3, color="red")

p5 <- ggplot(datafr, aes(x=sample, y=Angularity)) +
  coord_cartesian(ylim=c(0,5))+
  geom_boxplot(fill='#A4A4A4', color="black")+
```

```
  theme_classic() +
  theme(axis.title.x=element_blank())+
  annotate("text", x = 2, y= 4.7,
           label = paste("KW: p-value =",round(kt_Angularity$p.value, digits = 4)," "),
           color ="black",cex=2.5)+
  stat_summary(fun.y=mean, geom="point", shape=17, size=3, color="red")
# Plot
ggarrange(p1,p2,p3,p4,p5, ncol = 3, nrow = 2)
```